UNIVERSITÀ DEGLI STUDI DI MILANO

Scuola di Dottorato in Fisica, Astrofisica e Fisica Applicata

Dipartimento di Fisica

Corso di Dottorato in Fisica, Astrofisica e Fisica Applicata

Ciclo XXV

The warm nuclear rotation in ^{174}W: conservation of the K quantum number in the order to chaos region

Settore Scientifico Disciplinare FIS/04

Tutor: Prof.ssa Silvia LEONI

Cotutor: Prof.ssa Angela BRACCO

Coordinatore: Prof. Marco BERSANELLI

Tesi di Dottorato di:

Valeria VANDONE

Anno Accademico 2011-2012

Commission of the final examination:

External Referee:
Prof. Giovanni LA RANA

External Member:
Prof. Mauro BRUNO

Internal Member:
Prof.ssa Angela BRACCO

Final examination:

Date 06/02/2013
Università degli Studi di Milano, Dipartimento di Fisica, Milano, Italy

MIUR subjects:

FIS/04 - FISICA NUCLEARE E SUBNUCLEARE

PACS:

27.70.+q - Mass region $150 \leq A \leq 189$
23.20.Lv - γ-transitions and level energies
25.70.Gh - Compound nucleus
21.10.Re - Collective levels

Contents

Introduction

Warm rotating nuclei produced at high spin by heavy-ion fusion-evaporation reactions give the possibility to investigate the transition between order and chaos in a many body quantum system. This is a fascinating subject which is currently investigated in different research fields from solid state to nuclear physics.
In nuclear physics, it is found that the nucleus behaves as an ordered system with well-defined quantum numbers and associated selection rules at temperature[1] $T \sim 0$, namely at very low excitation energy. As the internal energy increases, energy levels start to interact giving rise to a gradual loss of selection rules. As a consequence, quantum numbers lose their meaning with temperature. The extreme regime is the chaotic region of the compound nucleus, where only energy, spin and parity are well defined for each energy level [1, 2].
The weakening of the selection rules with temperature can be studied focusing on the K-quantum number (i.e. the projection of the total angular momentum on the symmetry axis). Close to the yrast line K is a well-defined quantum number, and the γ-decay flows built on low-K and high-K configurations are well-distinguished. As the internal energy increases, a statistical K-mixing process takes place, due to the high density of states. Therefore, by studying the γ-decay flow in coincidence with low-K and high-K states in the region between the cold regime close to the yrast line[2] and the chaotic compound nucleus region, information on the order-to-chaos transition can be obtained [3].
In this respect, the nucleus ^{163}Er is the only investigated case [4], giving indication

[1] The nuclear temperature is defined as $T = (d(\ln \rho(U))/dU)^{-1}$, being ρ the density of states and U the internal energy of the nucleus. It can be approximated by the expression $T \approx \sqrt{U/a}$, where $a = A/8$ is the level density parameter (A is the mass of the nucleus).

[2] Yrast line: sequence of nuclear states with the minimum energy at a given spin.

of a gradual transition between order and chaos at around 2.5 MeV of excitation energy, as a consequence of a progressive K-mixing process. Therefore, additional experimental investigations are needed and an interesting case is represented by the ^{174}W nucleus [5, 6], studied in this thesis. In particular, ^{174}W is characterized by the existence of low-K ($\sim 3-4$) and high-K ($\sim 8-12$) rotational bands extending up to spin $39\hbar$, with two high-K bands ($K = 8$ and $K = 12$) built on isomeric states, with lifetimes longer than 120 ns. This feature has been the key-point of the present experimental data analysis.

The ^{174}W nucleus has been populated by the fusion-evaporation reaction of ^{50}Ti (at 217 MeV) on a ^{128}Te target (1 mg/cm^2 thick, backed by 50 mg/cm^2 of ^{nat}Pb). The experiment was performed in July 2010 at Legnaro National Laboratories of INFN, using the first phase of the Advanced GAmma Tracking Array (AGATA) [7], coupled to a multiplicity filter of 27 BaF_2 scintillators (the HELENA array).

To probe the gradual weakening of the selection rules on the K-quantum number with temperature, γ-γ matrices selecting low-K and high-K structures have been constructed and analysed by statistical fluctuation techniques [8]. This allows to estimate the number of low-K and high-K bands and their correlations, as a function of excitation energy. In particular, the selection of low-K and high-K transitions has required the use of both prompt and delayed γ coincidences with respect to a time reference given by the HELENA array.

The interpretation of the data has been based on a Monte Carlo simulation code, using as input microscopic Cranked Shell Model calculations at finite temperature [9]. The simulation reproduces the γ decay flux of ^{174}W and creates γ coincidence spectra which can be analysed by the same analysis techniques applied to the data.

The study of the warm rotation in ^{174}W along discrete rotational bands has evidenced the importance of introducing a quenching factor in the E1 decay between low-K and high-K bands. This problem has been discussed in a more general context, in order to relate our results to the reduced hindrance values f_ν, extracted from standard discrete spectroscopy studies of high-K isomers [10].

For the first time it is demonstrated that K-mixing is a general mechanism which well explains the hindrance to the γ-decay between low- and high-K states for both regular excited bands and isomeric states, as a function of temperature. This is a step forward in understanding the basic rules governing the decay properties of isomeric systems.

In summary, in Chapter 1 the nuclear rotational motion will be described in connection with K isomerism, while in Chapter 2 Cranked Shell Model calculations at finite temperature for the specific ^{174}W nucleus will be presented. The experimental set-up and the preliminary part of the data analysis will be reported in Chapter 3 and 4, respectively. Finally, results of the experimental data analysis will be shown in Chapter 5 and their comparison with simulated ones will be presented in Chapter 6. The last chapter, Chapter 7, will be devoted to the study of the role played by the K-mixing process in the K hindrance to the γ the decay.

Chapter 1

Nuclear rotational motion

In this Chapter we briefly discuss the main aspects which are relevant for the study of the nuclear rotational motion, at finite temperature. In particular, we describe the most important aspects of the fusion reaction mechanism, used to populate the excited rotational nuclei under investigation, and the the properties of their γ decay. We then introduce the topic of the transition between order and chaos, which is the subject of this thesis, in connection with the conservation of selection rules on the K quantum number and K-isomers decay. Finally, we discuss the analysis techniques applied to the experimental data presented in this thesis work.

1.1 Heavy ion fusion reactions

Complete nuclear fusion induced by heavy ions accelerated at energies around the Coulomb barrier, $\sim 5\ MeV/nucleon$, is the most efficient way to produce nuclei at high excitation energy and high angular momentum.
In complete fusion processes the accelerated particle is captured by the target nucleus and a compound nucleus is created. In the centre of mass frame, the kinetic energy of the projectile is converted in excitation energy of the compound nucleus and quickly distributed among all nucleons. In general one speaks about compound nucleus only if the half life of the nuclear system (projectile and target) is greater than $10^{-22}\ s$ [11]. In this case, in fact, the nucleons have time enough to redistribute the energy, and the nucleus reaches a stage of thermodynamical

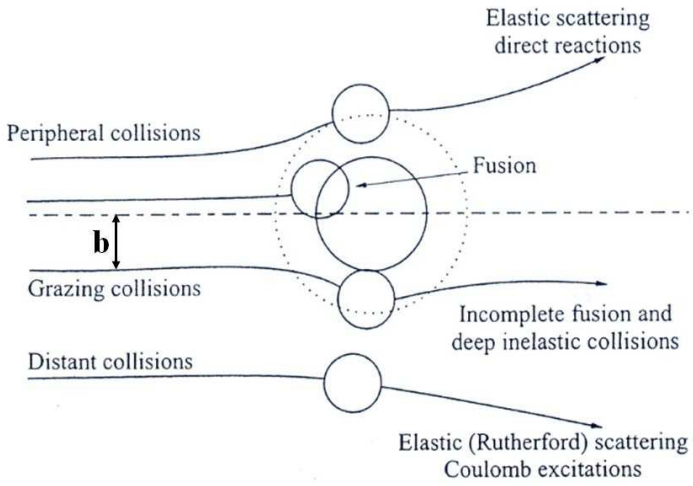

Figure 1.1: Picture of heavy-ion interactions showing the trajectories corresponding to close, grazing, peripheral and distant collisions [11].

equilibrium before decaying [12].

Many reaction mechanisms are in strong competition with the complete fusion process, one of which is, for example, fast fission. The bombarding energy of the projectiles needs to be accurately chosen in order to be high enough to penetrate the Coulomb barrier but lower than the values that would lead to fission. As shown in Fig. 1.1, a limited range of impact parameters b leads to fusion. In general, it is assumed that the distance between the projectile and the target is smaller than the radius of the Coulomb barrier, R_{Coul}, given experimentally by [13]:

$$R_{Coul} = 1.36 \cdot (A_p^{1/3} + A_t^{1/3}) + 0.5 \ fm \tag{1.1}$$

while the height of the Coulomb barrier is

$$E_{Coul}[MeV] = \frac{Z_p Z_t e^2}{R_{Coul}} = 1.44 \ \frac{Z_p Z_t}{R_{Coul}[fm]} \tag{1.2}$$

In the previous expressions A_p,Z_p and A_t,Z_t are the mass and atomic numbers of the projectile and the target, respectively.

The impact parameter b is related to the angular momentum l, transferred during the reaction process, according to the relation:

$$l\hbar = M_p v_p b \tag{1.3}$$

being M_p and v_p the mass and velocity of the projectile.
The sum of the potential energy and of the rotational energy of the system at the distance of R_{Coul} is given by

$$E_{Coul} + \frac{\hbar^2 l(l+1)}{2\mu R_{Coul}} \tag{1.4}$$

Then the distance R_{Coul} can be reached if and only if:

$$E_{cm} \geq E_{Coul} + \frac{\hbar^2 l(l+1)}{2\mu R_{Coul}} \tag{1.5}$$

where E_{cm} is the energy of the system in the center of mass, given by $E_{cm} = \left(\frac{M_p}{M_p + M_t}\right) E_{lab}$; here M_p and M_t are the mass of the projectile and target, and μ is the reduced mass of the system, defined as $\mu = \frac{M_p \cdot M_t}{M_p + M_t}$.
The maximum angular momentum l_{max} corresponding to fusion is then given by the relation:

$$E_{cm} = E_{Coul} + \frac{\hbar^2 l_{max}(l_{max}+1)}{2\mu R_{Coul}} \tag{1.6}$$

This allows to calculate the maximum angular momentum transferred from the reaction

$$l_{max} = R_{Coul}\sqrt{2\mu(E_{cm} - E_{Coul})} \tag{1.7}$$

that is related to the fission process. If the compound nucleus is too hot or has too high angular momentum the particle and γ emission before thermalisation become important (pre-equilibrium). The fission probability increases with the angular momentum and excitation energy [14].
The excitation energy given to the system by the heavy-ion reactions is given in the centre of mass frame by

$$E_{ex} = E_{cm} + Q_{fus} \tag{1.8}$$

where Q_{fus} is the Q-value for the complete fusion reaction, corresponding to the difference between the energy before and after the formation of the composite nucleus, and is given by the difference between the final and initial rest masses.

The compound nucleus is formed with a given excitation energy E_{ex}, while the transferred momentum, that depends on the impact parameter b, can vary from 0 to l_{max}, within a distribution shown in the centre of Fig. 1.2. The decay of the

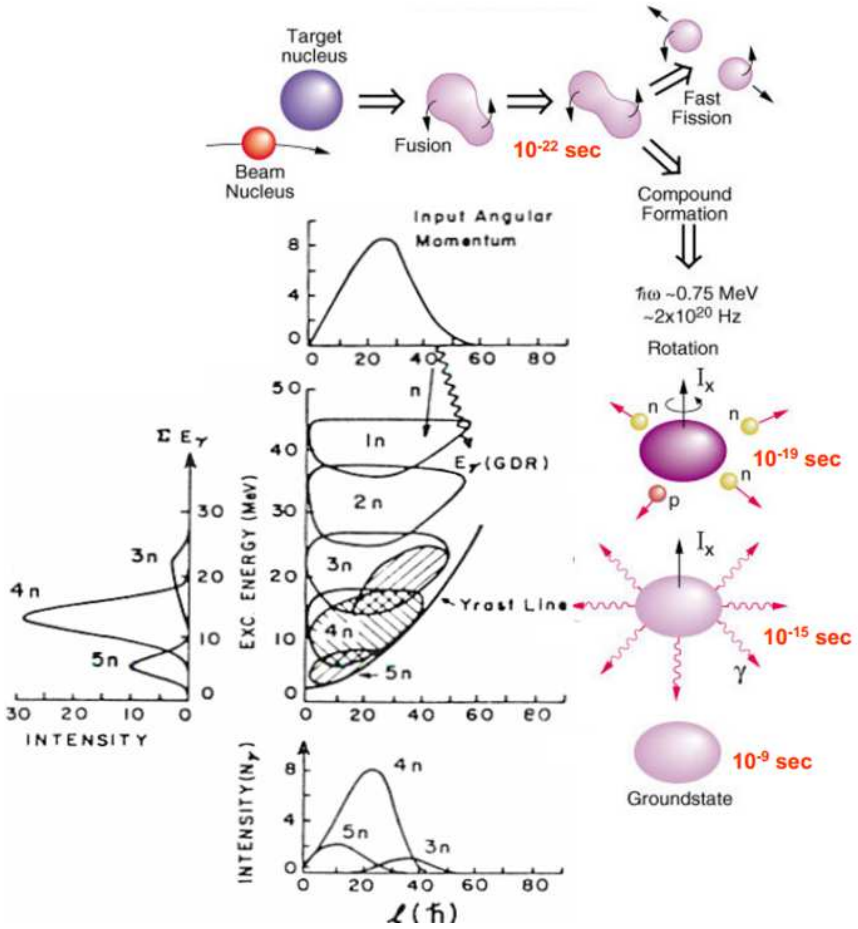

Figure 1.2: Schematic representation of the formation and decay of a compound nucleus produced in a fusion-evaporation reaction (upper and right part of the picture). Typical time ranges are also indicated. Results from the statistical model are reported in the central part of the picture, showing the input angular momentum and the population of single decay channels, both as a function of the angular momentum and of the excitation energy [11, 15].

composite nucleus can be divided into two steps. At the beginning, for excitation energies greater then the binding energy of a nucleon ($\sim 8\ MeV$), the nucleus looses energy evaporating particles, typically neutrons but also protons and α particles. The emission of neutron is generally favoured since they do not need to overcome the Coulomb barrier.

The number of emitted neutrons depends on the excitation energy and on the spin of the nucleus. Since the evaporation of one neutron reduces on average the energy of about 10 MeV (8 MeV is the average binding energy of the neutrons and 2 MeV the mean kinetic energy of an evaporated neutron) but diminishes the spin of the nucleus by $\sim 1\hbar$ only, the number of emitted neutrons is roughly equal to $\Delta E[MeV]/10$, where ΔE is the difference between the excitation energy and the rotational energy. Being the dependence of the rotational energy with the spin quadratic ($E_{rot} = \frac{\hbar^2}{2\Im} I(I+1)$), at the same excitation energy, nuclei with a higher angular momentum will emit less neutrons and produce residual nuclei with higher excitation energy. In this first step of the decay the evaporation of light particles is in competition with the emission of γ-rays of dipolar nature (E1) due to the de-excitation of the Giant Dipole Resonance (GDR) built on the nucleus.

For excitation energies lower than the binding energy of the nucleon, the nucleus cannot emit any other light particle and the excitation energy is dissipated trough γ rays emission. These regions are shaded in Fig. 1.2: these are the "entry region" for each reaction channel. The wide distributions, obtained as a projection on the energy axis for each reaction channel, reflect the statistical nature of the particle evaporation process. In fact, even if the initial excitation energy has a precise value E_{ex}, the dissipated energy by each particle is a distribution 2 MeV wide. Fig. 1.2 shows entry spin distributions of each reaction channel, too. In this case the width of the distribution corresponds to the one of initial transferred angular momentum. At this point, the nucleus approaches the ground state by emitting γ-rays that for energies around 2 MeV above the yrast line [1] are mainly of E1 nature, that cool the nucleus without changing the angular momentum much. Below 2 MeV the preferred mechanism is the E2 decay that takes away 2 units of angular momentum at each step.

[1] The yrast line is defined as the sequence of nuclear states with the minimum energy at a given spin.

1.2 The γ decay

Through γ spectroscopy, it is possible to study nuclear states populated during the de-excitation of residues nuclei in the (I, E_{ex}) phase space. As it will be explained in Chap. 2, at high excitation energies above the yrast line, the level density rapidly increases and that the nucleus can choose between many different de-excitation paths. In this region the number of emitted γ rays is so high that no one can gain sufficient intensity to be observed as a discrete transition in the energy spectrum. Estimations of nuclear level density indicate that there is no significant superposition of levels within their width, that is of the order of $10^{-3} - 10^{-1}\ eV$. The region characterised by this phenomenon is called "quasi-continuum": γ rays emitted at these excitation energies are not resolvable and constitute an energy spectrum composed by:

1. *Statistical E1 transitions*, mainly regulated by level density, that remove excitation energy from the nucleus but only little angular momentum (red bump in Fig. 1.3);

2. *Collective unresolved E2 transitions*, responsible of angular momentum removal, that form the continuum distribution shaded in Fig. 1.3;

While collective transitions populate a small energy region ($E_\gamma \leq 2\ MeV$) of the γ energy spectrum, statistical ones extend in an interval of several MeV, so that the quasi-continuum spectrum can be approximated as a statistical exponential distribution, over which a quadrupolar continuum distribution is located.
At the end of the de-excitation cascade, the nucleus reaches a low excitation energy region, characterised by low level density; here the rotational motion goes through discrete rotational bands. In this case, the transitions are mainly of E2 nature, with $E_\gamma \leq 1\ MeV$, and lay over the E2 quasi-continuum distribution, as shown in Fig. 1.3 in the case of the γ spectrum of ^{163}Er.
E1 and E2 decay modes compete along the entire γ cascade, as will be decribed in Sec. 6.2, from the entry distribution down to the yrast line.

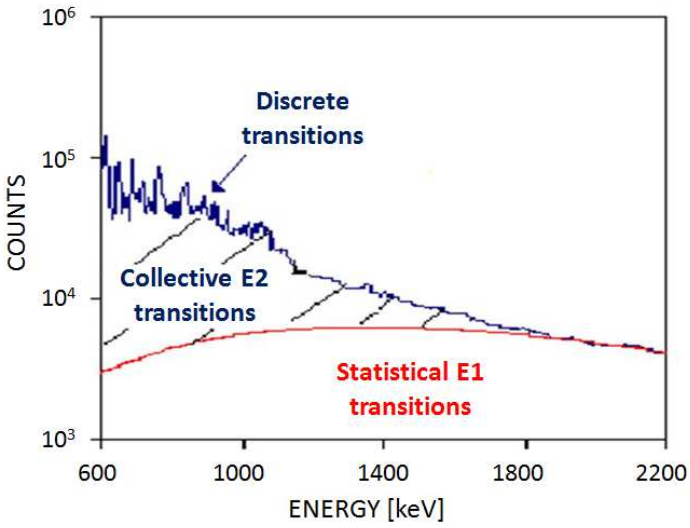

Figure 1.3: Energy spectrum produced by the decay of the ^{163}Er nucleus, produced in the heavy ion fusion reaction [16].

1.3 The rotational motion

In the case of nuclear rotation, two different kinds of spinning, both generating very high angular momenta, can be identified: a) collective rotation, typical of well deformed nuclei and b) non collective rotation, typical of spherical and little deformed nuclei (near the major closed shells). Since a quantum mechanical object cannot have collective rotation about a symmetry axis, collective rotation implies that the nucleus is deformed. Describing the nucleus as a drop of incompressible liquid, the shape of the nuclear surface in three dimensions can be expressed in terms of spherical harmonics $Y_{lm}(\theta, \phi)$ [17]

$$r(\theta, \phi) = r_0(1 + \sum_{lm} a_{lm} Y_{lm}(\theta, \phi)) \tag{1.9}$$

where r_0 is the radius at the spherical equilibrium, with the requirement of volume conservation.

In the case of quadropolar deformation (l=2) the expansion coefficient a_{2m} (being $m = 0, \pm 1, \pm 2$) can be reduced to two shape parameters β and γ, since $a_{21} = a_{2-1} = 0$ and $a_{22} = a_{2-2}$ are required by reflection symmetry of the deformation.

These parameters are defined as:

$$a_{20} = \beta \cos\gamma \qquad a_{22} = \frac{1}{\sqrt{2}}\beta \sin\gamma \tag{1.10}$$

While β (often denoted as β_2) represents the magnitude of the nuclear deformation (elongation or flattening), the parameter γ corresponds to the degree of non-axiality.

In a collective rotation many nucleons contribute coherently to the nuclear rotational motion, resulting in a rotation of an appreciable number of nucleons about an axis different from the symmetry axis [1]. In the simplest approximation the nucleus can be regarded as a rigid body system, which means that one can make use of concepts like the moment of inertia $\Im$, the rotational frequency ω and the angular momentum R. The classical relation $R = \Im\omega$ between these quantities would yield the first estimate of the energy $E = \dfrac{\Im\omega^2}{2} = \dfrac{R^2}{2\Im}$, but, since the real nucleus is a quantum mechanical system, the quantization of the angular momentum R gives rise to discrete rotational states of energies:

$$E = \frac{\hbar^2}{2\Im} R(R+1), \qquad R = 0,\ 2,\ 4,\ 6,\ ... \tag{1.11}$$

On the other hand, in spherical or little deformed nuclei, the alignment of the individual nucleonic orbitals along the nuclear symmetry axis appears to be a mechanism preferred to build up angular momentum. This is the case of non-collective rotation.

The two different kinds of nuclear spin can be clearly seen in the experimental level schemes: in the case of collective rotation the nucleus follows a regular de-excitation pattern with deviations at frequencies at which the Coriolis force destroys the correlations between a pair of nucleons. On the contrary, for spherical nuclei the individual nucleonic motion dominates, producing a very irregular energy spectrum, as can be seen in Fig. 1.4.

Even if well deformed, the nucleus does not rotate as a rigid body, but collective and single particle degrees of freedom coexist and compete in the same nuclear system. This happens when the single-particle alignment i starts to contribute to the angular momentum I. The previous considerations suggest that the total angular momentum I of the nuclear system can be written as the sum of the collective rotational part R and the part i of the angular momentum carried by the

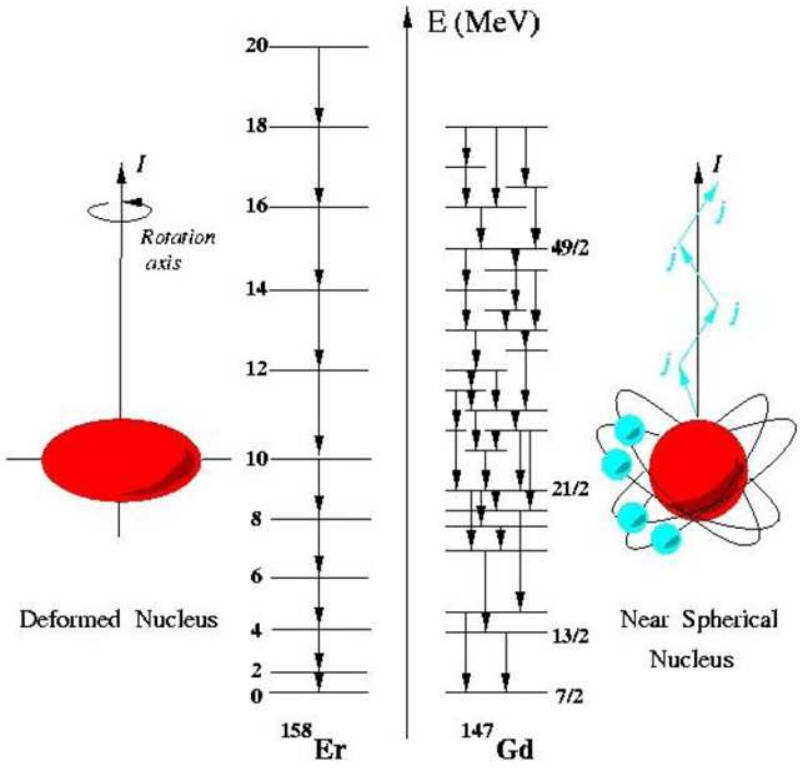

Figure 1.4: Partial level schemes for ^{158}Er and ^{147}Gd. In the case of ^{158}Er the angular momentum I is produced by the collective rotation at low values of angular momentum (left panel of the picture). At greater angular momentum values, also the quasi-particle alignments contribute to the total angular momentum. In the case of ^{147}Gd, the nucleus has an almost spherical shape, and the total angular momentum can only be generated by single nucleons (right panel).

single particle motion, according to the classical relation:

$$\vec{I} = \vec{R} + \vec{i} = \Im^{(2)}\vec{\omega} + \vec{i} \tag{1.12}$$

Here ω and $\Im^{(2)}$ are the rotational frequency and the so-called second (or dynamical) moment of inertia of the system, which expresses the collective properties of the nucleus. The energy of the rotating system can be written as:

$$E(I) = \frac{\hbar^2}{2\Im^{(2)}} R(R+1) + E(i) \tag{1.13}$$

which means that for high values of the angular momentum the largest part of the excitation energy is confined in the rotational degree of freedom. This also implies that the energy of the quadrupole γ-ray transition (E2, $\Delta I = 2\hbar$) becomes linearly dependent on the angular momentum I:

$$E_\gamma = E(I+2) - E(I) = \frac{\hbar^2}{2\Im^{(2)}}(4I - 2) \approx \frac{2\hbar^2}{\Im^{(2)}} I \tag{1.14}$$

while the difference between two consecutive transitions is spin independent:

$$\Delta E_\gamma = E_\gamma(I+2) - E_\gamma(I) = \frac{4\hbar^2}{\Im^{(2)}} \tag{1.15}$$

As a consequence, γ-rays proceeding through regular rotational bands are expected to form very specific patterns in two-dimensional (2D) coincidence spectra, as discussed later in Sec 1.6.

The interplay between collective and single-particle motion gives rise to a variety of moments of inertia, alignments and branching ratios, that one can measure and compare with detailed calculations. For the moment of inertia, the most straightforward distinction can be made between the kinematic and dynamical values [18]: the kinematic moment of inertia $\Im^{(1)}$ is defined as the first derivative of the rotational energy with respect to spin

$$\Im^{(1)} = \hbar^2 I \left(\frac{dE}{dI} \right)^{-1} = \frac{\hbar I}{\omega} \tag{1.16}$$

and it is related to the motion of the system; the dynamic moment of inertia $\Im^{(2)}$ is instead defined as the second derivative of the rotational energy

$$\Im^{(2)} = \hbar^2 \left(\frac{d^2 E}{dI^2} \right)^{-1} = \hbar \frac{dI}{d\omega} \tag{1.17}$$

and it has to do with the way the system responds to a force.
From the previous equations one obtains a relation between $\Im^{(1)}$ and $\Im^{(2)}$:

$$\Im^{(2)}(\omega) = \Im^{(1)}(\omega) + \omega \frac{d\Im^{(1)}(\omega)}{d\omega} \tag{1.18}$$

which becomes, in the case of rigid rotation (that is when $\Im^{(1)}$ is constant):

$$\Im^{(2)} = \Im^{(1)} = \Im_{rigid} \tag{1.19}$$

The equality between $\Im^{(1)}$ and $\Im^{(2)}$ holds only when the total energy of the system can be given by a simple expression like Eq. 1.11, with $\Im$ constant and equal to the moment of inertia of a rigid rotor, as follows from Eq. 1.18 and 1.19. In general $\Im^{(1)}$ and $\Im^{(2)}$ assume different values in rotating nuclei, and they both depend on the angular momentum I.
In defining moments of inertia it should also be recognized that the nucleus may increase its spin I in two ways, with collective or non-collective degrees of freedom. In a collective rotation the angular momentum increases regularly along a particular rotational band, as a function of the rotational frequency, while the intrinsic configuration is not changed. In this case the appropriate moment of inertia are $\Im^{(1)}_{band}$ and $\Im^{(2)}_{band}$, which are associated with the collective properties of the band. If all nucleons were participating in a rigid rotation, the collectivity would be maximum and $\Im^{(1)}_{band} = \Im^{(2)}_{band} = \Im_{rigid}$.
In most cases, however, the nucleus changes its intrinsic structure with increasing angular velocity, and gains angular momentum at the band crossings due to the single-particle alignments from nucleons which have a motion decoupled from the collective rotation. In this case the overall variation of the angular momentum I with frequency ω is characterized by the envelope of the various bands in the (E vs I) plot. The appropriate moments of inertia are then indicated by the effective moments $\Im^{(1)}_{eff}$ and $\Im^{(2)}_{eff}$.
The relation between the band and the effective moments of inertia can be easily found differentiating Eq. 1.12 with respect to the rotational frequency ω:

$$\frac{dI_{tot}}{d\omega} = \frac{dI_{band}}{d\omega} + \frac{di}{d\omega} \tag{1.20}$$

where dI_{band} corresponds to the collective motion an di is coming from the alignment of few specific orbitals. Since $\frac{dI_{tot}}{d\omega}$ includes both collective and alignment

effects, one obtains:

$$\Im^{(2)}_{eff} = \Im^{(2)}_{band} + \hbar\frac{di}{d\omega} \tag{1.21}$$

leading to the results:

$$\Im^{(2)}_{band} \begin{cases} = \Im^{(2)}_{eff}, & \text{for } \dfrac{dI_{tot}}{d\omega} = 0 \\ < \Im^{(2)}_{eff}, & \text{for } \dfrac{dI_{tot}}{d\omega} > 0 \end{cases} \tag{1.22}$$

The first relation expresses the simple situation in which the nuclear excitation follows the band coinciding with the envelope, called ground state band, while the second inequality follows from the definition, that is that the inverse curvature of the envelope is always larger than that of the bands.
The concepts of band and effective moments of inertia are particularly useful in high-spin studies because they can be extracted from the experimental γ ray energy spectra, on the basis of formulas 1.14 and 1.15:

$$E_\gamma = E(I+2) - E(I) = \frac{dE}{dI}\Delta I = \frac{\hbar^2}{2\Im^{(1)}_{eff}} 4I \tag{1.23}$$

$$\Delta E_\gamma = \frac{dE_\gamma}{dI}\Delta I = \frac{d^2E}{dI^2}(\Delta I)^2 = \frac{8\hbar^2}{2\Im^{(2)}_{eff}} = \frac{4\hbar^2}{\Im^{(2)}_{eff}} \tag{1.24}$$

where $\Delta I = 2\hbar$ (since we consider quadrupole transitions).
It should also be noticed that the only observable required to deduce $\Im^{(2)}_{eff}$ is ΔE_γ, which is independent on the angular momentum. This is the basis of the $\gamma - \gamma$ coincidence technique, discussed in Sec. 1.6.1.

Another important quantity that characterizes a nucleus with quadrupole deformation is the intrinsic quadrupole moment Q_t, which can be written in terms of the deformation parameters [19]:

$$Q_t = \frac{3}{\sqrt{5\pi}} Z R_0^2 \beta (1 + 0.16\beta) \tag{1.25}$$

As one can see, the intrinsic quadrupole moment Q_t is proportional to β only to the first order, although for β values typical of well deformed nuclei ($\beta \sim 0.3$), the higher order terms are rather small. In particular, for rare-earth nuclei with stable deformation, the quadrupole moment Q_t is $\sim 7eb$ [17].
An estimate of the intrinsic quadrupole moment Q_t can be obtained from the study

of the strength of the rotational decay, given by the reduced transition probability $B(E2)$:

$$B(E2; J_i \to J_f) = \frac{5}{16\pi} e^2 Q_t^2 \langle J_i 020 | j_f 0 \rangle^2 \tag{1.26}$$

For transitions $2^+ \to 0^+$, typical of even-even deformed nuclei, the reduced transition probability is:

$$B(E2; 2^+ \to 0^+) = \frac{5}{16\pi} e^2 Q_t^2 \tag{1.27}$$

and it can reach several hundreds of units of single-particle. This depends on the fact that $B(E2; 2^+ \to 0^+) \sim \beta^2$, since $Q_t \propto \beta(1+0.16\beta)$. The large values of β that characterise deformed nuclei ($\beta \sim 0.3$) with respect to spherical nuclei ($\beta \sim 0.05$) can then lead to an increase of one or two orders of magnitude in the value of B(E2). In the high spin limit, relation 1.27 reduces to the simple expression [20]:

$$B(E2; I \to I-2) = \frac{5}{16\pi} \frac{3}{8} e^2 Q_t^2 \tag{1.28}$$

The value of B(E2), and then the value of the intrinsic quadrupole moment Q_t, can be obtained from the measurement of the lifetime τ of an excited level in a rotational band. For a state that decays through an E2 γ transition of energy E_γ, the reduced transition probability can be written as:

$$B(E2) = \frac{0.08156 B_\gamma}{E_\gamma^5 \tau (1 + \alpha_{tot})} e^2 b^2 \tag{1.29}$$

where B(E2) is given in $e^2b^2 = 10^4 e^2 fm^2$ units, when E_γ is given in MeV and τ in ps. The term B_γ and α_{tot} represent, respectively, the γ decay probability with multipolarity E2 and the electronic conversion decay probability. In the case of γ decay from high spin levels, one can assume $B_\gamma \sim 1$ and $\alpha_{tot} = 0$, which gives:

$$\tau = \frac{0.08156}{B(E2) E_\gamma^5} \times 10^{-12} s \tag{1.30}$$

Eq. 1.29 and 1.30 represent the basic relations that show that the study of the lifetime is useful to obtain information on the collectivity of the nucleus. For a nucleus characterised by a strong collective rotational motion, that is with a value of $B(E2)$ between 10^2 and 10^3 *W.u.*, one obtains a lifetime between 10^{-9} and 10^{-15} s.

1.4 The damping of the rotational motion

Studies of several deformed nuclei of the rare-earth region have shown the existence of discrete rotational bands built on specific intrinsic single-particle configurations, up to few hundreds keV of internal excitation energy U above the yrast line. At increasing values of U (up to $U \sim 1\ MeV$), several rotational bands are found to exist, although their low intensity of population makes difficult to resolve them individually. Above $U \sim 1\ MeV$, because of the high level density and of the residual interaction among different rotational states, these bands become strongly mixed [3].

This picture has been formulated in the model of the damping of the rotational motion [21], assuming that the rotational bands are mixed in more complicated states by the presence of a small residual interaction not included in the pure rotational bands descriptions, based on a mean field. Such a mixing produces a fragmentation of the E2 transition probability, which is then distributed over a number of final states. The width of the corresponding B(E2) distribution is called rotational damping width, Γ_{rot}. The transition from the undamped to the damped regime is expected to occur gradually and continuously around an excitation energy denoted by U_0, as schematically illustrated in Fig. 1.5.

Schematic calculations based on the Cranked Shell Model allow to estimate both the value of U_0 at which rotational damping sets in, and the value of the damping width Γ_{rot}, which turns out to be determined by two quantities: first the average dispersion $\Delta\omega$ of the rotational frequency of the unperturbed rotational states; second the time τ in which the compound nucleus stays in a single configuration. The latter quantity is related to the energy range in which the rotational bands interact through the residual interaction:

$$\tau = \frac{\hbar}{\Gamma_\mu} \tag{1.31}$$

where Γ_μ is the width of the intrinsic configuration on which the rotational band is built. The values of Γ_{rot} have been obtained for three different regimes: at low excitation energy U, near the yrast line, the residual interaction is not strong enough to mix the states of the rotational bands.

This is due to the fact that the spacing d_2 among the levels is greater than their

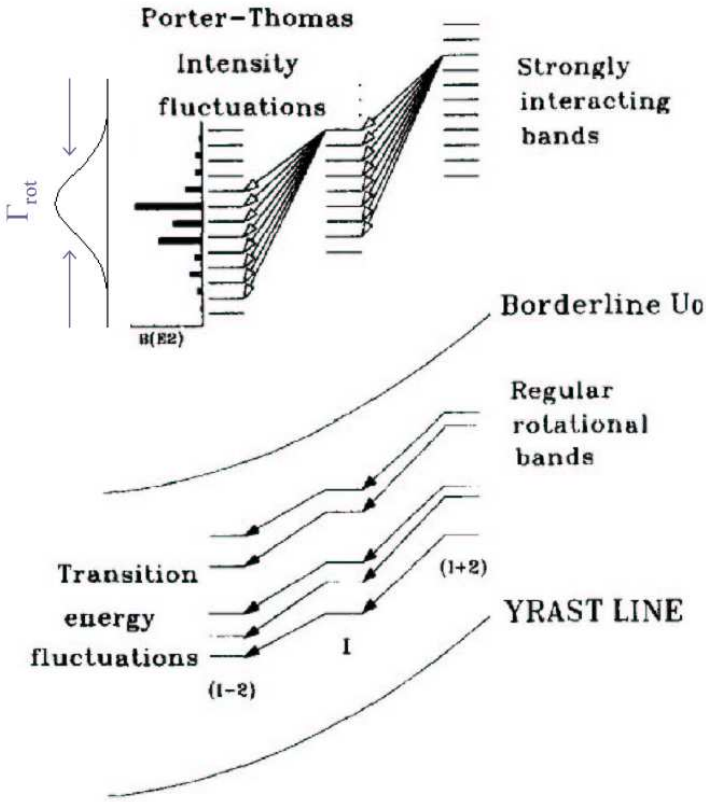

Figure 1.5: Schematic illustration of the rotational quadrupolar decay, as a function of spin and energy. In the low part of the figure, between the yrast line and the borderline U_0, the de-excitation of the nucleus follows regular rotational bands and in the upper part, above U_0, strongly interacting bands create a fragmentation of the B(E2) over many final states [8].

intrinsic width Γ_μ. In this case

$$\Gamma_{rot} \approx 0, \qquad \Gamma_\mu \leq d_2 \tag{1.32}$$

The relation above indicates that in this region the damping of the rotational motion does not exist and that the condition $\Gamma_\mu \leq d_2$ defines the excitation energy range where one can observe discrete rotational bands. If $2\Delta\omega_0 \gg \Gamma_\mu$, that is in an intermediate region of excitation energy, the reduced transition probability B(E2) assumes a Gaussian shape, with $\sigma = 2\Delta\omega_0$ and

$$\Gamma_{rot} \approx 2\sigma = 2(2\Delta\omega_0), \qquad 2\Delta\omega_0 \gg \Gamma_\mu \tag{1.33}$$

This means $\Gamma_{rot} \gg \Gamma_\mu$.
If, in the end, $2\Delta\omega_0 \ll \Gamma_\mu$ (condition predicted for very high values of internal energy U), one obtains a reduced transition probability B(E2) of Breit-Wigner shape, with a width

$$\Gamma_{rot} = \frac{2(2\Delta\omega_0)^2}{\Gamma_\mu}, \qquad 2\Delta\omega_0 \ll \Gamma_\mu \tag{1.34}$$

This means that $\Gamma_{rot} \ll \Gamma_\mu$ and that the width of the damping of the rotational motion decreases as a function of Γ_μ, and therefore of the excitation energy U.
From the knowledge of d_2, $\Delta\omega_0$ and Γ_μ as a function of the internal energy U it is possible to give an estimate of the rotational damping width, as follows:

$$\Gamma_{rot} = \begin{cases} 0, & \text{for } \Gamma_\mu \leq d_2 \\ 0.13\ \dfrac{I}{40}\left(\dfrac{A}{160}\right)^{-5/2}\left(\dfrac{\beta}{0.3}\right)^{-1} U^{1/4} MeV, & \text{for } 2\Delta\omega_0 \gg \Gamma_\mu \\ 0.22\left(\dfrac{I}{20}\right)^2\left(\dfrac{A}{160}\right)^{-13/3}\left(\dfrac{\beta}{0.3}\right)^{-2} U^{-1} MeV + & \\ \quad + 4.4\cdot 10^{-4}\left(\dfrac{A}{160}\right)^{-5/2}\left(\dfrac{\beta}{0.3}\right)^{-2} U^{3/2} MeV, & \text{for } 2\Delta\omega_0 \ll \Gamma_\mu \end{cases} \tag{1.35}$$

Accurate investigations of the damping model have been performed, making use of the microscopic band mixing calculations for the ^{163}Er nucleus (cfr. Ref. [4]), confirming the general trend predicted by the above expression.

Microscopic calculations have been carried out for several normal deformed (ND) and super deformed (SD) nuclei in different mass regions, showing large variations in the rotational damping width, while more or less similar values, of the order of $\sim 50\ keV$, are predicted for the compound nucleus width, which is always found to be smaller than Γ_{rot} [22].

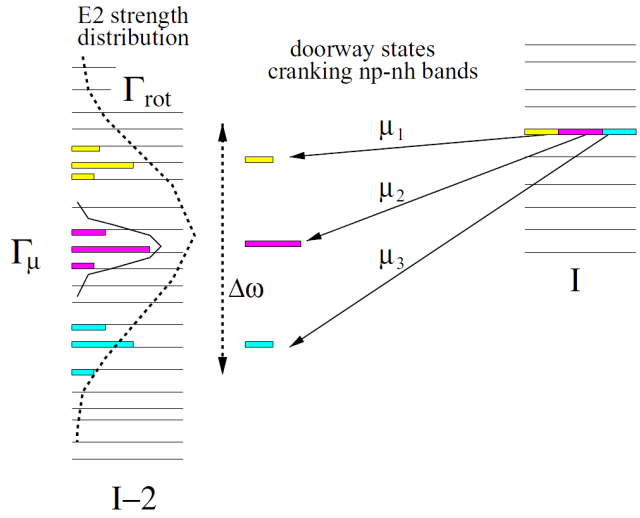

Figure 1.6: Schematic illustration of the fragmentation of the rotational E2 strength from a state at spin I to a number of final states at spin $I-2$, as a consequence of the complex nature of the compound nucleus states. The horizontal bars represent the energy levels at spin I and $I-2$. The thick bars represent the strength of cranked shell model np-nh states [4].

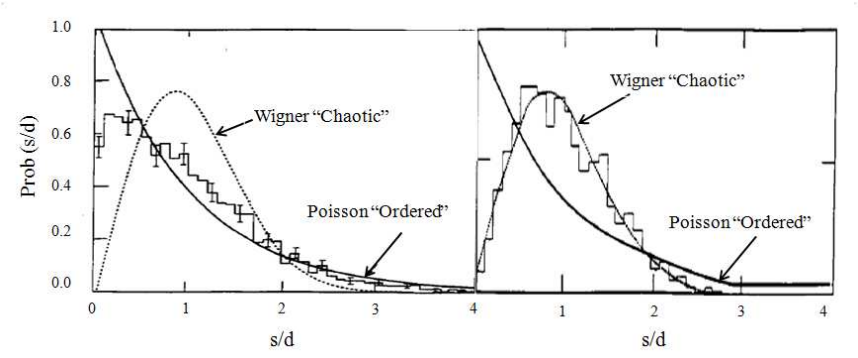

Figure 1.7: Comparison between level-spacing distributions for different regimes: (left) system with ordered behaviour and (right) chaotic system. Figure adapted from Ref. [2].

1.5 Order-to-chaos transitions

The transition between order and chaos in a quantum mechanical system is a fascinating subject that is currently investigated in different research fields, ranging from nuclear to atomic, molecular and solid-state physics.

The atomic nucleus is one of the best examples of a finite many-body quantum system for which the interplay between collective and single-particle degrees of freedom can be used to probe the gradual evolution of the system toward a chaotic regime.

Close to the yrast line nuclear states are in fact characterized by quantum numbers. Therefore, the transitions between nuclear levels are governed by selection rules and the distribution of the levels reflects that of an ordered system (see left panel of Fig. 1.7). On the other hand, around the particle emission threshold ($\approx 7 - 8\ MeV$ above yrast) the only quantum numbers surviving are spin, energy and parity, and the nucleus can be described as a chaotic system (see right panel of Fig. 1.7) [2, 23].

A useful probe to study the evolution of selection rules with excitation energy is the K quantum number, being K the projection of the angular momentum on the symmetry axis of a deformed nucleus (see Fig. 1.8).

At low excitation energies, close to the yrast line, K is a well defined quantity with selection rules governing the decay between various nuclear configurations. In par-

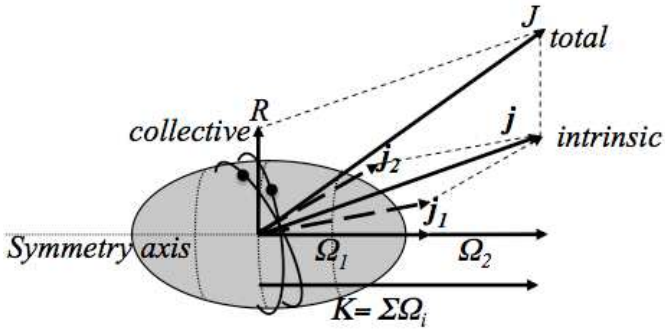

Figure 1.8: Schematic representation of the generation of angular momentum in a deformed rotating nucleus (see text for details).

ticular, the approximate conservation of the quantum number K is responsible for the existence of long lived high-spin isomers in deformed prolate systems, exhibiting strong hindrances to decay to low-K ground states by transitions with multipolarity smaller than the change in K value. These are the so-called K-isomers, which are particularly abundant around mass $A = 180$ [10, 24].

1.5.1 K isomers

Since no collective rotation R is allowed for a quantum rotor about its axis of symmetry, any projection of the total angular momentum J of the nucleus along its symmetry axis necessarily has to originate from the intrinsic angular momenta j of individual valence nucleons in their respective orbitals (see Fig. 1.8).

For a deformed nucleus in the shape of a prolate spheroid, collective rotation about a short axis (perpendicular to the long symmetry axis) is the most energetically favoured mode for generating angular momentum. If valence orbitals with large projections Ω of the intrinsic nucleonic angular momenta j along the symmetry axis are available, they provide an alternate mechanism for angular momentum generation in the nucleus. In specific regions of the nuclear chart, where high-Ω orbitals are available near the Fermi surface for both protons and neutrons, high-K ($K = \sum \Omega_i$) multiquasiparticle configurations of broken nucleon pairs become energetically favorable. In these nuclei, the two modes of generating angular momentum are (i) collective rotation perpendicular to the symmetry axis, and (ii)

coupled nucleonic angular momentum with large projections along the symmetry axis (see Fig. 1.8).

The $A \sim 180$ mass region of Hf, W and Os nuclei ($Z = 72,\ 74,\ 76$) is rich in high-K isomers, since multiple high-K orbitals are available near the Fermi surface for both protons and neutrons.

Transitions with $\Delta K > \lambda$, the multipolarity of the decay transition, are forbidden to first order and proceeds via higher order corrections. If the transition multipolarity is subtracted from the change in K resulting from the transition, then the degree of forbiddenness, $\nu = \Delta K - \lambda$, is obtained. Loebner [25] found that, empirically, for each extra unit of forbiddenness, the transition rate reduces by a factor of about 100, which may be expressed as $f_\nu = F_W^{1/\nu} \approx 100$ (here F_W is the ratio of the Weisskopf estimate to the measured transition rate). Therefore, these quantities are related by the expression

$$f_\nu = F_W^{1/\nu} = \left(\frac{T_{1/2}^{\gamma}}{T_{1/2}^{W}} \right)^{1/\nu} \tag{1.36}$$

where $T_{1/2}^{\gamma}$ is the partial γ-ray half-life and $T_{1/2}^{W}$ is the corresponding Weisskopf single-particle estimate.

Previous studies have shown that the reduced hindrance appears to be very small ($2 < f_\nu < 10$) as compared to empirical rule of Loebner ($f_\nu = F_W^{1/\nu} \approx 100$), calling into question the validity of the K quantum number, and leaving open the question of how to understand K-isomers half-lives.

One possible explanation to this phenomenon invokes two different kinds of K mixing [24]. One is a Coriolis effect that perturbs the states to which an isomer decays (such states typically involve rapid collective rotation). The other effect depends on the excitation energy of the isomer: it has been demonstrated that, for certain isomer decays, there is a systematic decline in reduced hindrance as the difference increases between the isomer excitation energy and the expected energy of a typical rotational state of the same spin. This correlation (see Fig. 1.9) can be explained by a statistical K mixing that depends on the density of states [10]. States with the same spin as the isomer, but having lower K values, are assumed to mix with the isomeric state and to introduce low-K components into the high-K isomeric state. The rapid increase in the number of such states per unit energy interval, as the excitation energy of the isomer increases, can be used to estimate

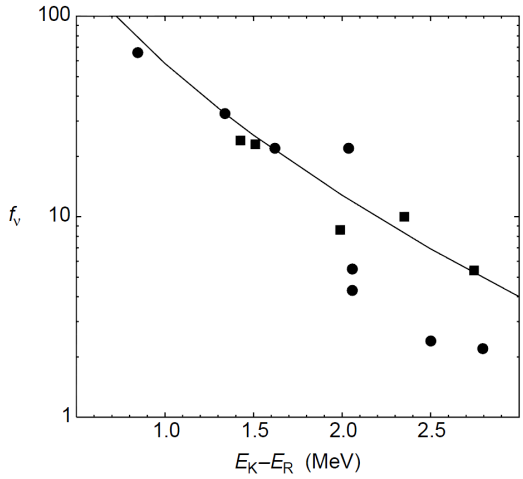

Figure 1.9: Reduced hindrance for selected K-forbidden transitions, as a function of excitation energy relative to a rigid rotor with the same angular momentum. Symbols refer to data, while the line represents a statistical model estimate based on the density of states [24].

the energy dependence of the declining reduced hindrance f_ν, as shown by the line in Fig. 1.9. It is found that there are several reduced-hindrance values which fall significantly below this density-of-states estimate: this can be explained by the additional influence of the Coriolis effect, as mentioned above.
The outcome is that the decay from lower excitation energy high-K states is more retarded indicating less K mixing between initial and final states. In other words, the K-quantum number progressively loses its meaning with increasing excitation energy [4, 24]. The onset of this chaotic behaviour is not yet fully established and in particular its dependence on the internal energy of the system is still to be clearly defined [4, 16, 26, 27].

The robustness of K with excitation energy can be also investigated by quasi-continuum γ-spectroscopy of deformed nuclei produced by heavy ion fusion-evaporation reactions. This reaction mechanism allows to populate warm rotating nuclei at high spin and excitation energy values, which de-excite by emission of long γ-decay cascades, all the way down to the yrast line. In this way, one can probe the entire excitation energy-spin region where the onset of K-mixing, i.e. of the chaotic

regime, is expected to take place.
In this respect, the only nucleus investigated in great details, over a wide interval of spin and excitation energy, is ^{163}Er [4, 16, 26], from which the conservation of selection rules on the K quantum number has been established up to internal excitation energy $U \sim 1.5 - 2\ MeV$. In this case, calculations predict a full transition into a chaotic regime above 2.5 MeV of internal excitation energy. This could not be observed in the work of Ref. [4, 16, 26], mostly due to the limited angular momentum and excitation energy given by the fusion-evaporation reaction employed. Therefore, the energy at which a full transition into the chaotic regime occurs still remains an open experimental question, as well as a more detailed investigation of the excitation energy dependence of the hindrance between low-K and high-K states. For this reason, additional experimental data are highly demanded.
An interesting physics case is represented by ^{174}W, the nucleus studied in this thesis; its main features will be described in Chap. 2.

1.6 γ coincidence analysis techniques

In this section we schematically describe the principle of multidimensional analysis techniques based on γ coincidence measurements. Emphasis is given to the different components of the spectral distributions which are relevant for the quasi-continuum analysis discussed in Chap. 5.

1.6.1 Double γ coincidence spectra

The study of the nuclear rotational motion is based on the analysis of $\gamma - \gamma$ coincidence spectra. In fact, each coincidence between two γ rays of energy $E_{\gamma 1} = i$ and $E_{\gamma 2} = j$ increments counts in channel (i, j) in a $\gamma - \gamma$ matrix.
In the case of the de-excitation of rotational nuclei, a large number of coincidences belonging to the same rotational band is produced. As a consequence, the two-dimensional spectrum exhibits a ridge-valley structure that allows to distinguish regions populated by damped transitions from the ones populated by regular rotational bands.
In order to understand how counts distribute in the $\gamma - \gamma$ matrix, Fig. 1.10 is considered:

1. *Single rotational band*: if only a single band is present (Fig. 1.10a), the cascade is characterised by a defined sequence of transition energies. Coincidence counts lay on a regular grid (Fig. 1.10 b) with no counts in the diagonal, since it is not possible to have, in the same band, transitions with the same energy, as follows from Eq. 1.14. By selecting a region orthogonal to the diagonal, a regular distribution of peaks can be observed (Fig. 1.10 c). The first ridge next to the diagonal is populated by consecutive transitions, while successive ridges are populated by transitions spaced by one transition and so on. By measuring the distance between two consecutive ridges, using the relation $\Delta E_\gamma = 4\hbar^2/\Im^{(2)}$ it is possible to estimate the dynamical moment of inertia of the band.

2. *Several rotational bands*: if nuclear de-excitation proceeds following a number of rotational bands characterised by different dynamical moment of inertia (Fig. 1.10d), a superposition of many grids (like the one of Fig. 1.10b) takes place and a ridge structure is formed (Fig 1.10e). Making projections on the orthogonal diagonal it can be observed that ridges show a width that depends on the dispersion of the dynamical moments of inertia of the bands. The width increases with $E_{\gamma 1} - E_{\gamma 2}$, while the ridge distance is determined by the average second moment of inertia of bands. The valley is not yet filled.

3. *Damped rotational motion*: in the damping regime, γ rays starting from a single energy level distribute over several final states belonging to different rotational bands (Fig. 1.10g), as a consequence of the fragmented B(E2) probability. Due to the large number of possible final states, each point of the grid is turned into a continuum distribution of width Γ_{rot}, filling even the principal diagonal $E_{\gamma 1} = E_{\gamma 2}$. Projections perpendicular to the diagonal (Fig. 1.10i) show continuum distributions that overlap, making visible only the valley, whose width is related to Γ_{rot}.

The analysis of these spectra has shown how the nuclear rotational motion is the composition of the three regimes already described. It is then possible to separate the contribution given by the regular rotational motion, that forms ridge structure, from the one given by a damped motion which produces a continuum and uniform background filling the valley ($E_{\gamma 1} \approx E_{\gamma 2}$).

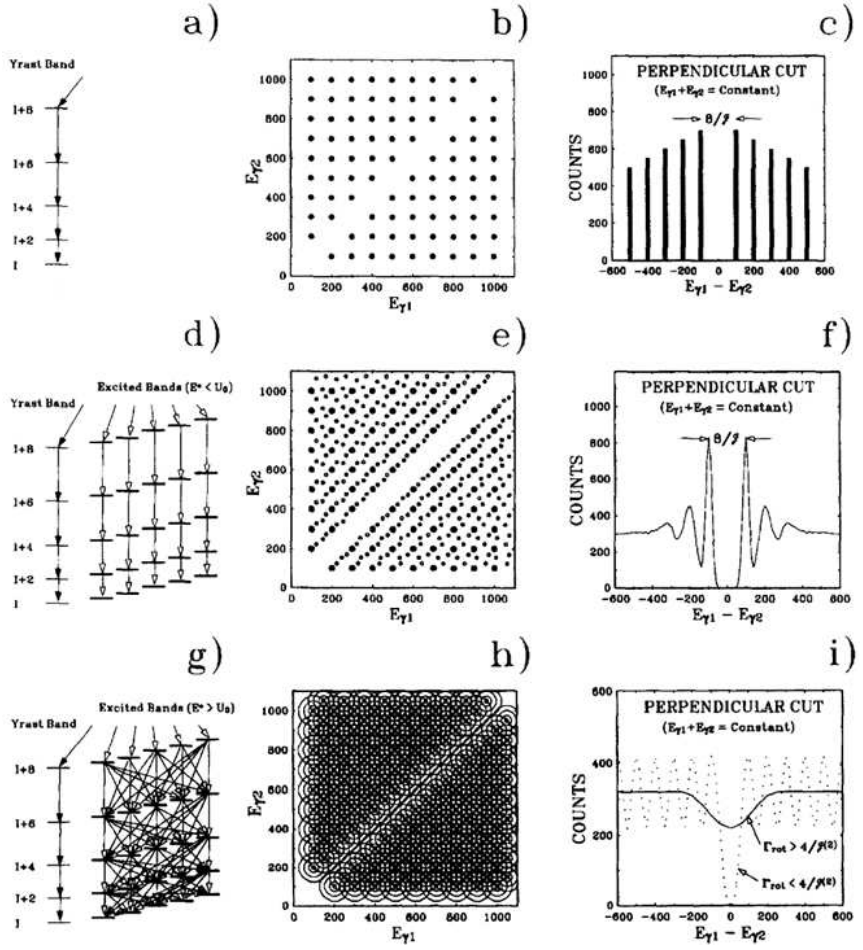

Figure 1.10: This schematic figure shows the three main rotational decay modes (left), the corresponding patterns in the 2D spectra (middle) and the distributions obtained by performing perpendicular cuts for constant energy $E_{\gamma 1}+E_{\gamma 2}/2$ on the 2D spectra (right). Panels a), b) and c) shows the case of one regular rotational band. Panels d), e) and f) display the pattern of ridges generated by an ensemble of bands with variations in moment of inertia. Panels g), h) and i) describe the situation of rotational damping [8].

1.6.2 Rotational planes

Two-dimensional matrices are composed by all possible pairs of energies $E_{\gamma 1}$ and $E_{\gamma 2}$ of an acquired event. On the other hand, if all the possible terns of energies ($E_{\gamma 1}$, $E_{\gamma 2}$, $E_{\gamma 3}$) are considered, it is possible to create three-dimensional (3D) matrices, i.e. cubes, whose points are incremented using the terns as coordinates.

The 3-fold requirement is more selective than the 2-fold one and allows to focus on weaker rotational structures. In particular, some locus of points in these cubes are very useful to study rotational bands. They are the *rotational planes*, defined as

$$x + N \cdot y = (N + 1) \cdot z \tag{1.37}$$

where $N = 1, 2, 3, ...$ is an integer number that selects different types of coincidences along rotational bands, as schematically shown in Fig. 1.11; x is the highest γ-energy, y is the intermediate one and z is the lowest one. The N=1 plane will contain three consecutive γ-ray transitions, or γ-ray number 1, 3 and 5 out of five consecutive, etc.. The N=2 plane will contain γ-ray number 1, 3 and 4 out of four consecutive transitions, and so on [28].

In the sorting of the rotational plane, an uncertainty on z has to be taken into account. The acceptable energies are, in fact, those include in the interval, centred around z, $[z - \delta/2; z + \delta/2]$, being $\delta = 20\ keV$ the expected width of the ridge structure, due to the uncertainty in the moment of inertia $\Im^{(2)}$ (see Sec. 1.6.1). Eq. 1.37, hence, becomes

$$x + N \cdot y = (N + 1) \cdot z \pm \delta/2 \tag{1.38}$$

In this way it is possible to measure quantities related to ridges of order higher than one.

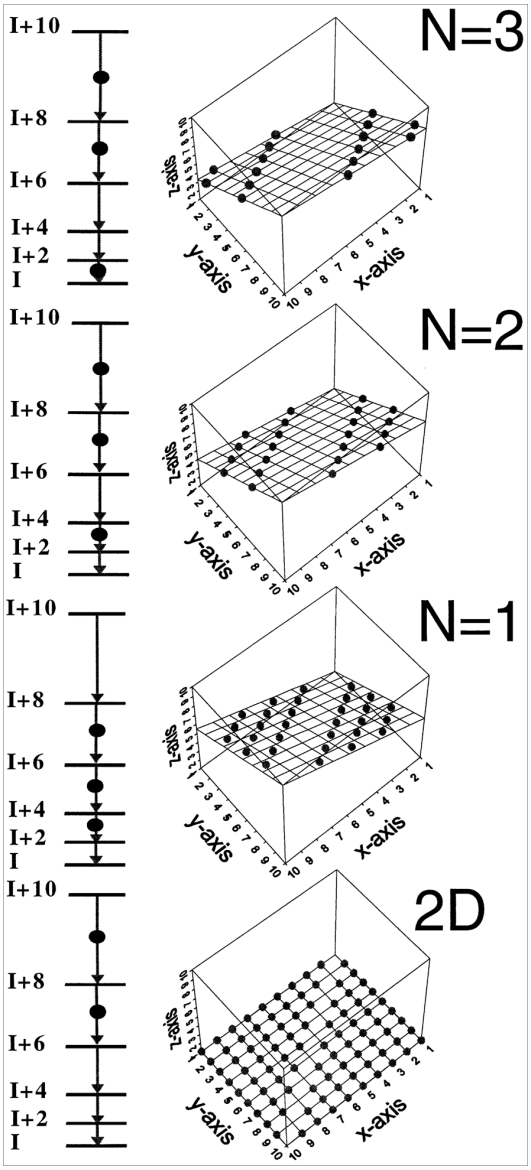

Figure 1.11: Schematic illustration of the rotational correlation patterns forming ridges in both the 2D (bottom) and 3D rotational planes defined by equation 1.37, with N=1, 2 and 3. The coincidence combinations selected by the different planes are indicated by circles in the rotational cascades shown on the left hand side of the figure [28].

Chapter 2

Cranked Shell Model at finite temperature

Simulation codes are often used to study the properties of the quasi-continuum component of the γ decay of rotational nuclei [29].
In Chap. 6 we will discuss in detail the *MONTESTELLA* code which has been used in the analysis of the ^{174}W nucleus discussed in this thesis. The code is based on the microscopic Cranked Shell Model (CSM) calculations presented in this Chapter, especially developed to describe in great details the properties of the nuclear rotational motion as a function of temperature. The use of these microscopic calculations as a input of Monte Carlo simulations of the γ-cascades allows us to sharpen the comparison between data and model prediction. In particular, in contrast to more schematic calculations, a simulation using microscopic calculations allows to use analysis techniques based on count fluctuations (see Chap. 5).
The main properties of ^{174}W, the nucleus investigated in this thesis, will be presented in Sec. 2.1, while in Sec. 2.2 and 2.3 the general properties of the CSM calculations will be discussed, also in connection with the specific case of ^{174}W.

2.1 Properties of the nucleus ^{174}W

Total Routhian Surfaces (TRS) calculations indicate that the nucleus ^{174}W exhibits an axially symmetric prolate shape over the range of observed rotational frequen-

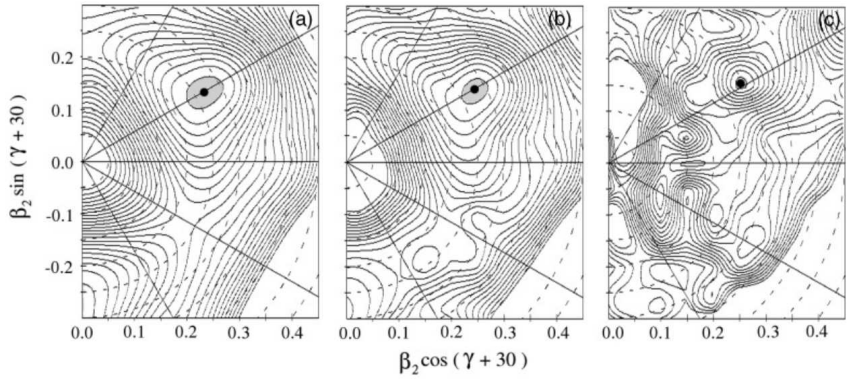

Figure 2.1: Total Routhian surfaces for ^{174}W at (a) $\hbar\omega = 0.0\ MeV$, (b) $\hbar\omega = 0.25\ MeV$, and (c) $\hbar\omega = 0.50\ MeV$. It is evident that an axially symmetric prolate shape (indicated by the shaded region and a black dot) is the lowest energy minimum up to high rotational frequencies [5].

cies [5]. The calculations were performed for frequencies ranging from $\hbar\omega = 0.0$ to $0.5\ MeV$ and the results are summarized in Fig. 2.1.

It is evident that the prolate energy minimum persists for the indicated rotational frequencies; this results is important, being the basis of our microscopic calculations, as it will be explained later in this Chapter.

^{174}W is characterised by low-K and high-K bands, extending up to spin $39\hbar$. Fig. 2.2 and 2.3 show partial level schemes, known from literature [5, 6]. In particular, two high-K bands are built on isomeric states: bands 15-16 ($K = 8$) are built on a level with 158 ns lifetime, while bands 17-18 ($K = 12$) are built on a 128 ns state, as indicated in Fig. 2.3. This feature will be the key-point for the experimental analysis discussed in Sec. 4.4. The excitation energy above the yrast line of the bandhead of the high-K structure is 1130 keV for bands 15-16 and 1328 keV for bands 17-18.

The K-forbidden decay from high-K to low-K states has been investigate in a systematic manner in this nucleus, as well as in other Hf, W and Os nuclei in the mass region $A \sim 180$ [5, 10].

One of the early mechanisms proposed to explain the unusually reduced hindrances for these K-forbidden decays was a tunnelling of the nucleus through a barrier in the γ degree of freedom [30] along a line of constant β deformation. The key param-

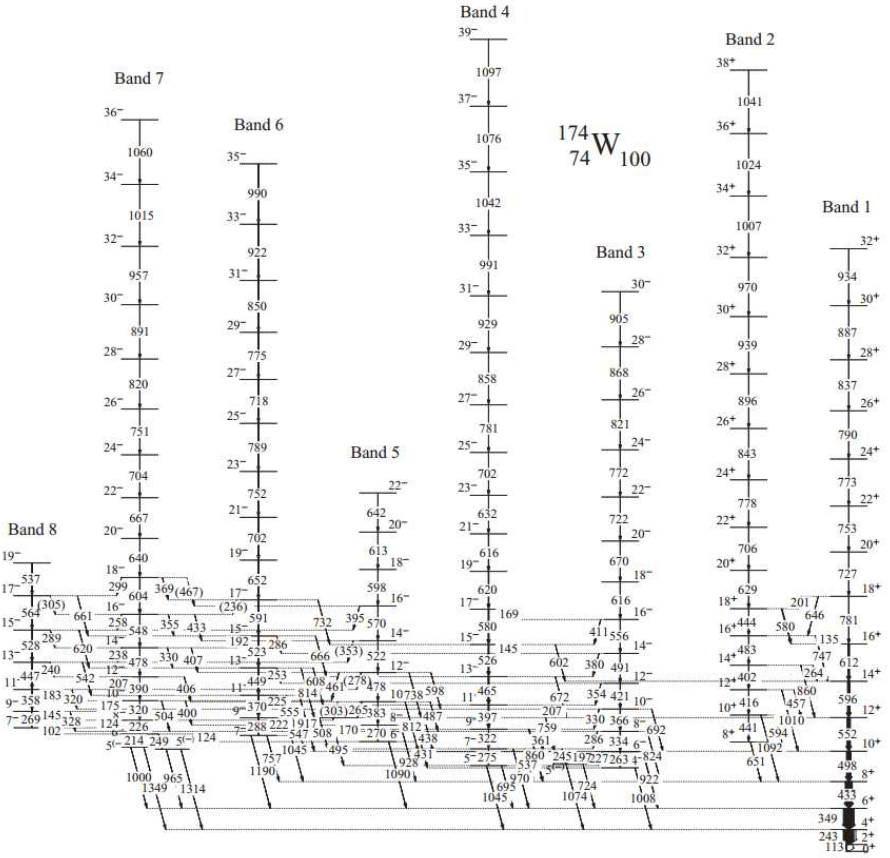

Figure 2.2: Partial level scheme for the ^{174}W nucleus, showing the yrast band (Band 1) and low-K ($K \leq 6$) bands [6].

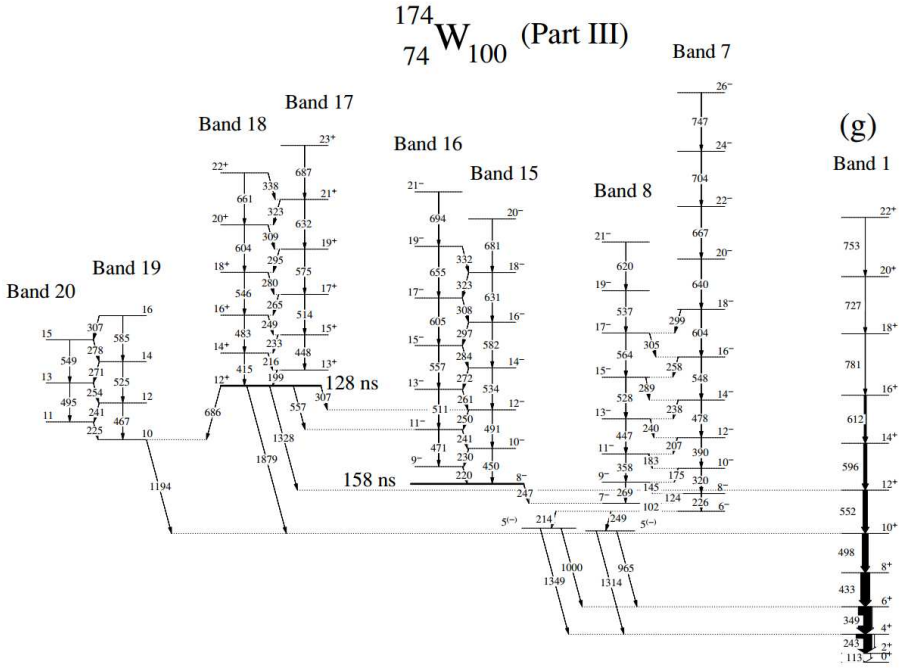

Figure 2.3: Partial level scheme for the ^{174}W nucleus, showing the known high-K bands at the band head (Bands 15 to 20) and their decay pattern. The lifetimes of the isomeric states are also indicated [5].

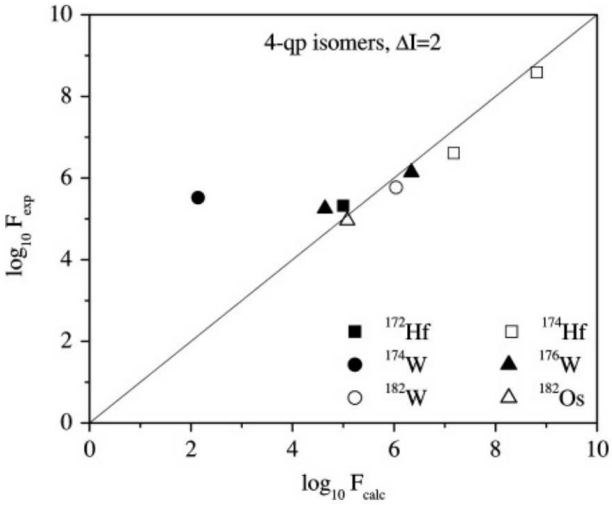

Figure 2.4: Measured vs calculated hindrance F for few selected isomers in the $A \sim 180$ region. The predictions of the γ-tunnelling calculations are in agreement with experiment, except for the case of the $K = 12$ isomer of ^{174}W [5].

eter in this model is the energy barrier along the γ-deformation axis through which the axially deformed nucleus is hypothesized to tunnel from the high-K bandhead (where intrinsic nucleonic spins are aligned along the symmetry axis) to low-K states (where the angular momentum of collective rotation is aligned perpendicular to the symmetry axis). The tunnelling probability T is related to the action W via the simple expression $T \propto \exp -2W/\hbar$ (see Ref. [31] for details).
These calculations, based on the Nilsson-Strutinsky method, have been very successful in describing a large body of isomer decays in this mass region.
These calculations were performed even for the $K = 12$ isomer decay in ^{174}W, giving unexpected results: the measured hindrance factor F_{exp} for the $1879 - keV$ E2 transition from the $K = 12$ isomeric bandhead to the 10^+ state of the ground state band is 7.3×10^5, three orders of magnitude higher than the calculated value F_{calc} of 2.6×10^2, as shown in Fig. 2.4. In the figure, points that fall along the diagonal are those where γ-tunnelling could be sufficient as the primary mechanism for the decay. For points below the diagonal, other decay mechanisms could contribute to lower the measured hindrance values. On the contrary, points far above

the diagonal, where the experimental hindrances are much larger than γ-tunnelling predictions, are not at all understandable within this logic.
Other theoretical models can be employed to explain the hindrance to decay from high- to low-K states: a possible effect which comes in is the K-mixing; this is our possible candidate to explain the experimental value in ^{174}W, as discussed in Sec. 1.5.1.

2.2 Microscopic calculations at finite temperature

The microscopic CSM calculations used in this work are able to describe the individual nuclear levels and their E2 transition probability, extending up in the region where the damping of the rotational motion is dominant ($U > 1\ MeV$ above the yrast line) [9].
In the model the single particle basis is obtained cranking the particle-hole states of a Nilsson potential representing the intrinsic excitations of the rotational nucleus. It is also assumed that each np-nh configuration forms a rotational band and that the two-body residual interaction mixes these configurations.
The Hamiltonian that combines the Nilsson cranked mean field with the two-body residual interaction is given by:

$$H_{tot} = H_{crank} + V_{res} \tag{2.1}$$

where

$$H_{crank} = H_{Nilsson} - \omega_x J_x \tag{2.2}$$

corresponds to the deformed Nilsson potential, rotating with a frequency ω around the symmetry axis with the largest moment of inertia (indicated as x axis). The rotational frequency ω_x is chosen so that the mean expectation value of the angular momentum J_x along the rotational x-axis is equal to the spin I.
Once the Hamiltonian $H_{Nilsson}$ is defined, the basis of the CSM of a many-body system is obtained by filling the cranked orbitals of Nilsson with N neutrons and Z protons. Starting from the configuration in which all the orbitals up to the Fermi surface are occupied, one can build many particle-hole excitations ($np-nh$) that form the shell model basis for the excited states above the yrast line. These

configurations, indicated by μ, at spin I are given by:

$$|\mu(I)\rangle = \prod a_i^\dagger |0\rangle \tag{2.3}$$

where $a_i^\dagger$ represents the creation operator for the wave function $\psi_i(\omega_I)$ of single particle occupied in this configuration.
The energies $E_\mu(I)$ of the states μ at spin I and the many-body wave functions $|\mu(I)\rangle$ define the basis of the CSM at spin I and parity π. Since the states that form the basis depend in a regular way on the rotational frequency, one assumes that each configuration of the basis forms a rotational band on a specific $np-nh$ configuration. The basis states are regarded as unperturbed rotational bands.
A residual interaction among the basis configurations has been introduced of surface-delta type (SDI). The shell model Hamiltonian thus constructed at spin I reads

$$H_{\mu\mu'}(I) = E_\mu(I)\delta_{\mu\mu'} + V_{\mu\mu'}(I) \tag{2.4}$$

where $V_{\mu\mu'}(I) = \langle\mu(I)|V_{res}|\mu'(I)\rangle$ is the matrix elements of the SDI, being:

$$V_{res}(1,2) = v_0 4\pi\delta(r_1 - R_0)\delta(r_2 - R_0)\sum_{\lambda\mu} Y^*_{\lambda\mu}(r_1)Y_{\lambda\mu}(r_2) \tag{2.5}$$

and $v_0 = 27.5/A\ MeV$. The residual interaction is essential to describe the compound states at finite thermal energy and the rotational damping phenomenon since both are caused by mixing among the basis configurations [21, 32]. The states near the yrast line, on the other hand, are less influenced by the residual interaction, and they survive as discrete rotational bands.

2.2.1 Dependence on the K-quantum number

In deriving the Hamiltonian of Eq. 2.4 the K-quantum number has been neglected by applying the angular momentum relation $I = I_x$. If the K-quantum number is taken into account, the $I = I_x$ relation should be modified.
If one considers a rotational band i carrying the K-quantum number K_i, the angular momentum about the rotational x-axis will be given by $I_x = \sqrt{I^2 - K_i^2}$. Denoting by $E_i^{crank}(I_x)$ the rotational energy acquired by the band cranking about the x-axis, the rotational energy taking into account the K-quantum number is given by

$$E_{i,Ki}(I) = E_i^{crank}(I_x) \tag{2.6}$$

In the case of high spin states, that is $I \gg K_i$, or if the dependence on I_x is quadratic as expected from a rigid-body rotation, the above equation can be approximated as

$$E_{i,Ki}(I) = E_i^{crank}(I_x = I) - K_i^2/2\Im_i \tag{2.7}$$

where $\Im_i = I_x(\partial E_i^{crank}/\partial I_x)^{-1} = I_x/\omega_x$ is the kinematic moment of inertia of the band. The second term $-K_i^2/2\Im_i$ represents the effect of the K-quantum number on the rotational energy, which we want to include in the present calculations.
According to these considerations, the shell model Hamiltonian is modified as:

$$H_{\mu\mu'}(I) = E_\mu(I)\delta_{\mu\mu'} + V_{\mu\mu'}(I) - \left(J_z^2\right)_{\mu\mu'}/2\Im_{\mu\mu'} \tag{2.8}$$

The last term is an operator form of the energy correction $-K_i^2/2\Im_i$, where J_z is the angular momentum operator of the constituent nucleons along the symmetry axis z, and $\Im_{\mu\mu'} = (\Im_\mu + \Im_{\mu'})/2$ is the kinematic moment of inertia of the $np-nh$ basis configurations. The new term in the Hamiltonian favours the states with high values of the K-quantum number.

2.3 Cranked Shell Model calculation for the ^{174}W nucleus

The microscopic Cranked Shell Model calculations discussed above provide a set of level characterised by spin, parity and K quantum number, which are given as input to the simulation code *MONTESTELLA* (see Chap. 6).
Numerical calculations have been performed for ^{174}W; 1000 $np-nh$ basis states have been employed with the lowest excitation energies to diagonalize the Hamiltonian for each (I^π) configuration.
While the deformation parameters ϵ_4 and γ were fixed to 0.02 and 0 respectively, the ϵ_2 parameter is extracted by comparison with experimental data. Three different values have been tested: fixed deformation with $\epsilon_2 = 0.237$ or 0.285 and linear deformation defined as interpolation between $\epsilon_2 = 0.237$ at $I = 0\hbar$ and $\epsilon_2 = 0.285$ at $I = 50\hbar$.
The quantities used to set the deformation were E_γ, $\Im^{(1)}$ and $\Im^{(2)}$ as a function of spin; the comparison between CSM calculations and experimental data is shown in Fig. 2.5.

As one can see, though $\Im^{(2)}$ is not so sensitive to changes in ϵ_2, for E_γ and $\Im^{(1)}$ the best agreement is reached using $\epsilon_2 = 0.237$. In fact with $\epsilon_2 = 0.285$ or linear ϵ_2, $\Im^{(1)}$ is too large for $I > 40\hbar$ especially in the case of linear ϵ_2. On the contrary the calculated E_γ is too low with the non-chosen values.

The role of the J_z^2 term in the Hamiltonian of Eq. 2.8 is to allow the existence of low-lying high-K states. In fact, if this term is neglected there are essentially no low-lying high-K states [9].
In the case of ^{174}W, CSM calculations including the J_z^2 term has led to an excess of high-K levels at low excitation energy, as compared to the existing (although scarce) experimental data. For this reason, a quenching factor q (≤ 1) has been added to the J_z^2 term. Higher is the quenching factor, higher is the number of high-K levels as compared to the number of low-K states. Fig. 2.6 shows the number of low-K and high-K levels obtained for $q = 0.5$ (left) and $q = 0.7$ (middle) at spin $I = 20,\ 40,\ 60\hbar$. It is found that the ratio between the number of high-K and low-K states is sensitive to q. As reported in the right panel of Fig. 2.6, there is a variation of a factor of $\sim 2 - 3$ using $q = 0.5$ or $q = 0.7$.
In order to tune the q parameter, the number of paths extracted from experimental data (see the analysis discussed in Chap. 5) has been compared to the calculated number of bands using different quenching factors (i.e. 0.4, 0.5, 0.6 and 0.7).
A calculated rotational band is here defined as a sequence of 2 consecutive transitions exhausting more than 71% of the total E2 decay strength. In practise this corresponds to less than two final states, as defined by the branching condition

$$n_{b,i} = \frac{1}{\sum_j b_{ij}^2} < 2 \tag{2.9}$$

where b_{ij}^2 is the normalised E2 strength function from level i with spin I to level j with spin $I - 2$ (see also discussion in Chap. 5).
By looking at the upper panels of Fig. 2.7 it is difficult to determine the most appropriate value of q due to the reduced sensitivity and to the rather large error bars on experimental data. Even considering averaged values for the calculations (bottom panels) the sensitivity does not improve. Even if all quenching factors give values compatible within the error bars, the curves having $q = 0.5$ and 0.6 lead to a number of bands closer to the experimental expectation values. In fact we tend to esclude $q = 0.7$ because it gives a too low number of low-K bands (panel 2.7 a)

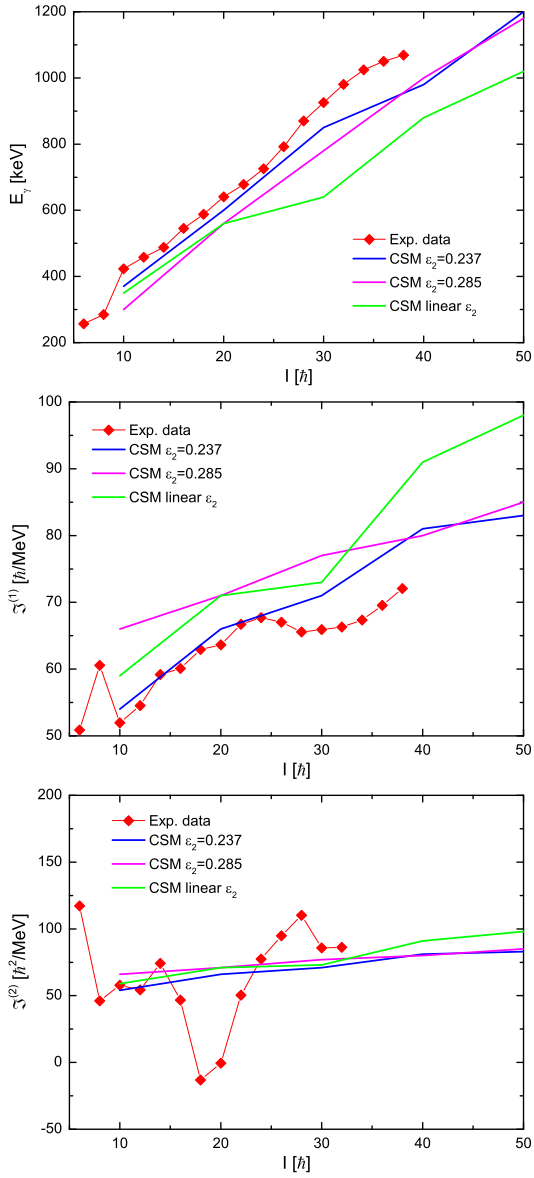

Figure 2.5: Comparison between experimental data and CSM calculations with different deformation parameter ϵ_2, for E_γ, $\Im^{(1)}$ and $\Im^{(2)}$ as a function of spin.

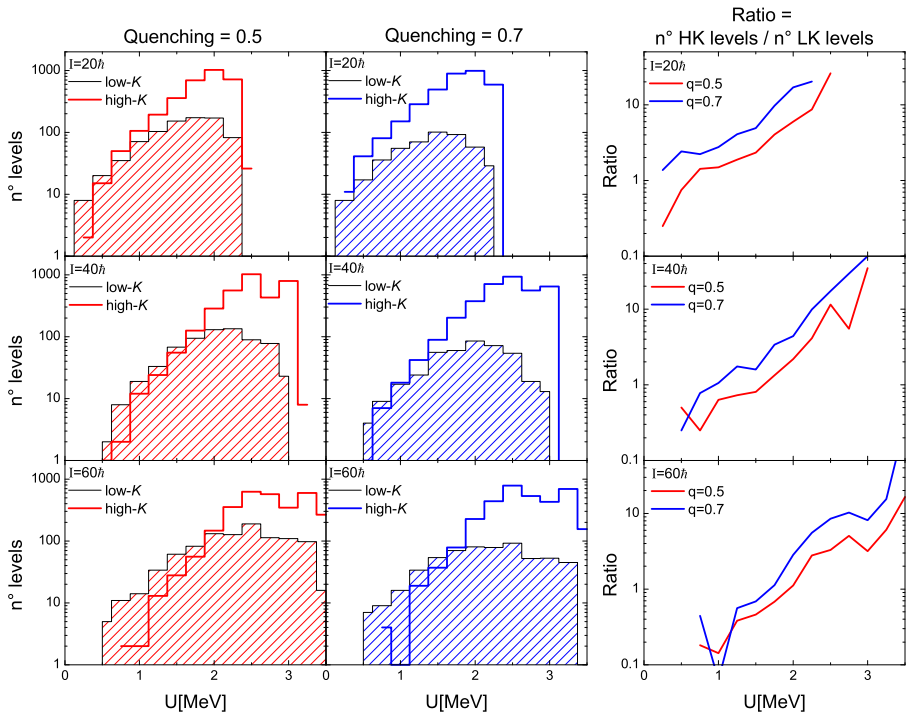

Figure 2.6: Left (center) panel: level density for low and high-K states using $q = 0.5$ ($q = 0.7$). Level density are calculated in steps of 250 keV. Right panel: ratio between the number of high-K and low-K states using $q = 0.5$ (red) and $q = 0.7$ (blue).

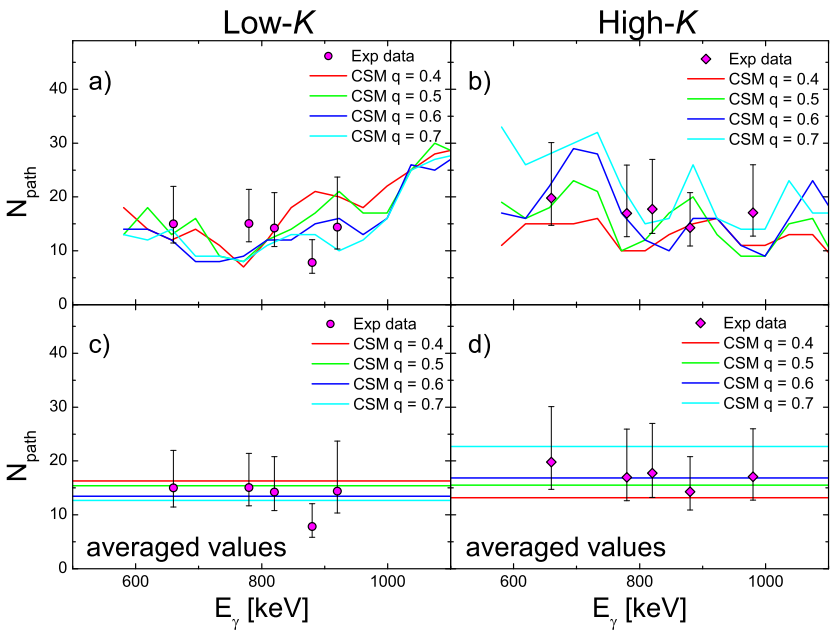

Figure 2.7: Number of bands obtained by the CSM microscopic calculations (coloured lines) compared to the experimental number of decay paths obtained with the analysis procedure described in Chap. 5. Data for low-K (high-K) bands are plotted on the left (right) column. Bottom panels show the theoretical values averaged between 600 and 1000 keV.

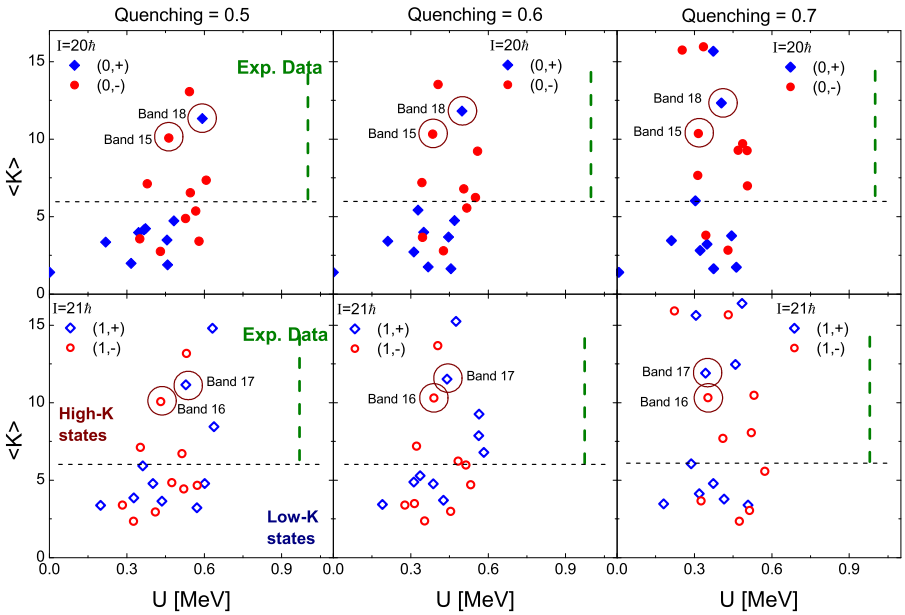

Figure 2.8: Plot of K-values for the lowest 10 states for each parity at spin $I = 20,\ 21\hbar$, as obtained using the CSM with different quenching factors q. From left to right $q = 0.5$, $q = 0.6$ and $q = 0.7$ are used. High-K bands observed experimentally [5] are evidenced by red circles. Vertical green dashed lines indicate the excitation energy of high-K bands, observed in the experimental data [5].

and $q = 0.4$ since it underestimates the nmber of high-K states (panel 2.7 b).
The final choice between $q = 0.5$ and 0.6 has been done by looking at the calculated microscopic levels, reported in Fig. 2.8.

As one can see, $q = 0.7$ is not the best choice since it gives a too small number of low-K ($K \leq 6$) states that is inconsistent with the data: $\sim 20 - 25$ low-K states are measured by experiments [5], but only ~ 18 levels are obtained by calculations. Furthermore the excitation energies of the high-K states ($U \sim 300 - 400\ keV$) are too low and not consistent with data ($U \sim 1000\ keV$, indicated by green dashed lines in Fig. 2.8). Finally, using $q = 0.7$, the model predicts several high-K states with very large values of K ($K > 15$), not experimentally observed.
The situation improves by using $q = 0.6$ although the excitation energy of the high-K states ($U \sim 380 - 500\ keV$) remains still too low.

The best agreement is reached using $q = 0.5$: the excitation energy of the high-K states (indicated by red circles) is still lower than in the experiment ($U \sim 400 - 600\ keV$); however the number of low-K states becomes now closer to the experimental value of $\sim 20 - 25$ low-K bands. It is important to underline that microscopic calculations don't provide a precise correspondence between the single energy levels, especially at low-spin, where pairing effects are relevant, but they are mostly appropriate for a general description of the overall properties of the rotational motion at finite temperature, as already pointed out in Ref. [9].

The energy levels calculated using the parameters here determined ($\epsilon_2 = 0.237$ and $q = 0.5$) in the spin range $I = 10-60\hbar$ are shown in Fig. 2.9 for the spin-parity configuration 0^+. Here the strong stretched E2 transitions forming rotational band structures are evidenced. Many of the states whose excitation energy U relative to yrast is smaller than about 1 MeV form rotational bands, whereas the rotational band structure gradually disappears as U becomes larger than $\sim 1\ MeV$, indicating that rotational damping sets in around this excitation energy.

The average value of K for each energy level i is defined as $\langle K_i \rangle = \sqrt{\langle i|J_z^2|i\rangle}$ in terms of the expectation value of J_z^2. Fig. 2.10 plots the average value of K for each discrete rotational band (i.e. the bands composed by at least two consecutive transitions exhausting more than 71% of the full rotational E2 strength) for different spin ranges (cyan plots) and for the whole spin interval (blue plot). By looking at the latter, in particular, it is found that the distribution of $\langle K \rangle$ shows a concentration of states for $K < 6$, and a rather long tail for $K > 6$, in accordance with the experimental observation of a rather large number of low-K bands with $K < 6$ [5].

Fig. 2.11 shows, in black, the excitation energy U_{onset} above the yrast line at which the onset of rotational damping ($n_b > 2$) sets in. The red curve delimits the excitation energy region ($U < U_{band}$) where microscopic calculations are available. The calculations give values of $U_{onset} \approx 1\ MeV$ and $U_{band} \approx 2.5\ MeV$

Excitation energy spectra calculated for low-lying discrete bands of ^{174}W are shown in Fig. 2.12, for each spin-parity configuration. They are obtained by selecting levels connected by at least two consecutive transition belonging to the same rotational band, corresponding to E2 decay probability of more than 71% of the full rotational E2 strength. The symbols refer to the yrast line for each

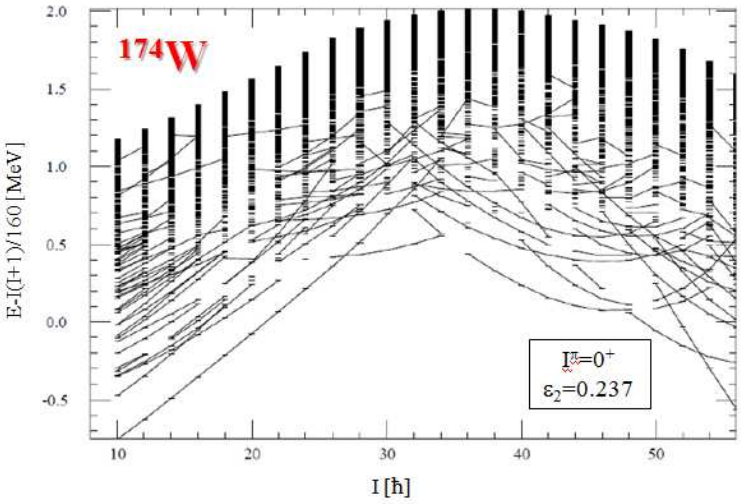

Figure 2.9: The calculated energy levels in ^{174}W for the (0^+) configuration. A reference rotational energy $I(I+1)/160\ MeV$ is subtracted. The solid lines connecting energy levels indicate stretched E2 transitions exhausting more than 71% of the full rotational E2 strength.

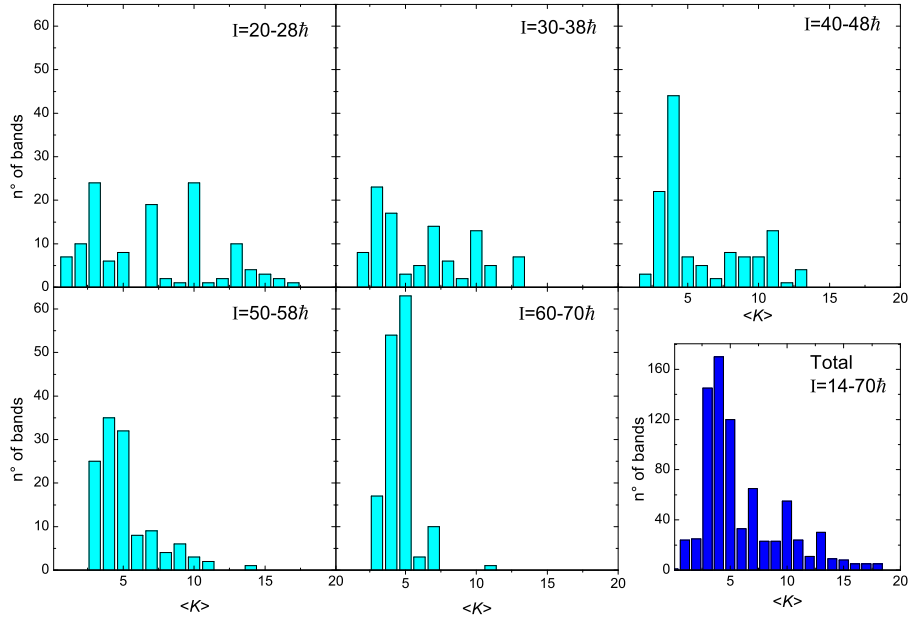

Figure 2.10: Average value of K for each rotational band composed by al least two consecutive transitions exhausting more than 71% of the full rotational E2 strength for different spin ranges (cyan plots) and for the whole spin interval (blue plot).

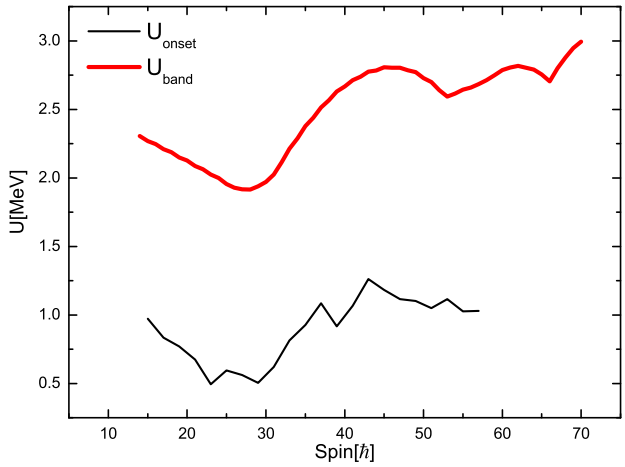

Figure 2.11: Black line: excitation energy value as a function of spin above which the E2 decay probability is fragmented ($n_b > 2$). Red line: energy limit for the microscopic CSM calculations.

spin-parity configuration.

Through CSM calculations it is possible to evaluate the number of rotational bands as a function of spin. This method does not give information about the population intensity of bands but provides only the number of microscopic paths available for the nuclear de-excitation. Fig. 2.13 shows calculations for low ($K < 6$) and high-K ($K \geq 6$) bands having different length (i.e. $N_{steps} = 1$, 2, 3, 4 and 5), as a function of spin.

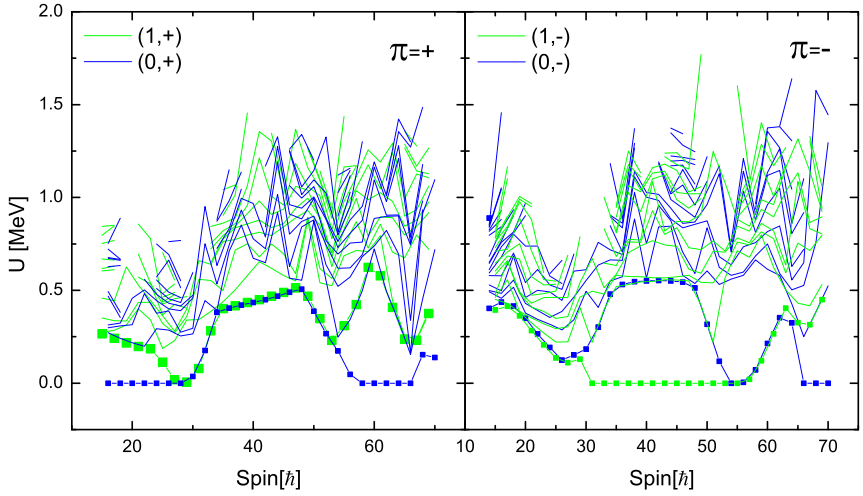

Figure 2.12: Excitation energy spectra calculated for low-lying discrete bands of ^{174}W: positive (negative) parity configuration are shown on the left (right). Symbols refer to yrast line for each spin-parity configuration.

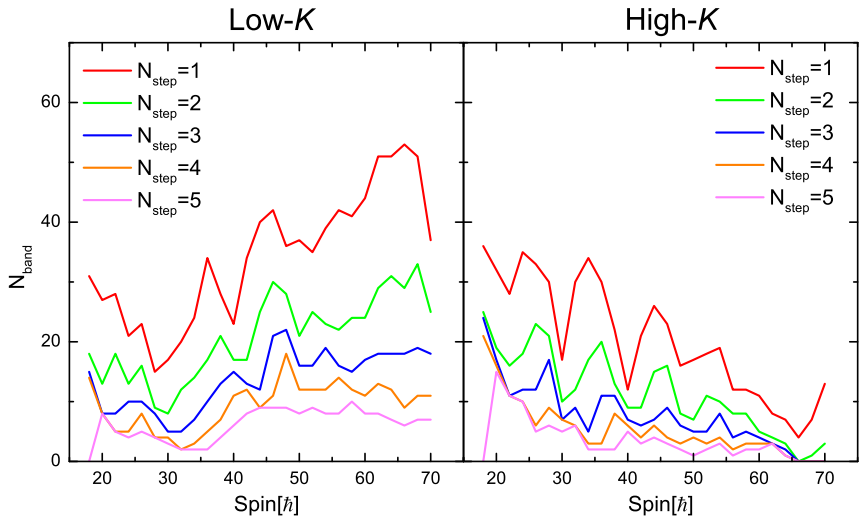

Figure 2.13: Calculated number of bands of ^{174}W using the CSM as a function of spin. Low-K (left) and high-K (right) bands with length N_{steps} = 1, 2, 3, 4 and 5 are shown.

Chapter 3

The experimental set-up

The experiment described in this thesis was performed in July 2010, at the Legnaro National Laboratories (LNL), in Italy.
The warm rotating ^{174}W nucleus has been populated by a fusion-evaporation reaction using a beam of ^{50}Ti at 217 MeV, impinging on a ^{128}Te target (1 mg/cm^2 thick backed by 50 mg/cm^2 of ^{nat}Pb). The beam was provided by the Tandem accelerator, with a typical current of 1 pnA.
The total fusion cross Section was calculated to be ~ 560 mb, leading to the compound nucleus ^{178}W. The evaporation residues were mainly ^{173}W and ^{174}W, which were produced with an excitation energy of ~ 4 MeV over the yrast line, reaching spins up to $60\hbar$, therefore providing a good population of the warm rotational regime. Details about the reaction will be given in chapter 6.
The γ-rays produced during their de-excitation have been measured using an array of HPGe segmented detectors (the AGATA Demonstrator) coupled to 27 BaF_2 scintillators, (the HELENA array) used for multiplicity and Sum Energy information. No Doppler correction was needed, owing to the use of a backed target.
A picture of the complete experimental set-up is shown in Fig. 3.1; the AGATA Demonstrator detectors are in the middle, while the coloured hexagonal clusters around them are the BaF_2 scintillators of the HELENA array.

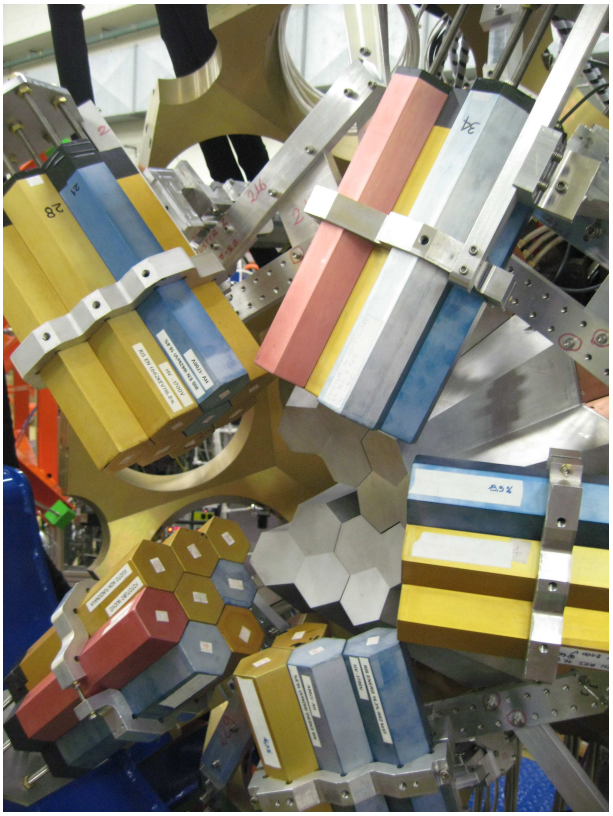

Figure 3.1: Picture of the experimental setup, comprising four triple clusters of AGATA (in the back of the picture) and an array of 27 BaF_2 detectors named HELENA, grouped in 5 clusters (two clusters of eight detectors, two of four detectors and one of three detectors).

3.1 The AGATA Demonstrator

AGATA (Advanced Gamma Tracking Array) is a European project aiming at the development and construction of a 4π array for nuclear spectroscopy studies. This kind of detectors is based on gamma-ray tracking, whose principle is the reconstruction of the sequence of interactions of each gamma-ray inside the array, in order to achieve a good suppression of the Compton background. As a consequence high efficiency is achieved, overcoming the limits of Compton-suppressed HPGe arrays. In the actual phase AGATA is composed by 5 triple-cluster of HPGe segmented detector, whose name is AGATA Demonstrator. The Demonstrator has started its campaign in 2009, when test experiments were done in order to evaluate the performances of the tracking algorithms in terms of energy resolution, efficiency and Peak-to-Total (P/T) ratio. The physical campaign, instead, has begun in February 2010, when the first in-beam measurement took place; at that moment only 3 triple-clusters were available. At the time of our experiment one triple-cluster was added to the existing set-up, resulting in 4 triple-clusters for a total of 12 HPGe detectors.

3.1.1 AGATA: Advanced GAmma Tracking Array

The aim of the Advanced GAmma Tracking Array (AGATA) project [7] is the construction of an array based on the novel concepts of pulse shape analysis and gamma-ray tracking with highly segmented Ge semiconductor detectors.
The best geometrical design has been deeply investigates, as described in [33]; here only the main ideas are summarized.
The first need was to have the best detection efficiency and solid angle coverage; an additional requirement in the conceptual design of AGATA was to keep a sufficiently large inner space inside the array in order to host ancillary instrumentation, which often is indispensable in the physics programme of AGATA. GEANT4 simulations were used to decide the best performing configuration based on geodesic tiling of a sphere with 12 regular pentagons and 180 hexagons. Owing to the symmetries of this specific buckyball construction, three slightly different irregular hexagons are needed (see Fig. 3.2); the three shapes are indicated by the colours red, green, and blue. The detectors are grouped in 60 identical triple-clusters, each containing a red, a green, and a blue crystal (see Fig. 3.3); the pentagonal

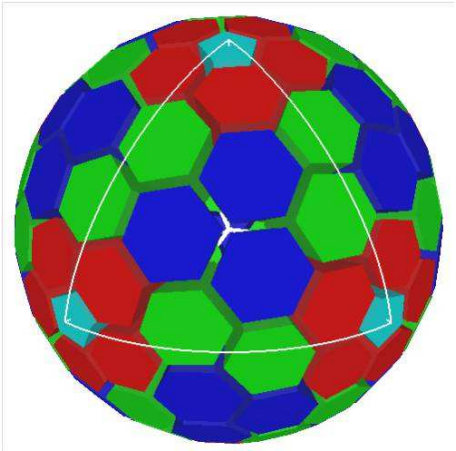

Figure 3.2: Schematic view of the full AGATA detector; the different colours represent the different shapes of the detectors [7].

detectors are individually canned. The three detectors are placed inside a single cryostat and are cooled to 90 K with a liquid nitrogen system. The preamplifiers for all segments and core signals are also cooled to 130 K.

The inner radius of the array is 23.5 cm. The total solid angle covered by HPGe material is close to 80% and the photo peak efficiency is as high as 50% for individual 1 MeV gamma rays. A key feature of AGATA is the capability to determine the emission direction of the detected gamma-rays with a precision of $\sim 1^{\circ}$. This corresponds to an effective solid angle granularity of $5{\cdot}10^4$ (unachievable with individual germanium crystals) and ensures an energy resolution better than 0.5% for transitions emitted by nuclei recoiling at velocities as high as 50% of the speed of light. This value is only a factor of two bigger than the intrinsic resolution of HPGe detectors and is comparable with the values currently observed at 10 times smaller recoil velocity.

3.1.2 High-fold segmented detectors

In order to achieve a large tracking efficiency (see Section 3.1.5), the positions where the gamma rays interact inside the detector volume should be determined with an accuracy of $\sim$ 5 mm at an energy of 1 MeV. This corresponds to an effective granularity of approximately 30000 voxels (the analogous of pixel in 3D) per Ge

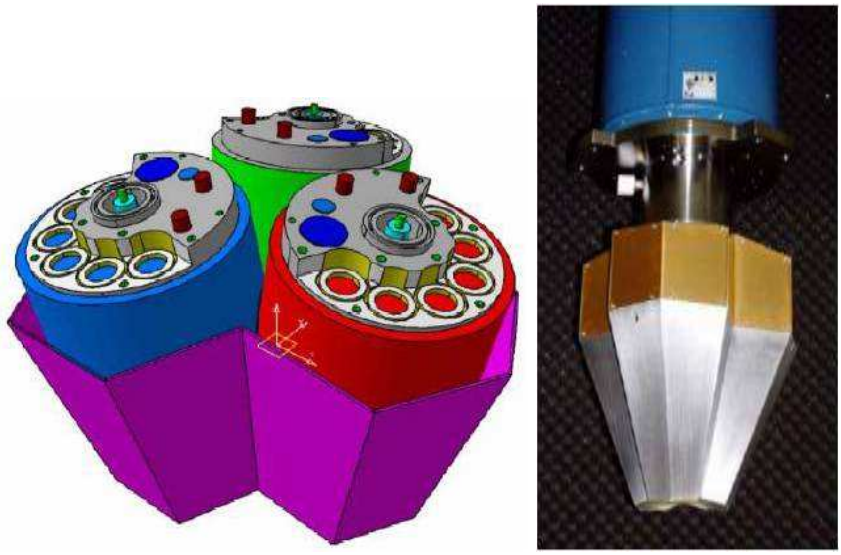

Figure 3.3: The AGATA triple-cluster: Technical drawing on the left and picture of a real cluster on the right

detector. While it is impossible to achieve such a granularity by a physical segmentation of the crystal, pulse-shape analysis methods (PSA) (see Section 3.1.4) can provide this position accuracy; a medium level segmentation of the outer detector contact is however required: each detector is then divided into 20 - 40 segments. The AGATA array is composed by large volume 36-fold segmented n-type germanium detectors in the semi-coaxial geometry, like the one depicted in Fig. 3.4. The detectors are produced by the French company Camberra and have a length of 90 mm, a diameter of 80 mm at the rear, and a tapering to a irregular hexagonal shape with an angle of 10° at the front. The sector-wise segmentation goes through the middle of each hexagonal side, the longitudinal segmentation forms rings of varying thickness, optimised for a uniform distribution of the gamma-ray interactions. Because of their complexity and the need of packing them very close to each other, these detectors use the encapsulation technology developed for the clusters of EUROBALL.

Figure 3.4: Schematic view of the 36-fold segmented, hexaconically tapered germanium crystal, as planned for AGATA.

3.1.3 Digital electronics

The use of Pulse Shape Analysis (PSA) techniques obviously requires that the shape of each pulse in the detector is recorded and processed digitally. For this reason, all 37 signals (36 segments + the central electrode) from each detector are digitised at 100 MHz immediately after the preamplifiers by high-resolution (14 bits) fast ADCs. Using the digitized signals the energy, time and position of each gamma ray interaction are then extracted using digital processing techniques. These data are associated with unique time-stamp and unique positional label which will be used by the data acquisition processors to associate data produced by the same event. Digital processing allows to use filters that have no analogue counterpart such as the Moving Window Deconvolution algorithm [34] to reconstruct the original charge collection by removing the effect of the preamplifier response. A good energy resolution can be achieved with shorter shaping time; in this way the array is able to sustain a counting rate per detector 5 times higher than the "traditional" apparatuses (50 kHz per detector instead of 10 kHz).

3.1.4 Pulse Shape Analysis

The task of Pulse Shape Analysis (PSA) is to identify with high precision the location of the individual interaction points and the corresponding energy deposits of a γ ray. There can be more than one interaction in one detector segment and/or the γ ray can be scattered to another segment of the same crystal or to an adjacent

detector or even across the array. Simulations show that in order to reach a satisfactory efficiency, tracking algorithms have to be provided with information on the gamma interaction localization with a precision of at least 5 mm.

The parameters of interest (i.e. three dimensional interaction position, energy, time and a confidence in the quality of the determined fit) are determined by comparing the detector pulse shapes to a calculated reference basis, where each signal corresponds to a well-localised single interaction point.

The input data for the PSA process for an AGATA detector consist in 37 signals $S_j(E,t)$, with $j = 0, 1, ..., 36$, sampled at the output of the HPGe detector preamplifiers (36 segments + core). Since the detector response is linear, $S_j(E,t)$ can be written as the superposition of the signals associated to the single hits of the gamma $S_j(x_i, y_i, z_i, t)$ weighted by their energy release E_i:

$$S_j(E,t) = \sum_{i=1}^{N} E_i S_j(x_i, y_i, z_i, t) \tag{3.1}$$

where N is the number of interactions inside the segment and $E = \sum_{i=1}^{N} E_i$.
In the case where $N = 1$, Eq. 3.1 reduces to

$$S_j(E,t) = E S_j(x_i, y_i, z_i, t) \tag{3.2}$$

Solving this equation means finding the interaction point that better reproduces the measured signal shape, by a comparison between the measured signal shape and the set of shapes belonging to the signal basis. In order to achieve a good position resolution, it is not sufficient to compare the net-charge signal of a segment with the basis, but the transient shapes in the neighbouring segments must also be compared to a basis for transient signals. If $N>1$, there is the added complication of disentangling the single interactions of each segment, all with an unknown energy deposit and unknown position.

The comparison of waveforms is a very challenging task if performed in a naive way, more so if a decomposition of each signal shape in multiple interaction points is needed, because it requires a large quantity of memory and of CPU time; fast and efficient PSA algorithms are therefore needed. Many approaches to the "PSA problem" have been proposed: adaptive grid search [35], neural networks, matrix inversion [36], genetic algorithms [37], recursive subtraction [38], etc.

In the experiment presented in this thesis, as in the whole LNL experimental campaign, it has been decided to use a grid search algorithm because it is the only

one with processing times small enough to be used in on-line acquisition. A basic assumption for this algorithm is that the size of a segment is small enough that multiple interactions inside the same segments can be neglected, so that the PSA is performed under the simpler case of Eq. 3.2, i.e. $N = 1$. While it is known that it is not a very realistic approximation, the effect on the overall performance of the detector has been found negligible [35].

Independently of the chosen algorithm, the quality of the PSA also depends critically on the signal basis that is used for the decomposition of the measured shapes. There is a large effort in the AGATA community to build an experimental signal basis [39, 40], but it is not yet available due to the long times needed to build up the necessary statistics while achieving a good precision on the reference positions. The basis used at the moment is obtained via detailed calculations of the charge transport through the detector [41], [42].

The reconstruction of the signal shape performed by PSA algorithms can also be used to increase the time resolution of a HPGe detector, compared with that obtained with a common approach based on a constant fraction discriminator. While such possibilities are under study [43], they were not employed for the present analysis.

Once the interaction points, with the corresponding energy and time, have been determined, the events have to be reassembled according to their timestamps and a tracking algorithm (see Section 3.1.5) is applied in order to disentangle the coincident interaction points and to determine the total energy and the emission direction of those γ rays that have been fully absorbed in the germanium array. Absolute positions of the individual crystals and target position corrections enter at this stage.

3.1.5 Gamma-ray tracking

The aim of tracking algorithms is to reconstruct the trajectories of the incident photons in order to determine their energy and direction. To do this, the algorithms must disentangle the interaction points identified in the detectors and establish the proper sequences of interaction points. Tracking algorithms can be divided into two classes: algorithms based on back tracking [44] and algorithms based on clustering and forward tracking [45]. Both are related to the particular properties of the

interaction of photons with matter.

Back tracking The back tracking algorithm [44] is based on the fact that the photoelectric energy deposition is almost independent from the incident photon energy and is peaked around $100 - 250\ keV$; it assumes that the interaction points within a given deposited energy interval $e_{min} \leq e_i \leq e_{max}$ are the last interaction (in time) of a fully absorbed gamma-ray; the algorithm then finds the closest interaction to the photoelectric one, it computes the scattering angle using the incident and the scattered energies and, finally, it searches for the other previous interactions along this direction; such process is iterated until the direction points directly to the target. This algorithm, however, was found to be less efficient and showed a worse P/T in the reconstructed spectra [46], and was therefore not used for our analysis.

Forward tracking In the forward tracking algorithm the first step is the identification of clusters of interaction points that may belong to a single gamma-ray. Looking at the forward peaking of Compton scattering cross-section, clusters are identified as a set of interaction points with an angular distance $\leq \theta_0$ between each other (link algorithm) or with respect to a given point (leader algorithm).
Secondly, each cluster is evaluated to determine whether it contains all the interaction points belonging to a single gamma-ray with the following criteria:

1. If the interaction points satisfy the Compton scattering formula, the tracking algorithm uses the angle-energy relation of Compton scattering to determine the most likely scattering sequence from the position and energy of the interaction points:

$$\chi^2 = \sum_{j=1}^{N-1} W_j \left(\frac{E_{\gamma'} - E_{\gamma'}^{pos}}{E_\gamma} \right)_j^2 \tag{3.3}$$

   where E_γ is the sum of the deposits from 1 to $N-1$, and $E_{\gamma'}^{pos}$ is the energy of the scattered photons according to the Compton scattering formula. For a cluster of N interaction points, the $N!$ permutations are tested, and the cluster is defined as "good" if the χ^2 is below a predetermined threshold.

2. If the cluster is composed by a single interaction point and the energy satisfy photoelectric conditions, the algorithm checks the compatibility between γ-ray energy and interaction depth in the detector. If the compatibility is reached, a Monte Carlo-like approach is taken to decide if to consider the interaction point as an actual photoelectric event or if to discard it as an isolated Compton scattering event.

3. If there are two gamma-rays of energy equal to 511 keV and an interaction point in the middle with energy greater than 1022 keV, that is a pair production event, the three energies are summed and considered as a single gamma-ray.

The algorithm tries to recover some of the wrongly identified clusters. For example, one type of incorrectly identified cluster comes from a single gamma-ray being separated into two clusters. This gamma-ray can be correctly identified by tracking together all pairs of bad clusters. When the result gives a small χ^2, the gamma-ray is recovered by adding the two clusters. The clusters which do not satisfy any of the above criteria are rejected, thus improving the P/T (peak to total) ratio of the spectra without the need for Compton suppression shields. If a large solid angle is covered with segmented germanium detectors, the combination of PSA and gamma-ray tracking allows for a very high photopeak efficiency together with a good P/T ratio. An example of the interaction clustering is represented in Fig. 3.5, where a high-multiplicity event is considered: the coloured dots represent single interaction points of gamma-rays inside a 4π detector shell; the red circles correspond to clusters of interaction points identified by the tracking as belonging to a single gamma-ray, while the green squares correspond to clusters that are discarded.

The forward tracking algorithm is the basis for the Orsay Forward Tracking (OFT) code [46] and the Mars Gamma-ray Tracking (MGT) code [47], that are implemented in the Narval code for the experimental data; the last one is also used for GEANT4 simulations.

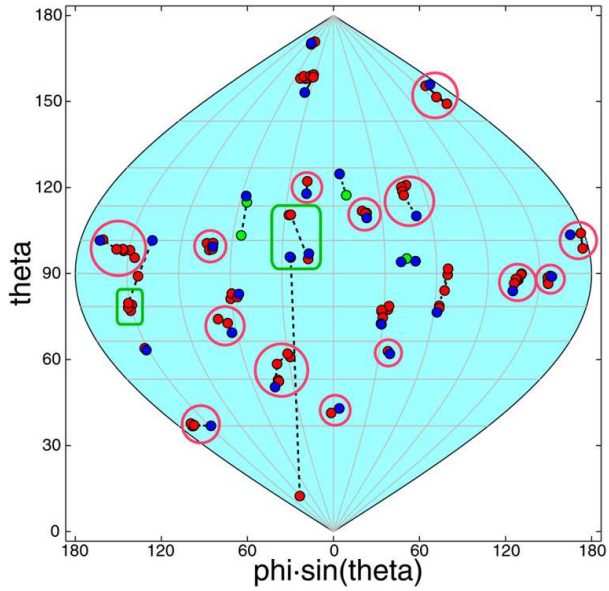

Figure 3.5: "World map" representation of $M_\gamma = 30$ events of $E_\gamma = 1.0\ MeV$ detected in an ideal 4π HPGe shell and reconstructed with the tracking algorithm. Correctly reconstructed transitions are grouped with red circles while green rectangles represent badly reconstructed background events.

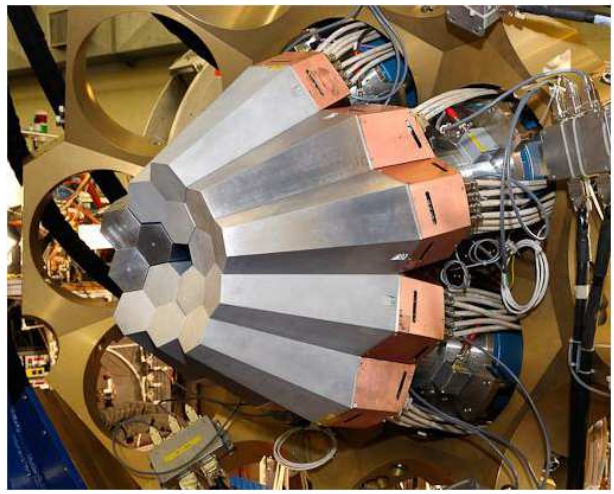

Figure 3.6: Photo of the AGATA Demonstrator installed at Legnaro National Laboratories.

3.1.6 The Demonstrator phase of AGATA

It has been planned by the international collaboration that the development of AGATA will proceed in stages, with the construction of the full array preceded by a R&D phase aimed at building a subsystem of 5 triple clusters, called AGATA Demonstrator array. The Demonstrator, together with its digital electronics, DAQ and full on line processing of the digitized data, has been installed in LNL in 2008 and has been used in various physics experiments from February 2010 to December 2011. The aim of the experimental campaign of the Demonstrator is to confirm the performances of the γ-ray tracking algorithms in real measurement conditions. A picture of the full Demonstrator is shown in Fig. 3.6. In a "conventional" array of germanium detectors, a collimator is placed in front of each detector in order to minimize the scattering of photons between different crystals. Therefore, only a small region around the target position is actually visible from the detectors. In the case of the AGATA Demonstrator array, no collimators are present, and thus it is possible to modify the placement of the detectors relative to the target position depending on the specific measurement. In particular, given the lack of spherical symmetry and the limited solid angle coverage, it is feasible to place the detectors closer to the target position compared to the "reference" 23.5 *cm* distance of the

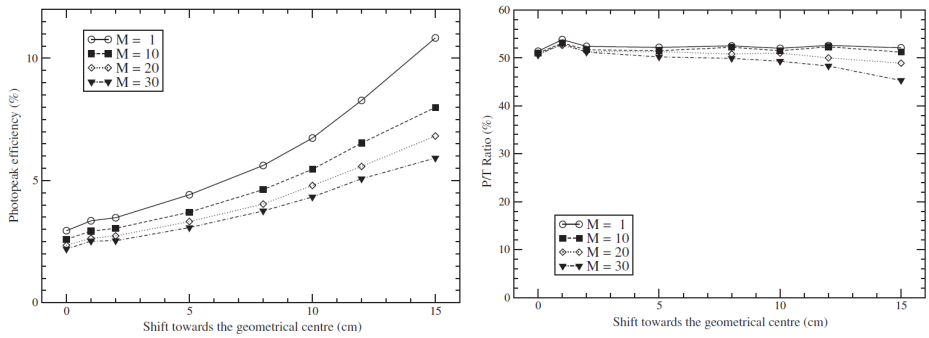

Figure 3.7: Photo-peak efficiency (left) and peak-to-total ratio (right) of the AGATA Demonstrator array for 1 MeV photons emitted from a point source at rest [33].

full AGATA array in order to cover a larger solid angle. The simulated photo-peak efficiency and P/T ratio as a function of the shift towards the geometrical centre are shown in Fig. 3.7 for monochromatic 1 MeV γ-rays.

3.1.7 Energy Resolution

The energy resolution is one of the main parameters describing the performances of an HPGe detector array. The energy resolution can be parametrised by the analytic function:

$$FWHM(E_\gamma) = \sqrt{F^2 + G^2 \cdot E_\gamma + H^2 \cdot E_\gamma^2} \tag{3.4}$$

The intrinsic energy resolution of the AGATA array is measured using standard γ-ray sources and it is then compared to in-beam data. The energy resolution is given by the FWHM of the γ peaks and changes as a function of the energy. In the present experiment the intrinsic energy resolution of the array has been evaluated using γ transitions from an ^{152}Eu source.
In Fig. 3.8 data obtained for the AGATA detectors from the ^{152}Eu source and from in-beam data are compared. The in-beam energy resolution is equivalent to the one obtained from the radioactive source, being the γ radiation emitted by excited nuclei fully stopped in the backing of the target. The two distributions were fitted using the function in Eq. 3.4; the obtained parameters are reported in Tab. 3.1.

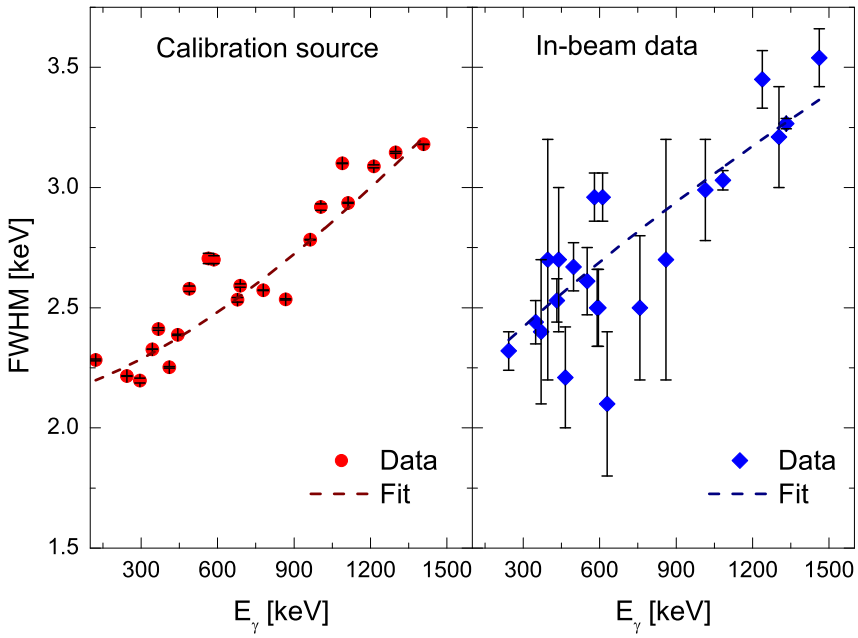

Figure 3.8: Energy resolution for the ^{152}Eu calibration source (red circles) and for in-beam data (blue diamonds) from the reaction ^{50}Ti + ^{128}Te studied in this work, as a function of the γ-ray energy. The obtained resolutions are comparable due to the use of a backed target.

Parameter	Calib. Source	In-beam data
F	2.15	2.12
G	1.21	2.12
H	1.34	0.34

Table 3.1: Fitting parameters of Eq. 3.4 for the energy resolution data plotted in Fig. 3.8.

Parameter	A	B	C	D	E	F	G
Value	6.7	-0.1	0.0	6.0	-0.5	0.1	15.0

Table 3.2: Efficiency fitting parameters of Eq. 3.5 for the distributions plotted in Fig. 3.8.

3.1.8 Efficiency

The other most important property of a multi-detector array is the detection efficiency, which corresponds to the total photo-peak absorption probability over the 4π solid angle. The detection efficiency depends on the energy of the γ-ray detected.
The relative intensity of γ-ray detection for the AGATA array is obtained using standard ^{152}Eu source.
The main idea at the basis of the evaluation of the efficiency curve is to compare the measured intensities of the main transitions visible in the spectra of the radioactive source, with the tabulated values given in literature. The points that are obtained from this comparison are then interpolated with the following analytical function, which well reproduces the efficiency curve of a Ge detector:

$$\epsilon = exp((A + Bx + Cx^2)^{-G} + (D + Ey + Fy^2)^{-G})^{-1/G} \tag{3.5}$$

being $x = log(E_\gamma/E_1)$ and $y = log(E_\gamma/E_2)$, where $E_1 = 100\,keV$ and $E_2 = 1\,MeV$. The function is divided into two terms, the first acting on the low energy part of the spectrum and the second on the high energy transitions. The parameter C is usually set to 0. The seventh parameter G is the connecting point between the two parts.

Using the ^{152}Eu source, we have a sufficient number of points to cover the energy interval up to 1.5 MeV. The efficiency was calculate using the programs Source and Effit of the Radware package [48].
The efficiency curve of the AGATA array is shown in Fig. 3.9, while the coefficients derived from the fit are reported in Tab. 3.2.

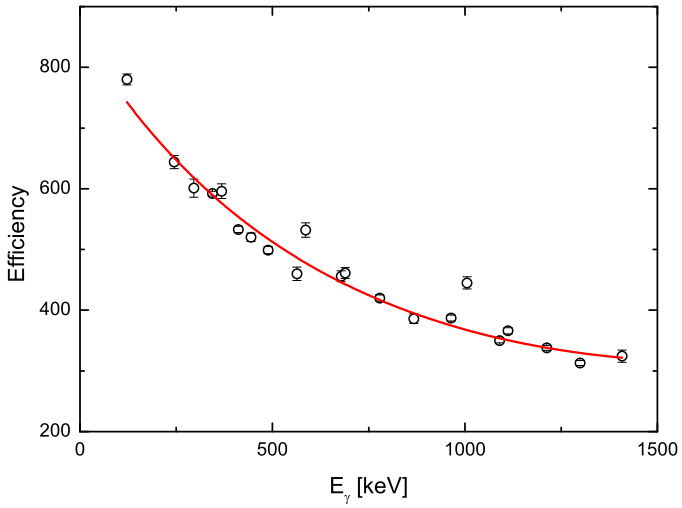

Figure 3.9: Efficiency curve of the AGATA array obtained from a standard ^{152}Eu source. The red line is the result of a least-squares fit by Eq. 3.5 using the program *EFFIT*.

3.2 The HELENA array

In the experiment described in this thesis, 27 BaF_2 detectors (named HELENA), originally used in the HELENA multiplicity filter array [49], were placed around the AGATA Demonstrator array: that is the maximum possible number of detectors that can be inserted between the AGATA flanges and the PRISMA magnetic spectrometer first quadrupole. Each detector is 2.5 *inch* $\times$ 3 *inch* large; they were grouped into five clusters: two clusters composed of 8 detectors, two clusters formed by 4 detectors and the last one composed of 3 detectors (see Fig. 3.10). An optimum distance of 15 *cm* from the target has been chosen for the HELENA detectors, through GEANT4 simulation [50]. These calculations show that the total solid angle covered by the HELENA array is $\sim$25% of 4π and the absolute efficiency is $\sim$20%. The configuration simulated with GEANT4 is shown in Fig. 3.11.

During the experiment the signal of each HELENA crystal was sent to a channel of a BaFpro module [51]. BaFpro is a custom spectroscopy amplifier developed in Milan for the shaping of BaF_2 signals; it has 16 channels and for each of them it

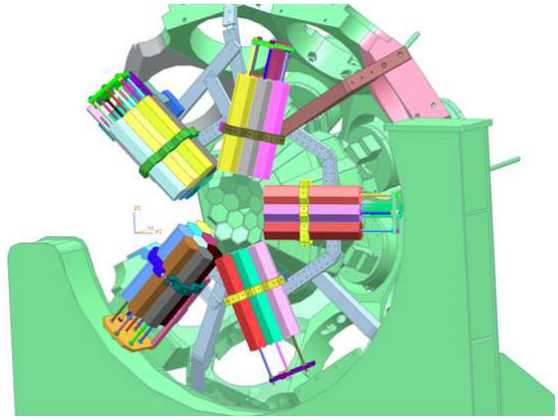

Figure 3.10: Schematic view of the HELENA array, grouped in 5 clusters: two clusters with 8 detectors, two clusters with 4 detectors and one with 3 detectors

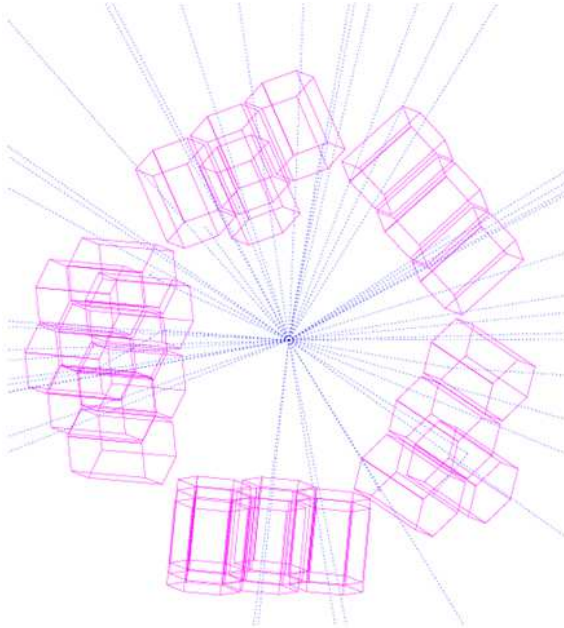

Figure 3.11: The configuration that has been simulated with GEANT4 [50] for the HELENA array used in AGATA.

gives a "fast" and a "slow" output, corresponding to the fast and slow components of the signal (see Section 3.2), as well as a "time" output obtained by a Constant Fraction Discriminator (CFD).

Barium Fluoride (BaF_2) is one of the most used scintillation detectors in nuclear physics, due to its excellent time resolution ($\sim 350 - 600\ ps$) and good efficiency (due to the high density of Barium Fluoride, that is 4.88 g/cm^3 and high atomic number); it is characterized also by a fairly good energy resolution (about 9% at 1 MeV). The light signal of these detectors consists of two components: a fast component with decay time of 0.5 ns and a slower component with 600 ns decay time. These two different components allow obtaining from the same signal a good time resolution (using the fast one) and an acceptable energy resolution (by integrating the fast and slow components). Since the ratio of fast and slow component changes with the incoming particle, they are commonly combined to make light particles discrimination, through fast vs. slow matrices.

3.3 The Data Acquisition System

As mentioned in Sec. 3.1.2, the electrical contacts of each AGATA detector are divided into 36 segments and the digitizers sample the pulses from each segment at 14 bits precision with a frequency of 100 MHz; for every accepted event, a pulse trace of 60 samples is extracted and acquired. With a counting rate of 50 kHz/crystal the data-flow for each detector is therefore of the order of 100 MB/s (with zero suppression). Furthermore, in order to have an online analysis, the PSA has to be performed in real time for each of the acquired traces and tracking algorithms must reconstruct the detected gamma-rays from the PSA information. This means that the Data Acquisition (DAQ) software for AGATA has to be able to handle large quantities of data, control a computing farm for the PSA and tracking algorithms, and coordinate the flow of information between the digitizers, the computing farm, and the disk server where all the data are written. All of this is performed by a NARVAL-based DAQ software [52].
The HELENA ancillary detectors were controlled by an independent DAQ running on a KMAX environment [53], which communicated with the VME crate via an optical fibres and with NARVAL via TCP/IP.

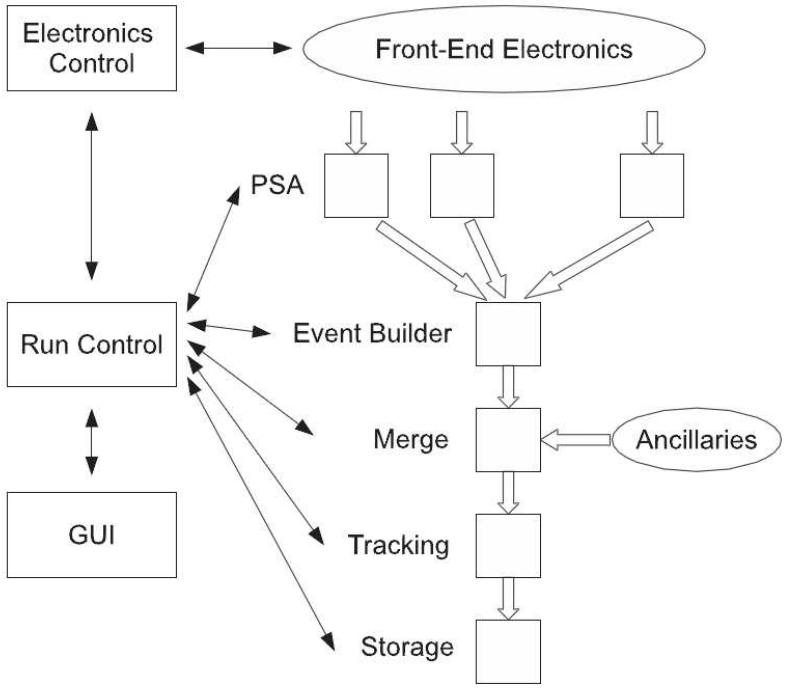

Figure 3.12: Layout of the AGATA acquisition system [7].

NARVAL is based on actors corresponding to separate processes that receive and send out data at any stage of the data-flow chain; actors communicate with each other with a UNIX fifo if running on the same machine or with a TCP/IP socket if running on different machines. There are 3 types of actors:

- producer: they interface with the hardware and read out the data;
- intermediary: they perform operation on the data, receiving input and sending output from/to one or more other actors;
- consumer: they can only receive input from the other actors and store the data to disk or act as histogrammers.

From the point of view of NARVAL, each AGATA detector is considered as a separate entity and the whole array may be considered as the aggregation of synchronized data supplied by the individual crystals. The synchronization is guaranteed

by the AGATA Global Trigger and Synchronization (GTS) hardware with a common 100 MHz digital clock.
For each AGATA detector there is a producer actor reading the pulse traces from the front-end electronics; the traces are sent (together with the timestamp information) to an intermediary actor that performs the PSA and to a consumer that writes them to disk; the PSA data from all detectors are sent to an intermediary actor that acts as event builder, matching the data from different detectors through the timestamp information. For the ancillary detectors, there is a producer actor that receives the data from the KMAX acquisition, kept synchronized to the GTS via the AGAVA (AGATA Ancillary VME Adapter) module. The producer sends the VME data to a consumer that writes them to disk and to an intermediary that decodes the VME words and sends only the actual data words to the event builder, discarding VME header and trailer words. The builder then matches the ancillary data to the AGATA data and sends the event to another intermediary that performs the online tracking. A schematic representation of the Data Acquisition System is given in Fig. 3.12.

3.4 Trigger conditions

When a γ-ray is detected in an AGATA crystal, a trigger request is formed and sent via the GTS to the trigger processor, which can validate the request (meaning that all the information about the event are acquired, written and processed) or reject it. This software trigger can be used to make multiplicity requirements on the AGATA crystals, or to make a coincidence between AGATA and the ancillary detectors via the AGAVA module.

This way to proceed was not suitable for this experiment, because a more complex trigger was needed. Therefore, a standard NIM elctronics was used to build the master gate trigger and to send it via AGAVA as a trigger request to the DAQ system. The initial master gate was the coincidence between at least 2 events in AGATA ($M_\gamma \geq 2$) and HELENA. The AGATA trigger was made using the analogue output of each AGATA detector (present for debug purposes), sent to standard CFD modules, to a logical "OR" and to a multiplicity module; the HELENA scintillators trigger was the logic "OR" of all the 27 BaF_2 detectors, taken from the CFD output of BaFpro. This is the hardware part of the trigger

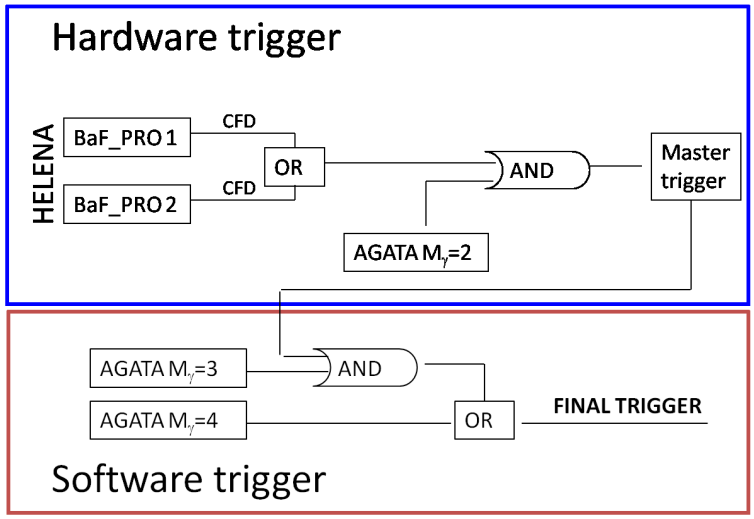

Figure 3.13: Schematic view of the trigger conditions used during the experiment. The hardware and software components are put in evidence.

conditions.

However, during the first runs of the experiment, the counting rates were too high and generate instability in the DAQ system. In order to reduce the counting rates, other more restrictive software condition were added to the hardware ones. In particular, a three-fold event request in AGATA was combined to the previous hardware trigger and a four-fold condition for the AGATA events was added.

The resulting trigger is schematically described in Fig. 3.13. It is the logic "OR" of two conditions:

1. three-fold events in AGATA in coincidence with at least one event in HELENA (hardware + software)

2. four-fold events in AGATA (completely software)

It has been observed that with this kind of trigger conditions, a better selection of the events of physical interest can be achieved together with acceptable counting-rates. Typical values of the counting rates are listed in Tab. 3.3.

AGATA singles	HELENA singles	AGATA $M_\gamma = 2$	Acquired events
15 kHz	45 kHz	5.4 kHz	3.5 kHz

Table 3.3: Typical counting rates of the experiment. Singles AGATA (HELENA) are events of multiplicity $M_\gamma > 1$ in the AGATA (HELENA) array; AGATA $M_\gamma = 2$ are events of multiplicity 2; acquired events means the rates of triggered events.

Chapter 4

Preliminary data-analysis

The first part of the data analysis has been focused on the presorting of the raw data. In fact, in order to obtain better performances of the Pulse Shape Analysis (PSA) and tracking algorithm, the so-called "replay" of the data is needed. This means that the same procedure of performing PSA and gamma-ray tracking on-line, i.e. during the experiment, has to be done off-line, starting from the pulse shape of the HPGe AGATA detectors written to disk.
After that the nuclear configurations interesting for the analysis are selected using the procedure described in Sec. 4.3 and 4.4.

4.1 Replay of the Data

As described in Sec. 3.1 the performances (i.e. energy resolution, efficiency and P/T ratio) of the AGATA Demonstrator depend on the performances of the PSA and tracking algorithms. During the experiment these operations are done in real time by the NARVAL Data AcQuisition (DAQ) system (see also Sec. 3.3), but they can also be performed after the experiment with a C++ emulator of NARVAL.
This is possible because the DAQ writes to disk a list-mode file for each detector, containing the digitized pulse signals from the segments and the timestamp information for each event; the emulator can process all these files, running again the PSA and γ-ray tracking and matching the AGATA and ancillary data. This procedure is called "replay", because from the point of view of the data processing

it is essentially a repetition of the experiment.

In the case of tha present experiment, the replay was necessary in order to apply a better calibration to the AGATA detectors segments (see Sec. 4.1.1), since the calibration used on-line was not very accurate being based on a short run at the beginning of the data taking. We could also make use of improvements in the PSA that were not available at the time of the experiment, such as the correction for neutron damage (see Ref. [7] and references therein).

The replay was performed in two steps:

1. The energy calibration was applied and the PSA was performed for all AGATA detectors. The original data, including the pulse shapes of each HPGe detector were "reduced" to only energy, position and time information; for all the events they were saved to disk.

2. The data from all the segments were merged and the tracking was performed. The ancillary detectors were calibrated and data from the AGATA and HELENA arrays were combined for each event.

The advantage of this separation in two steps is that the PSA is a very long process, requiring a large amount of computing power and memory: in the present experiment about one week was needed to perform the first step with 10 computers working in parallel. The tracking, instead, is a much faster procedure and could be repeated several times as we changed parameters, without having to perform the PSA again.

After the replay is completed, the user is given a list-mode file in ROOT tree format. For each event, the file contains the list of reconstructed gammas, together with their energy, time information and the position of the first interaction, as well as the data of the ancillary detectors received from the VME crate.

4.1.1 AGATA energy calibration

The energy calibration of the AGATA detectors is performed during the first step of the replay, together with the PSA. The calibration coefficient for each segment of the 12 detectors and for the core electrode were calculated using calibration runs acquired with an $AmBe - Ni$ source. This source is composed by a core of ^{9}Be and alpha-unstable ^{241}Am and is surrounded by a thick layer of paraffin

and Polyvinyl chloride (commonly known as PVC); some Nichel discs are also placed inside the paraffin layer. When an alpha particle is emitted by the ^{241}Am, there is a high probability that it is captured by a ^{9}Be, making a $^{9}Be(\alpha,n)^{12}C$ reaction. The neutrons are emitted with energies between $\sim 400\,keV$ and $\sim 5\,MeV$ and are thermalized by the multiple scattering in the paraffin layer, which serves both as moderator and as shielding. The slow neutrons are then captured by the nickel isotopes, as well as by the chlorine isotopes present in the PVC material that was used as an additional shielding; the neutron capture by the ^{1}H nuclei of the shielding produces additional gamma-rays in the spectrum. Note that the $^{9}Be(\alpha,n)^{12}C$ reaction can also populate the ^{12}C in its first excited state, at 4.4 MeV; the gamma decay from the level is Doppler broadened because the ^{12}C has a v/c of $\sim$10%.
The γ rays used for the calibration are 17 for the core electrode and 7 for the segments; they are reported in Tab. 4.1 together with the corresponding reactions.

As one can see from Tab. 4.1, the AmBe-Ni source is very useful because the $^{58}Ni(n,\gamma)^{59}Ni$ reaction produces γ rays up to $\sim$9 MeV. This is one of the few ways to have such high-energy gamma rays without using an accelerator. The energy spectrum acquired with the AGATA Demonstrator for the AmBe-Ni source is shown in Fig. 4.1.

The front-end electronics for the AGATA detectors has two settings, one for low dynamic range (up to 4 MeV) and one for high dynamic range (up to 20 MeV). In the present experiment, the 20 MeV range was used, although it is known that the segments show a non-linearity at high energies with this setting. While this effect is not large enough to compromise the performance of the tracking algorithms, it can deteriorate the energy resolution of the reconstructed gamma-rays. Since this non-linearity affects only the segments, and not the core signals of the detectors, it is possible to correct this effect requiring in the tracking algorithm that, for every event, the sum of the segment energies in a crystal is recalibrated to be equal to the energy measured in the core. This procedure was also used to produce the spectrum in Fig. 4.1, which shows a FWHM of $\sim$7 keV at 8998.4 keV.

After this first calibration, the calibration coefficient were refined in order to check the gain stability over the time. This was done by choosing a set of reference lines and comparing the measured energy with the known value, for each crystal and each run. A new linear calibration was applied and the coefficient of the

Core		Segments	
Energy [keV]	reaction	Energy [keV]	reaction
1951.1	$^{35}Cl(n,\gamma)^{36}Cl$	595.8	$^{73}Ge(n,\gamma)^{74}Ge$
1959.3	$^{35}Cl(n,\gamma)^{36}Cl$	846.8	$^{56}Fe(n,n')^{56}Fe$
2223.2	$^{1}H(n,\gamma)^{2}H$	1332.5	^{60}Co
2863.8	$^{35}Cl(n,\gamma)^{36}Cl$	1460.8	nat. rad. ^{40}K
4400.0	$^{12}C(n,n)^{12}C$	2223.2	$^{1}H(n,\gamma)^{2}H$
3061.9	$^{35}Cl(n,\gamma)^{36}Cl$	5088.9	$^{35}Cl(n,\gamma)^{36}Cl$ d.e.[1]
4979.8	$^{35}Cl(n,\gamma)^{36}Cl$	5599.9	$^{35}Cl(n,\gamma)^{36}Cl$ s.e.[2]
5517.2	$^{35}Cl(n,\gamma)^{36}Cl$		
5715.3	$^{35}Cl(n,\gamma)^{36}Cl$		
6110.9	$^{35}Cl(n,\gamma)^{36}Cl$		
6619.6	$^{35}Cl(n,\gamma)^{36}Cl$		
6627.8	$^{35}Cl(n,\gamma)^{36}Cl$		
6977.9	$^{35}Cl(n,\gamma)^{36}Cl$		
7414.0	$^{35}Cl(n,\gamma)^{36}Cl$		
7790.3	$^{35}Cl(n,\gamma)^{36}Cl$		
8533.4	$^{58}Ni(n,\gamma)^{59}Ni$		([1]Double escape peak)
8998.4	$^{58}Ni(n,\gamma)^{59}Ni$		([2]Single escape peak)

Table 4.1: The γ rays generated by the AmBe-Ni source used for the AGATA HPGe detectors calibration (core on the left and segments on the right).

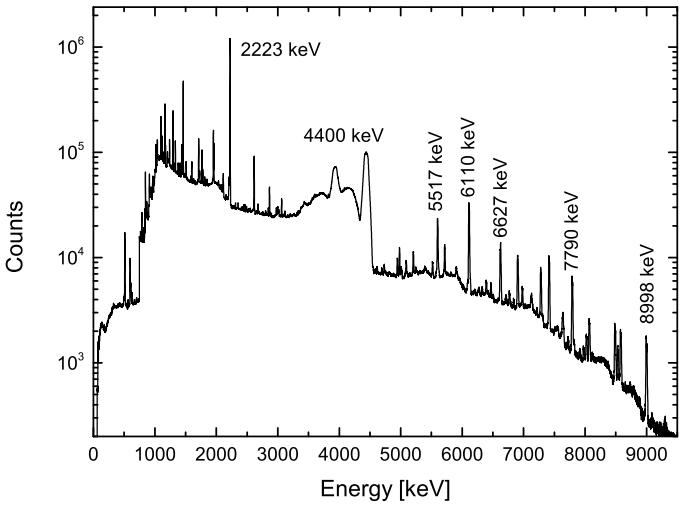

Figure 4.1: Energy spectrum from a composite AmBe-Ni source measured with the AGATA Demonstrator. The broad structure around 4 MeV is the Doppler-broadened decay of the first excited state of ^{12}C. The spectrum has been obtained after recalibrating segment energies with the energy measured by the core, for each crystal.

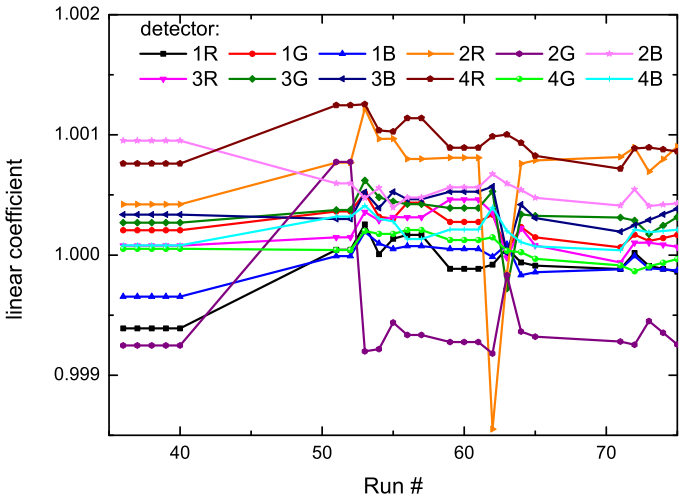

Figure 4.2: The coefficient of the linear term of the recalibration fit is plotted for each crystal and for each run. The gain fluctuations are within 0.3 %. We have chosen 14 reference line between 243.2 keV (^{174}W) and 1436.6 keV (background line from ^{208}Pb target backing)

linear term was plotted, as shown in Fig. 4.2. The gain variation over all the measurement, that lasted one week, is less than 0.3 % indicating that the AGATA detectors were very stable. These coefficients were then used to recalibrate all the detectors and correct these very small gain fluctuations.

4.1.2 HELENA energy calibration

The calibration of the BaF_2 detectors is performed during the second step of the replay, together with the tracking procedure, when the information given by the AGATA and HELENA arrays are merged. Since the BaFpro spectroscopy amplifier (see Sec. 3.2) had some instability before the start of the experiment, a calibration run was necessary at the end of the measurement. A ^{88}Y source was used; it provides 2 γ rays at 898 keV and 1836 keV. This source is very useful for calibrating BaF_2 detectors, because the two lines are very far from each other and can be very well distinguished even with poor energy resolution, as one can see in Fig. 4.3.

After applying the calibration coefficients, three BaF_2 detectors (detectors n. 1, 4 and 17) showed a different global shape of the spectrum, due to electronic

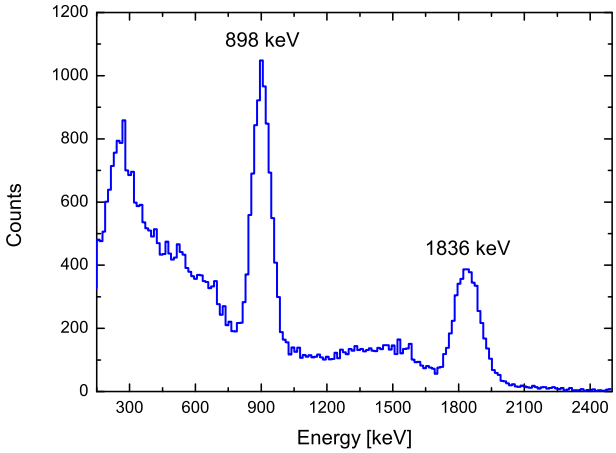

Figure 4.3: Energy spectrum of a ^{88}Y source, used to calibrate the HELENA BaF_2 detectors.

instability, in particular to the ADC modules. This effect was adjusted by adding correction factors in the sorting program, calculated in such a way to reproduce the global shape of the energy spectrum of "good" BaF_2 detectors. Fig. 4.4 shows the energy spectrum of one "good" BaF_2 detector taken as a reference (in red) and the corrected energy spectra of three BaF_2 detector affected by gain fluctuations (blue, green and black lines).

4.1.3 Time spectra

Each gamma-ray reconstructed by the tracking algorithm is associated to a timestamp T_{AGATA}, which measures the absolute time from the start of the Global Trigger and Synchronization (GTS) clock in steps of 10 ns. A more precise information is given by the PSA, that uses a Constant Fraction Discriminator (CFD) to determine the start time of the signal t_{CFD}. The sum of these two values gives the detection time of the gamma relative to the start time of the GTS, as reported in Eq. 4.1.

$$time_{TT} = T_{AGATA} + t_{CFD} \tag{4.1}$$

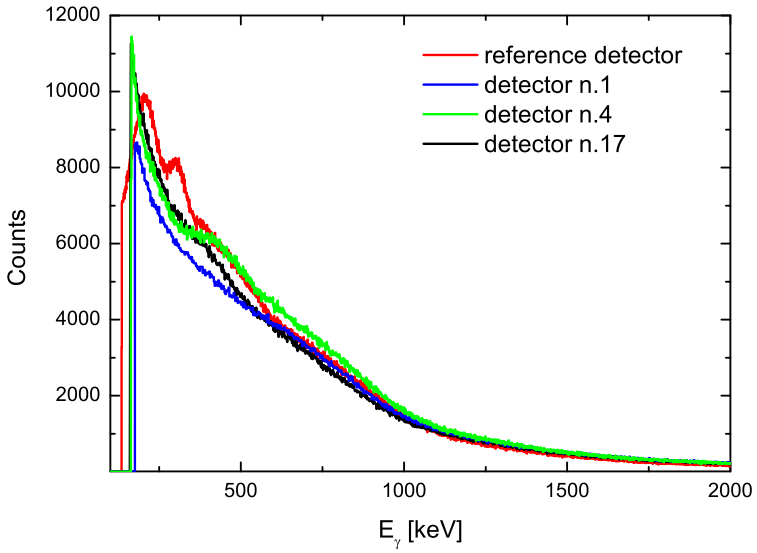

Figure 4.4: Energy spectra of three BaF_2 detector affected by gain fluctuations after the correction (blue, green and black lines). The reference BaF_2 detector energy spectrum is plotted in red.

Figure 4.5 shows the AGATA time spectra, obtained by choosing one of the 12 detectors as a reference and by measuring the time difference between that detector and the other. A time walk of $\sim 20ns$ was observed, as one can see in the left panel. This has been corrected by adding an offset term during the second step of the data replay (within the tracking algorithm). The resulting spectra, after the correction, are shown in the right panel: here the spectra are aligned in less than 5 ns, that is smaller than the time resolution of HPGe detectors (~ 10 ns).

In order to correlate the information given by the AGATA and HELENA arrays, time spectra between AGATA and the ancillary HELENA detectors have been built and aligned. This work, at the first stage, is done by the Narval emulator, that creates spectra obtained as the difference between each AGATA detector and the AGAVA (i.e. HELENA ancillary detectors) time stamp, in step of 10 ns. Figure 4.6 shows, on the left, these time difference $time_{TA}$ spectra, without any correction and, on the right, after they have been aligned. The correction is done by adding the factor with the keyword *TimestampCorrect* in the Narval emulator second step. The second step to build the AGATA vs HELENA time spectra is performed

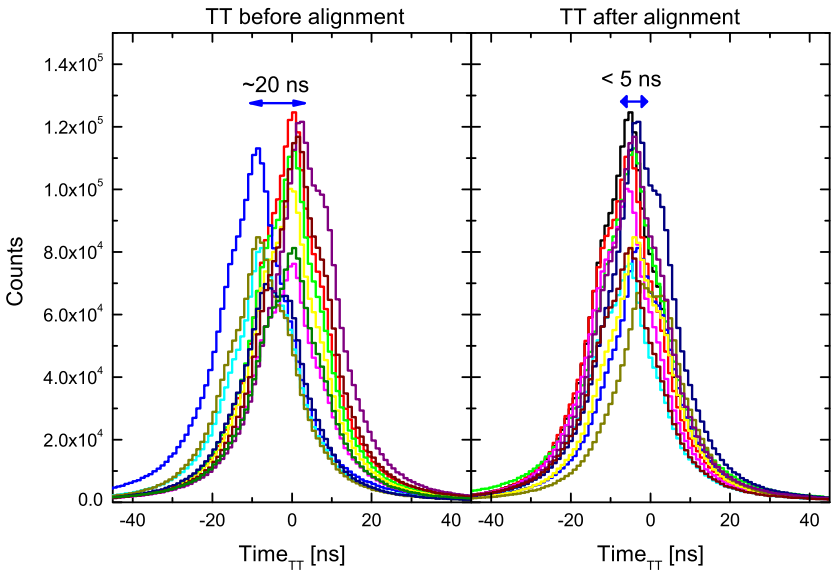

Figure 4.5: Time spectra of all AGATA detectors against a reference one, before (left panel) and after (right panel) the correction of the time walk.

within the sorting code. A better precision can be obtained either by adding to the AGAVA timestamp the so-called "phase shift" $t_{phase-shift}$ and by including the CFD information t_{CFD} to the AGATA timestamp. The AGAVA phase-shift is acquired by one channel of the TDCs and measures when the VME master gate was opened relative to the GTS clock, while the CFD information is extracted during the PSA, as mentioned before.

The AGATA vs HELENA time information is then defined as follows:

$$t_\gamma = T_{AGATA} + t_{CFD} - T_{AGAVA} - t_{phase-shift} \tag{4.2}$$

where T_{AGATA} and T_{AGAVA} are the timestamps for AGATA and for the ancillary detectors, as obtained by the Data Acquisition System.
The spectrum shown in Fig. 4.7 is obtained by calculating for each gamma-ray the time information as given by Eq. 4.2.

Another time spectrum useful for the analysis (see discussion in Sec. 4.4) is obtained from the time difference between the trigger of the acquisition and the HELENA detectors, here indicated as t_{HELENA}. This information is given by the TDC, because these modules work in “common start” mode, meaning that each

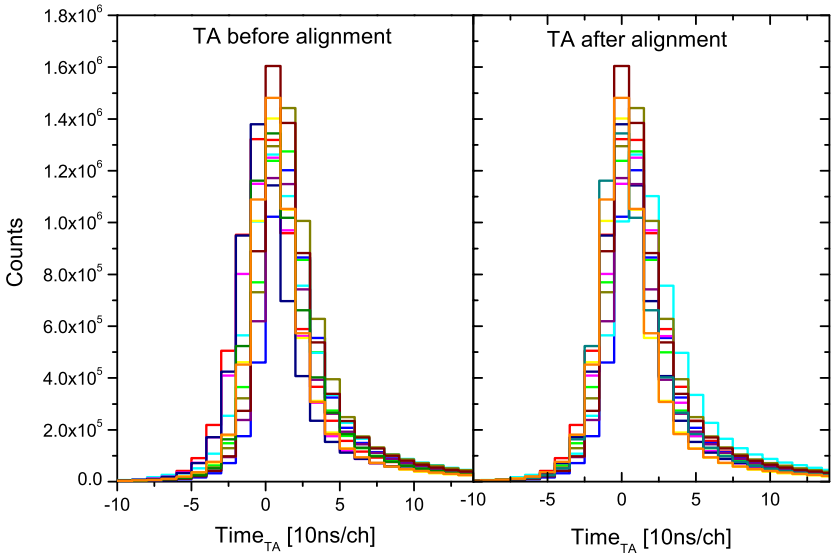

Figure 4.6: Time spectra obtained as the difference between each AGATA detector and the HELENA array time stamp $time_{TA} = T_{AGATA} + T_{AGAVA}$, with a step of 10 ns. The spectra before the alignment are shown on the left, while the corrected ones are plotted on the right.

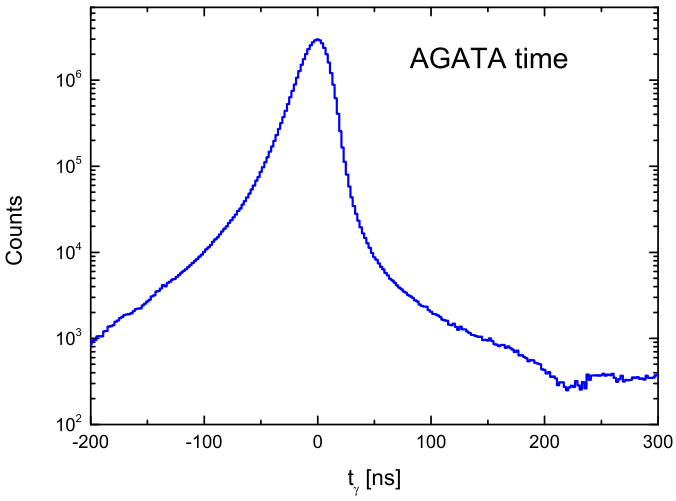

Figure 4.7: Example of time AGATA vs HELENA spectrum constructed following Eq. 4.2

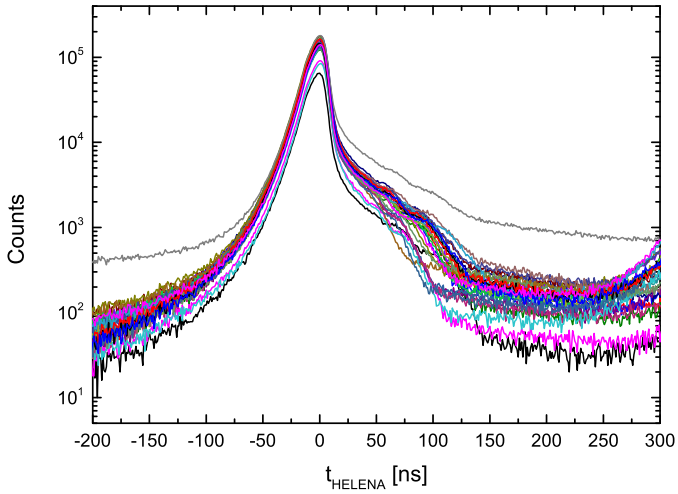

Figure 4.8: Time spectra of the 27 BaF_2 detectors, with respect to the master trigger signal.

TDC channel is started by the master trigger (see Sec. 3.4) and is stopped by the time signal of the corresponding BaF_2 detector. Fig. 4.8 shows the time spectra of all the 27 HELENA detectors. The narrow peak centred at $0ns$ corresponds to prompt coincidences, while the bump on the right contains delayed transitions; the latter is fundamental for the subsequent analysis, as explained in Sec. 4.4. On the left side of the prompt peak, background events are collected. The time spectrum described above is an alternative way to define AGATA vs HELENA γ time correlations since the trigger contains always a condition on the AGATA detectors (cfr. Sec. 3.4). Fig. 4.9 shows a comparison between the two classes of time spectra t_γ and t_{HELENA}: they present the same main structures, although the HELENA time spectrum constructed with respect to the master trigger presents a more pronounced distribution of delayed events. This happens because the T_{AGAVA} component of t_γ triggers on the first acquired event, so if BaF_2 ancillaries detect a prompt and a delayed gamma, only the first participates in the construction of the time spectrum; this means that some delayed events are "lost". On the contrary, t_{HELENA} is the sum of all time information given by the 27 HELENA detectors, therefore all the delayed events are acquired and increment the t_{HELENA} time spectrum.

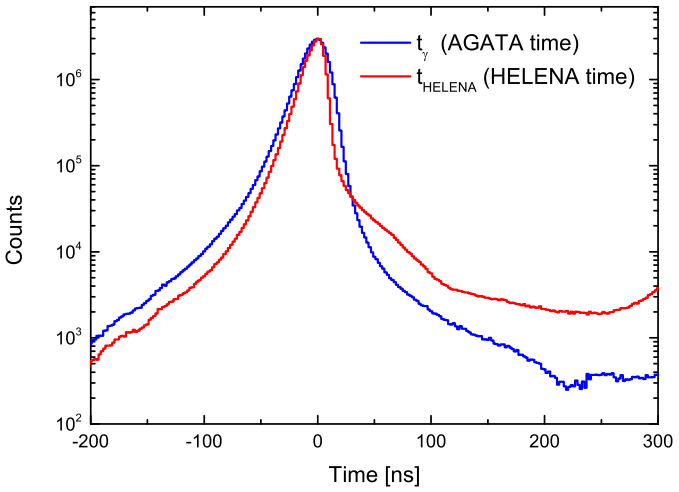

Figure 4.9: Comparison between time spectra t_γ and t_{HELENA} obtained using Eq. 4.2 and the TDC modules of the HELENA array, respectively.

4.2 Tracking performances

In order to have a quantitative evaluation of the tracking algorithm performances, same test have been done both on experimental and simulated energy spectra of AGATA.

Figure 4.10 shows an acquired spectrum before (black) and after (red) applying the tracking algorithm: as one can notice, there is a large reduction of the low-energy Compton background. There is, also, an improvement in the absolute area of the full energy peak, that increases with energy (see left panel of Fig. 4.12); these two effects lead to a better peak-to-total ratio, as reported in Fig. 4.12 (right panel). The AGATA fold distribution before and after γ-ray tracking is plotted in Fig. 4.11: as shown, after γ-ray tracking the fold distribution is peaked at lower values due to reconstruction of γ-ray event by grouping together 2 or more γ ray interaction points.

Concerning the simulated spectra, a GEANT4 code, developed by E. Farnea [54], is used to simulate monochromatic γ rays at $3, 6$ and 9 MeV, where pair production is the main interaction mechanism. The GEANT4 code gives as an output a file containing all the interaction points for each primary event; this file was used to perform the tracking on the simulated data with the MGT code [47], which is

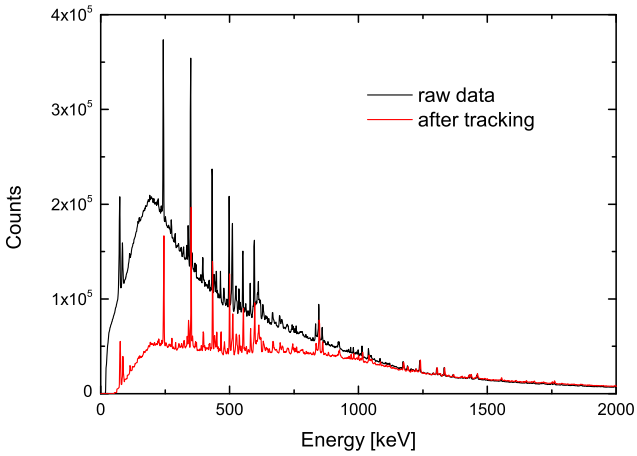

Figure 4.10: Typical HPGe energy spectrum from the reaction $^{50}Ti + ^{128}Te$ acquired during the experiment. Spectra before and after applying γ-ray tracking are plotted in black and in red respectively. The main effect of the tracking is a large, low-energy, background reduction.

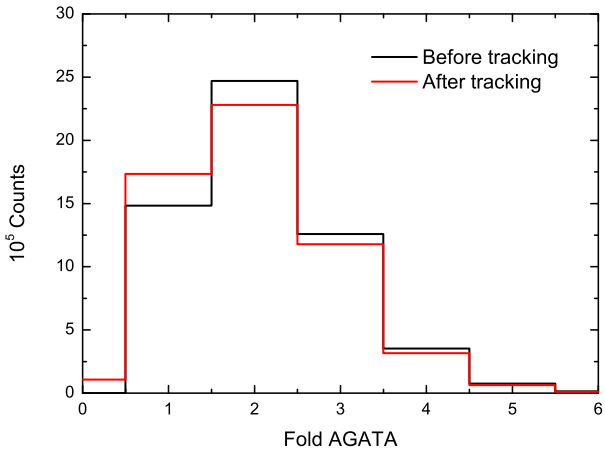

Figure 4.11: AGATA fold spectrum acquired during the experiment, before (black) and after (red) applying γ-ray tracking. After tracking the distribution is peaked at lower values, due to the grouping of 2 or more γ ray interaction as a unique γ event.

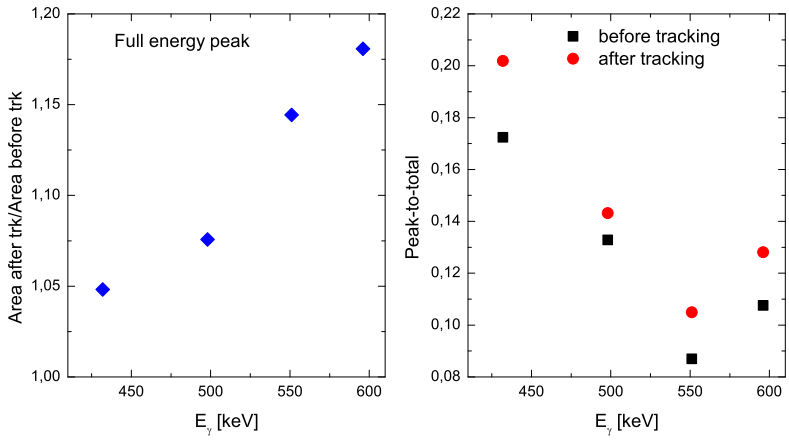

Figure 4.12: Improvement in the full energy peak area, defined as the ratio between the area after and before tracking (left panel); the improvement increases with γ-ray energy. On the right, peak-to-total ratio before (black squares) and after (red circles) tracking.

the same used for the experimental data.

Different AGATA configurations (with 3 and 5 triple clusters) have been considered, in order to test the performance of the array as a function of the number of detectors. On the left side of Fig. 4.13 a simulated spectrum for a γ ray of 3 MeV is shown before (black) and after (red) tracking. As observed for the experimental spectrum, there is a large reduction of the Compton background; furthermore there is a suppression (ratio < 1) of the 511 keV and the second escape peak and an improvement (ratio > 1) of the first escape and of the full energy peak. The analysis indicates that the tracking algorithm is able to recognised gamma interactions belonging to the same γ ray and to sum them together: for example it sums the contribution from two 511 keV interaction to a second escape interaction improving the total number of full energy peak events. Right panel of Fig. 4.13 summarises the results of the analysis. Concerning the dependence on the number of detectors, Fig. 4.14 shows that there are no differences in the improvement of full energy peak area in case of 3 or 5 clusters, for γ rays of 3 and 6 MeV. The improvement starts to become relevant at 9 MeV.

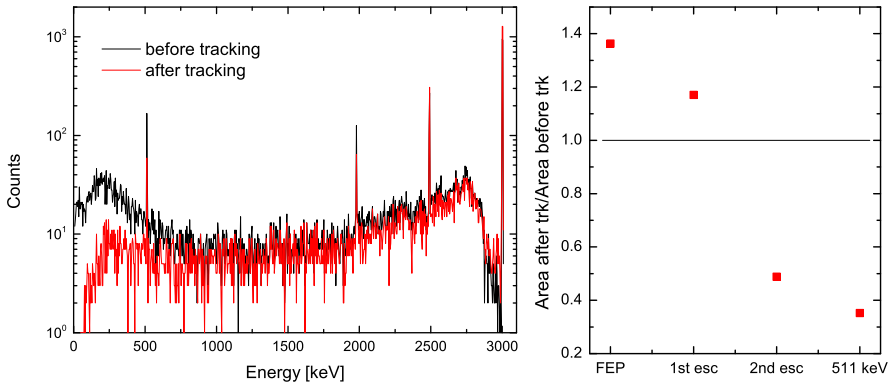

Figure 4.13: On the left: GEANT4 simulated spectra for monochromatic 3 MeV gamma-ray before (black) and after (red) tracking. After tracking there is a large reduction (ratio < 1) of the Compton background, of the 511 keV peak and the second escape peak, while the first escape and the full energy peak are enhanced (ratio > 1), as plotted on the right.

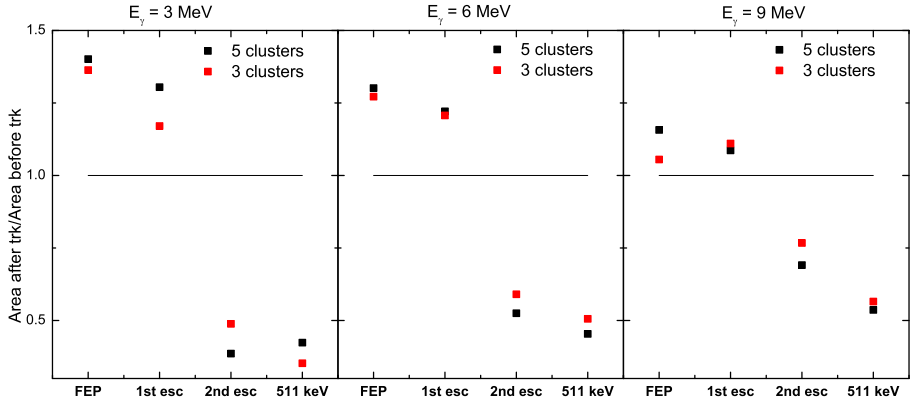

Figure 4.14: Test of the tracking performances with different γ-ray energies and AGATA configurations. No differences are observed in the full energy peak area at 3 and 6 MeV with 3 or 5 clusters. Effects due to the number of detectors are visible starting from 9 MeV.

4.3 Selection of the reaction channel of interest (^{174}W)

As discussed at the beginning of Chap. 3, the reaction used to populate ^{174}W was a fusion-evaporation reaction of ^{50}Ti on a ^{128}Te backed target.
In order to make a precise γ-spectroscopy analysis, it is better to separate at best events belonging to different reaction channels. Before the experiment, a PACE4 simulation [55] was run with the aim of evaluating the nuclei populated with the reaction. It was found that the two main evaporation residues are ^{173}W and ^{174}W, with a percentage intensity of 48.1% and 36.6% respectively. Other nuclei are populated with intensity less that 5%, so their contribution can be neglected.

In order to enhance the selectivity to ^{174}W, the HELENA information has been used. First, two "Sum energy vs Fold" ($\Sigma E_\gamma,\ F_\gamma$) matrices have been built in coincidence with the low-spin transitions of ^{173}W and ^{174}W nuclei respectively, as shown in Fig. 4.15. The gate transitions used to select ^{173}W are the 191 keV, 274 keV, 341 keV, 395 keV for the first decay path and 223 keV, 339 keV and 440 keV for the second one (see Fig. 4.17 and Ref. [56, 57]); while to select ^{174}W gates were put on 243 keV, 349 keV, 433 keV and 498 keV that collect all the decay flux (see Fig. 4.18). The total ($\Sigma E_\gamma,\ F_\gamma$) matrix has been used as a background: after it has been normalised to the number of counts and to the peak-to-total ratio of the gate transitions, it has been subtracted to the gated ($\Sigma E_\gamma,\ F_\gamma$) matrices. At this point, the matrices have been projected on their x and y axes, corresponding to fold F_γ and Sum Energy ΣE_γ respectively. The comparison between the obtained projections for ^{173}W and ^{174}W nuclei are shown in Fig. 4.16. As expected, the Sum-Energy and Fold distributions associated to ^{174}W are peaked at higher values, indicating that this nucleus has been populated at higher excitation energy and angular momentum. This means that to favour the selection of ^{174}W, an high-F_γ and high-ΣE_γ gating condition is needed. Based on these considerations and since the Sum Energy information is not so selective, the discriminating condition chosen for the further analysis is $Fold_{HELENA} \geq 4$.
This condition on HELENA will help also to focus on the high excitation energy and high spin region of the γ cascades, which is the region of phase-space mostly relevant for the present work.

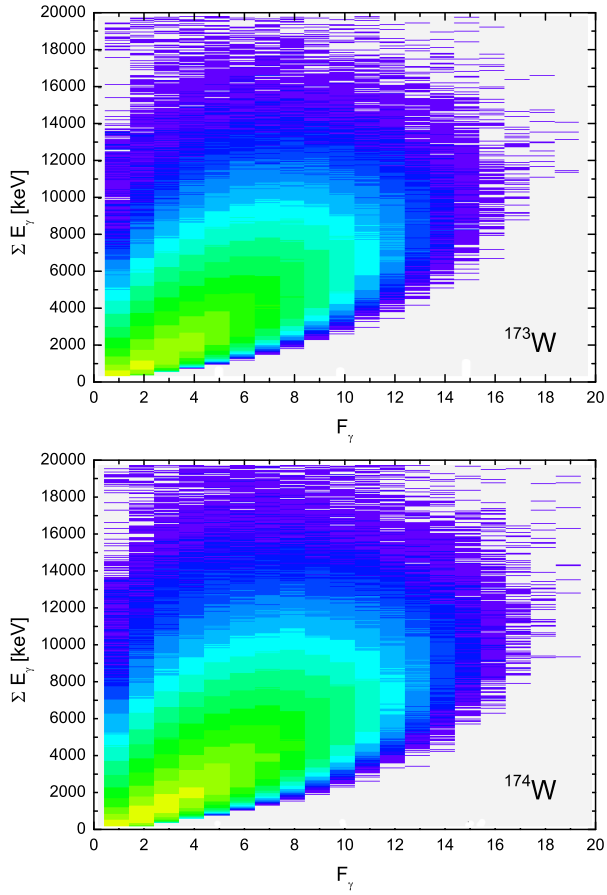

Figure 4.15: Comparison between the (ΣE_γ, F_γ) matrices obtained for ^{173}W (top) and ^{174}W (bottom).

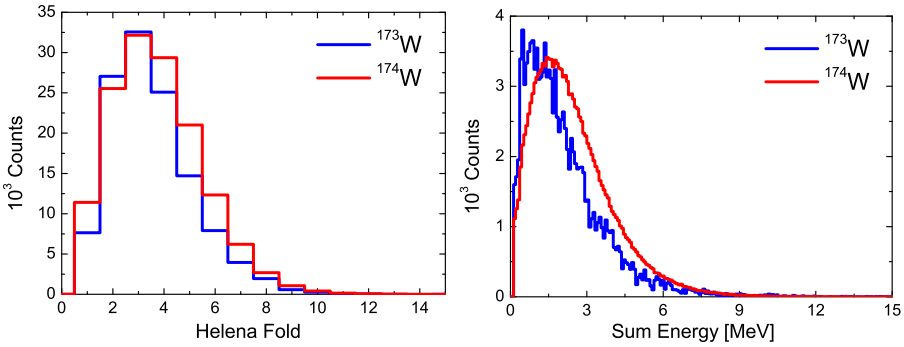

Figure 4.16: Comparison between HELENA Fold distributions (left) and Sum Energy spectra (right) obtained for ^{173}W (blue) and ^{174}W (red), respectively.

Through the analysis of the total $\gamma-\gamma$ matrix, the effects of the Fold condition on the relative population of ^{173}W and ^{174}W nuclei has been evaluated. As a first results, it was found that this reaction has populated ^{175}W too [56].

In order to evaluate the population intensity of each reaction channel, the total $\gamma-\gamma$ matrix, constructed using the condition $Fold_{HELENA} \geq 4$, was used to build their level schemes using the *escl8r* program of the Radware software package [48]. With this program, it is possible to analyse all γ lines of the input matrix in order to build the level scheme for the selected nucleus.
The level schemes obtained through the analysis of the experimental total $\gamma-\gamma$ matrix for ^{173}W, ^{174}W and ^{175}W are shown in Fig. 4.17, 4.18 and 4.19.

Each of these nuclei has different features, such as the kinematic moment of inertia $\Im^{(1)}$ which is related to E_γ and I through the relation $\Im^{(1)} = 2\hbar^2 \cdot I/E_\gamma$. E_γ as a function of spin for different nuclei is plotted in Fig. 4.20; the linear fit equation is also given for each case. By summing all intensities at a given spin value (or correspondingly at given E_γ using the fitted curves of Fig. 4.20), the percentage population for each nucleus has been extracted. As reported in Fig. 4.21, the nucleus of interest, i.e. ^{174}W, is populated at $\sim 60-80\%$. This means that using the condition $Fold_{HELENA} \geq 4$ the contribution of ^{173}W has been reduced but the contaminants nuclei are not negligible, especially above spin $16\hbar$. Therefore, further conditions are needed to select at best the nucleus of interest.

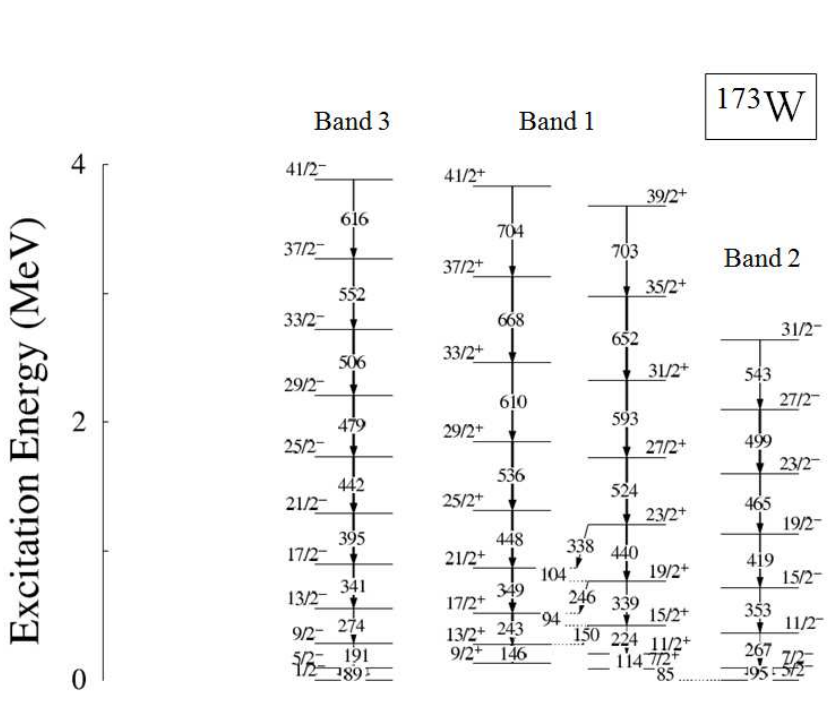

Figure 4.17: Level schemes of the ^{173}W nucleus populated by the reaction $^{50}Ti + ^{128}Te$, as obtained through the analysis of the experimental total $\gamma - \gamma$ matrix [56, 57].

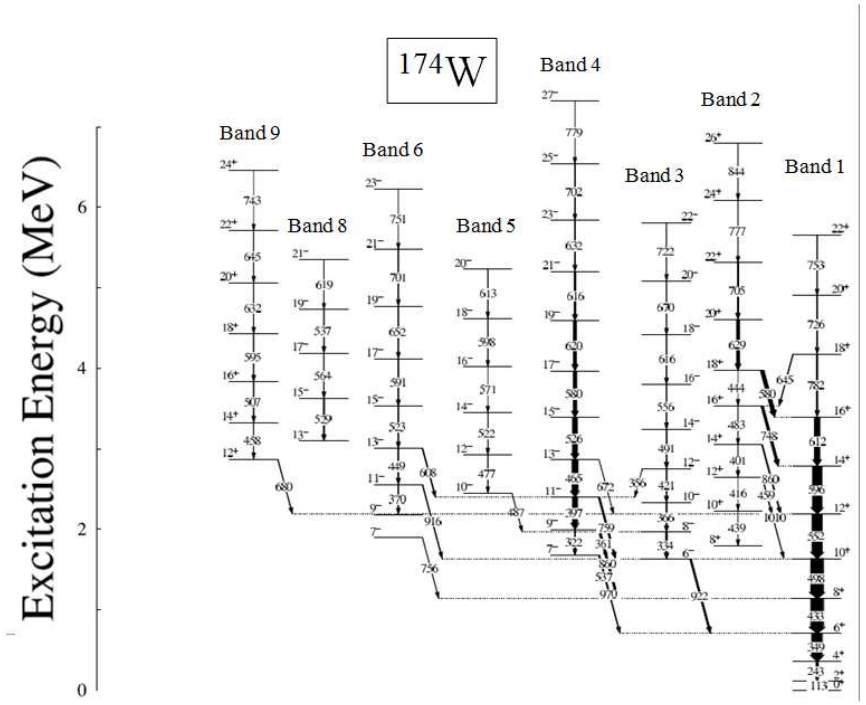

Figure 4.18: Level schemes of the ^{174}W nucleus populated by the reaction $^{50}Ti + ^{128}Te$, as obtained through the analysis of the experimental total $\gamma - \gamma$ matrix [5, 6].

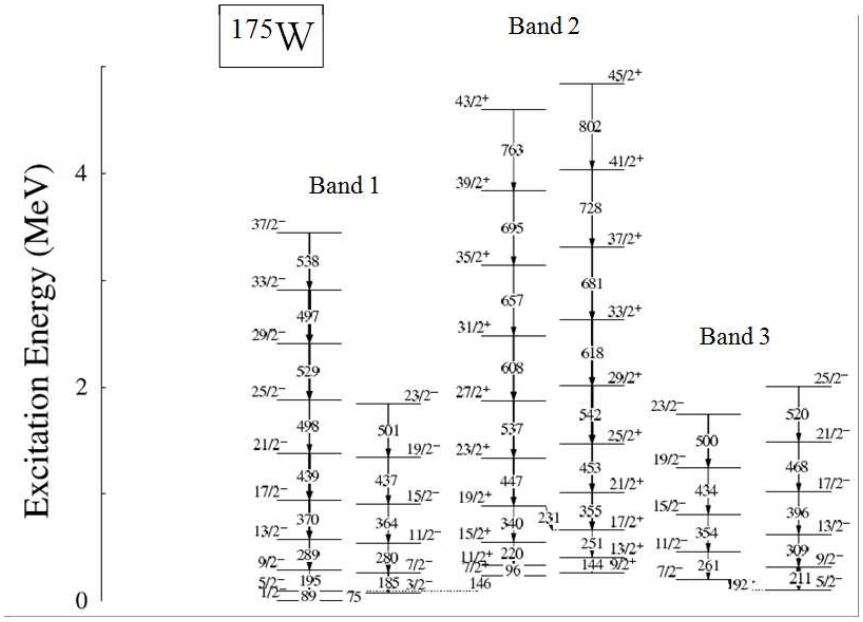

Figure 4.19: Level schemes of the ^{175}W nucleus populated by the reaction $^{50}Ti + ^{128}Te$, as obtained through the analysis of the experimental total $\gamma - \gamma$ matrix [56].

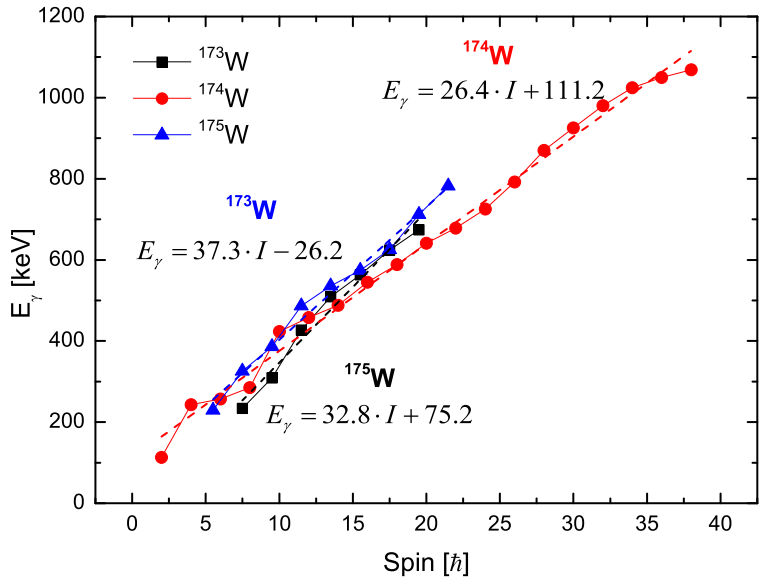

Figure 4.20: E_γ as a function of spin for the three residues: ^{173}W, ^{174}W and ^{175}W. The linear fit equation is also reported in each case.

4.4 Configuration selection

Once the contaminants nuclei have been roughly separated from the one we want to analyse through the fold condition $Fold_{HELENA} \geq 4$, more specific gates are needed to have a precise selection of the ^{174}W nucleus and to distinguish the low-K and high-K bands.

Using energy gating procedure it's possible to study γ coincidence spectra corresponding to different nuclear configurations separately. In fact, the selection of specific bands is made, for example, by sorting the cascades in coincidence with γ transitions corresponding to the configuration we want to study.
The gate is, in practice, a window delimited by a lower and a upper channel. If in a cascade a transition whose energy lies between these limits is found, then the remaining γ transitions are updated in the $\gamma - \gamma$ coincidence matrix.

This gating selection does not distinguish between the real peak component and the background under the peak: the incremented matrix has then a percentage of events which are in coincidence with the background and not with the real peak.

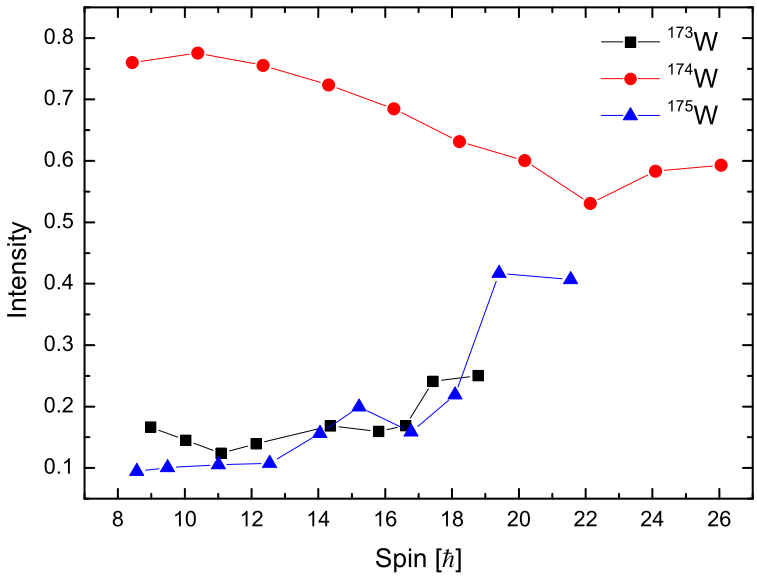

Figure 4.21: Population intensity for the three main residues nuclei (^{173}W, ^{174}W and ^{175}W) as a function of spin, as obtained by the analysis of the experimental data.

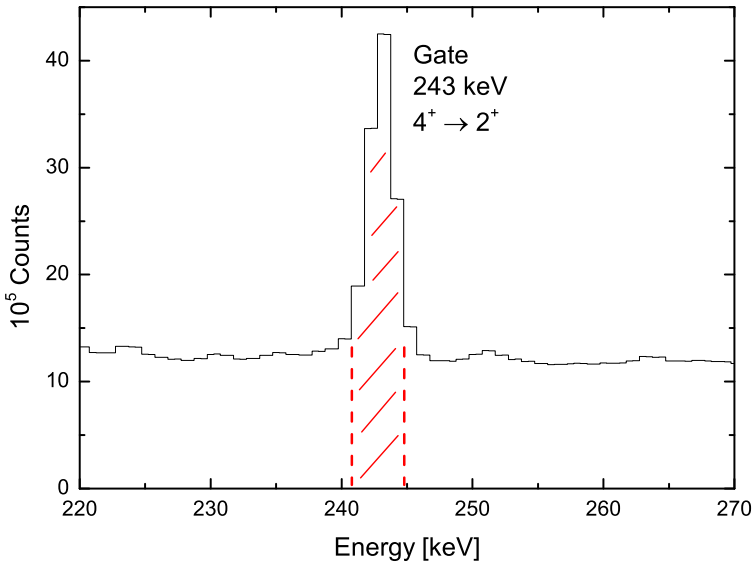

Figure 4.22: Example of energy gating window used to select the ^{174}W nucleus.

Fig. 4.22 shows an example of an energy gating window (marked with red dotted lines) used to select the ^{174}W nucleus: the selected peak, at energy of 243 keV, corresponds to the transition from the 4^+ to the 2^+ state in this nucleus (see level scheme in Ref. [5, 6]). It is clear from the picture that even events in coincidence with the background under the selected peak are updated in the gated matrix, since they fulfil the gating condition.
In order to reduce the background contribution a second matrix (named background, BG) has to be created: in our case it is represented by a total $\gamma - \gamma$ matrix, that is a matrix without any gating condition (i.e. the one used for contamination studies, described in Sec. 4.3).
The background spectrum BG is then subtracted from the gated spectrum $GATED$ using the relation:

$$RAW(x, y) = GATED(x, y) - g \cdot BG(x, y) \tag{4.3}$$

where $RAW(x, y)$ is the spectrum after the subtraction. The g factor is calculated evaluating the background over total ratio (B/T) of the selected peak, multiplied by the normalization factor N between the two spectra. Figure 4.23 shows examples of how the gating technique helps to separate the contributions from only one band. The top panel a) reports the total spectrum obtained from the reaction giving $^{178}W^*$ as compound nucleus: the strongest peaks (red arrows) belong to the yrast band of the ^{174}W nucleus, the most populated residue. The idea is, in this case, to create a spectrum which mostly contains the contribution of Band 4 (see level scheme of Fig. 2.2). Using the gating transitions reported in Tab. 4.2 a gated spectrum, shown in panel b), is created. After calculating the B/T ratio and normalising the gated and background spectra one to the other, the spectra in panel b) and a) are subtracted according to Eq. 4.3, resulting in the spectrum of panel c) (named RAW). It is evident that the contribution of the lines corresponding to Band 4 (green arrows) are much enhanced.

4.4.1 Total flux of ^{174}W

In order to have a more precise selection of the ^{174}W nucleus, gates on the low-spin transitions have been imposed. In this way, since these γ lines collect the entire decay flux, it is possible to increment a matrix that contains only γ rays belonging to the nucleus under study.

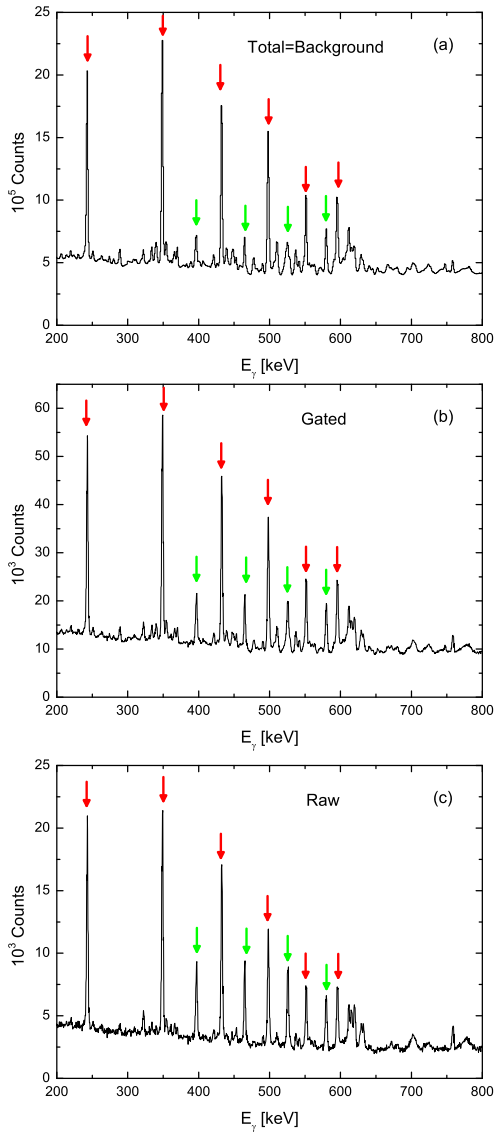

Figure 4.23: Panel a): the total γ-spectrum obtained in the fusion-evaporation reaction of ^{50}Ti on a ^{128}Te backed target, used as a background too. Panel b): spectrum obtained requiring the gating conditions reported in Tab. 4.2 to extract the contribution of Band 4. Panel c): difference between the spectra in panels b) and a), calculated according to Eq. 4.3. Peaks belonging to Band 4 are indicated by green arrows while yrast transition by red arrows.

Band 1	Band 2	Band 3	Band 4	Band 6
Energy [keV]	Energy [keV]	Energy [keV]	Energy [keV]	Energy [keV]
727	444	556	580	652
753	629	670	616	702
773	706	722	620	789
790	778	773	632	718
837	843	821	858	775
	896	868	929	850
	939	905	991	922
	1024		1042	990

Table 4.2: γ transitions used as gates to select the most intense low-K bands (cfr. Fig. 4.18).

The γ rays used to build this $\gamma - \gamma$ coincidence spectrum are the same used for the analysis of the HELENA "Sum energy vs Fold" matrices, i.e. 243 keV, 349 keV, 433 keV and 498 keV (see Fig. 4.18). After the matrix has been built with the energy gating procedure already described, Eq. 4.3 was applied for background subtraction. Since the average background over total ratio (B/T) of the selected peak was 0.53 and the normalization factor between the two spectra was 0.04, the g factor value obtained was $g = 0.53 \cdot 0.04 = 0.021$.

4.4.2 Low-K selection

For low-K bands, the energy gating procedure, explained at the beginning of Sec. 4.4, has been used. The five most intense bands have been selected using high-spin transitions, not belonging to other bands. The γ transitions used as gates are reported, for each band, in Tab. 4.2. A prompt time condition was used too, because all the low-K bands don't have isomeric transitions; the time condition was $-20ns \leq t_{HELENA} \leq 10ns$, centred around $t = 0ns$: the region is delimited by blue lines in Fig. 4.24. The procedure of energy gating and background subtraction was the same as for the total ^{174}W matrix, with g factors reported in Tab. 4.3.

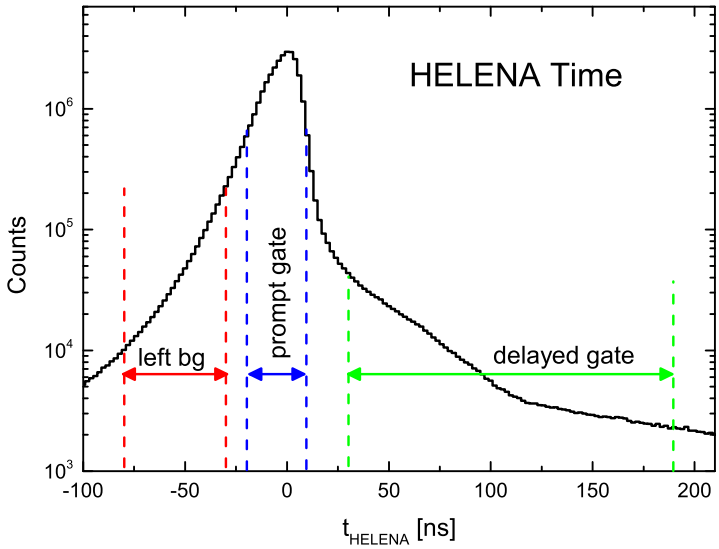

Figure 4.24: Different time gates on the HELENA time spectrum: in blue is indicated the prompt time gate region, in green the delayed one. The left region used as background is delimited by red lines.

	Band 1	Band 2	Band 3	Band 4	Band 6
<B/T>	0.96	0.92	0.95	0.79	0.91
N	0.019	0.022	0.016	0.023	0.021
g	0.018	0.020	0.015	0.018	0.019

Table 4.3: g factors used for background subtraction of the low-K matrices. (B/T) ratios are averaged over the selected gating transitions. N is the normalization factor between $GATED$ and BG spectra.

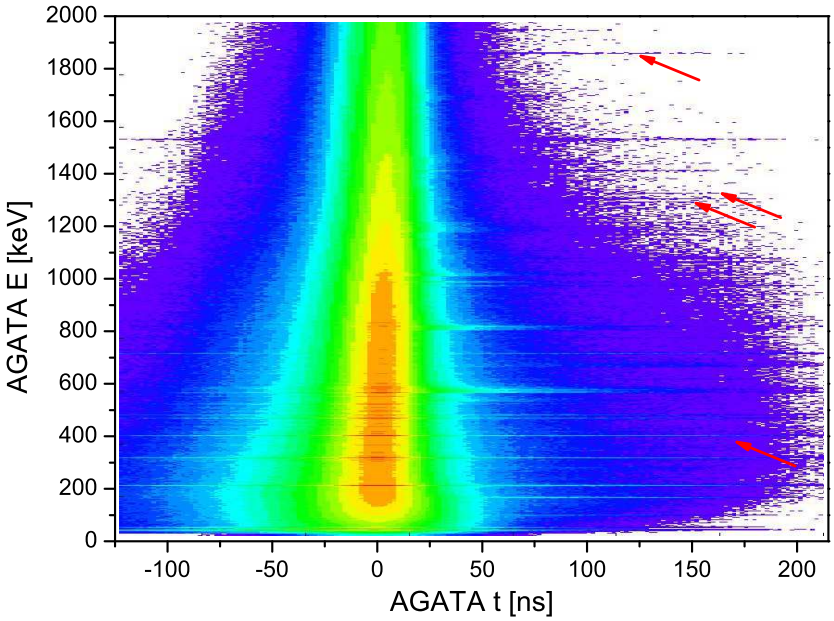

Figure 4.25: AGATA Energy versus time matrix. Red arrows show some of the isomeric gamma rays that de-excite the High-K bands, the most visible of which is the 1879 keV line (cfr. Fig. 2.3).

4.4.3 High-K selection

For the high-K bands, it wasn't possible to use the standard gating procedure on γ ray energies because the intensity of the γ rays belonging to high-K states is very weak (of the order of 1%), resulting in a very poor selectivity.
An alternative way to proceed is to select the high-K bands through the long-lived isomeric gammas associated to their decay. To check this possibility, some tests have been done. First, an E_γ vs $Time$ matrix has been built for the AGATA events: as one can see in Fig. 4.25 the isomeric gammas associated to the high-K bands decay extend up to long times. Putting a gate on these isomeric transitions, the corresponding time spectrum shows an enhanced bump in the delayed region (as one can see in Fig. 4.26 upper panel), with respect to the same time spectrum obtained by gating on the energy of prompt γ rays. On the other hand, if one gates on the delayed times, the isomeric γ transitions associated to the decay of the high-K bands show an increased intensity, while contributions of prompt γ rays

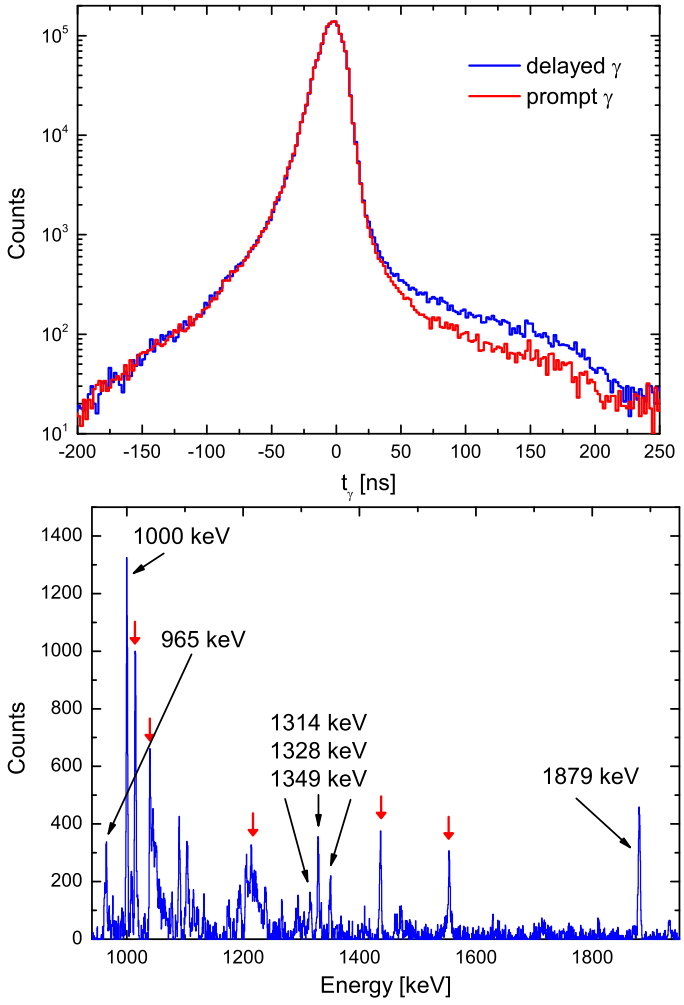

Figure 4.26: Upper panel: time spectra obtained by gating on energy of prompt (red) or delayed (blue) γ rays. Lower panel: energy spectrum obtained by gating on delayed transitions: isomeric γ rays are indicated by black arrows; red thick arrows denote peaks due to neutrons and natural background.

are largely suppressed (see lower panel of Fig. 4.26).
These results clearly indicate that we can use time gates instead of energy gates to select the contribution of the high-K structures from the total decay flux.
The final condition used to select high-K bands was $30ns \leq t_{HELENA} \leq 190ns$ (green lines of Fig. 4.24), in addition to the high fold condition $Fold_{HELENA} \geq 4$ (used for all the matrices).

Since this matrix has not been built using energy gate, a different background subtraction has been performed, based on a time-background matrix .
As already mentioned in Sec. 4.1.3, the left part of the spectra in Fig. 4.8 contains background events. For this reason, a $\gamma - \gamma$ coincidence matrix with "left" time gate ($-80ns \leq t_{HELENA} \leq -30ns$, in red in Fig. 4.24) has been constructed, to be used as background. The g factor of Eq. 4.3 was calculated according to the number of time-gating channel, that is 160 ch for the high-K gated matrix (delayed gate) and 50 ch for the "left" time gate (background). Equation 4.3 was then applied, setting $g = 2.6$.

Chapter 5

Analysis of the quasicontinuum spectra

5.1 The Fluctuation Analysis Method (FAM)

The study of the nuclear rotational motion at high excitation energy can not be performed through the analysis of discrete gamma transitions of energy E_γ or by coincidence peaks of intensity I_{γ_1,γ_2}. When the rotational motion becomes damped, as a consequence of the mixing between densely spaced rotational levels, it is not possible to distinguish single gamma transitions in the energy spectra. Instead a "quasi-continuum" distribution, that starts filling even the valley region (defined by $E_{\gamma 1} = E_{\gamma 2}$) in $\gamma - \gamma$ coincidence spectra, is observed, as explained in Chap. 1. The study of the warm rotation can be done by analysing the shape of the quasi-continuum distribution, or by analysing the fluctuations of counts in the γ energy spectrum [4, 8]. Both techniques can be applied to two-dimensional (2D) coincidence spectra, in which one can distinguish the contribution of the cold regular bands from that of strongly mixed excited bands: the first populate the ridges while the second the valley (see Fig. 5.3).

The fluctuation analysis method aims at measuring the number of decay paths available to the nuclear rotational decay. It relies on the fact that the typical spacing between two consecutive transitions in a rotational cascade is $4\hbar^2/\Im^{(2)}$, which implies that each cascade contributes, on average, to only one count every

$4\hbar^2/\Im^{(2)} \times 4\hbar^2/\Im^{(2)}$ interval in a $\gamma-\gamma$ energy spectrum. The path is then characterized by the nuclear levels involved in the decay and not only by the γ energies [8].

The number N_{eve} is defined as the number of events recorded in a $4\hbar^2/\Im^{(2)} \times 4\hbar^2/\Im^{(2)}$ interval close to the diagonal or centred around the first ridge, in case of analysis of damped motion or discrete bands, respectively.

Any two γ-rays with energy in the selected window and emitted in coincidence in a cascade define a *decay path i*. The reaction and the nuclear structure determine for each path a probability W_i of following the path *i*. In particular, the largest probabilities are carried by the most relevant paths, such as two consecutive transitions in a strong discrete rotational band like the yrast band. The rest of the paths, especially false paths with Compton transitions, will form a background, which can be taken care of by background-subtraction procedures. The *channels* are denoted by the letter *j*.

For given energy E_i and path probability W_i, the probability Q_j for an event to be recorded in channel number j is found by summing over paths:

$$Q_j = \sum_i W_i P_j(E_i) \tag{5.1}$$

where $P_j(E_i)$ is the probability of detecting energy E_i in channel *j*. The probability distribution for detecting M_j out of N_{eve} events in channel j is binomial. This results in the following first and second moments of the number of counts:

$$\langle M_j \rangle = N_{eve} Q_j = N_{eve} \sum_i W_i P_j(E_i) \tag{5.2}$$

$$\langle M_j^2 \rangle = N_{eve}(N_{eve}-1)Q_j^2 + N_{eve}Q_j \simeq N_{eve}^2 \sum_{ii'} W_i P_j(E_i) W_{i'} P_j(E_{i'}) + \langle M_j \rangle \tag{5.3}$$

The aim of the fluctuation analysis is to determine the number of paths without knowing in detail the transition energies and the transition probabilities.

If the nucleus follows a finite number of decay paths during its cascade, filling the selected 2D window in a $\gamma-\gamma$ coincidence matrix, there is a relation between the number of decay paths and the count fluctuations in the spectra. In order to explain the relation between the number of available paths and the fluctuations of counts, it is useful to consider a simple numerical example. If one assumes to distribute in a random way a number of paths N_{path} in a number of channels N_{ch},

one obtains a binomial statistical distribution, so that the average number of paths per channel, called first moment and indicated by $\mu_1(path)$, and the variance of the path distribution, called second moment $\mu_2(path)$ are comparable, namely

$$\mu_1(path) = \frac{N_{path}}{N_{ch}} \tag{5.4}$$

$$\mu_2(path) = \frac{N_{path}}{N_{ch}} \left(1 - \frac{1}{N_{ch}}\right) \approx \mu_1(path) \tag{5.5}$$

Assuming to have a number of events equally distributed in the available paths, the following distribution of events in the N_{ch} channels with moments μ_1 and μ_2 is obtained

$$\mu_1(counts) = \mu_1(path)\frac{N_{eve}}{N_{path}} \tag{5.6}$$

$$\mu_2(counts) = \mu_2(path)\left(\frac{N_{eve}}{N_{path}}\right)^2 \approx \mu_1(counts)\frac{N_{eve}}{N_{path}} \tag{5.7}$$

In case of high statistics $N_{eve} \gg N_{path}$, then

$$\frac{\mu_2(counts)}{\mu_1(counts)} = \frac{N_{eve}}{N_{path}} \geq 1 \tag{5.8}$$

This means that there is an amplification of the fluctuations in the number of counts due to the presence of a small number of available paths.
If one takes into account that a random distribution of N_{eve} in N_{path} paths with equal probability gives rise to binomial distribution of fluctuations in the average number of events per path, one obtains from the composition of the two different contributions, the following relation [8]

$$\frac{\mu_2(counts)}{\mu_1(counts)} = \frac{N_{eve}}{N_{path}} + 1 \tag{5.9}$$

This is the basic relation of the fluctuation analysis technique, since it relates the number of paths with the first and second moments μ_1 and μ_2 of the distribution of counts in the spectra. Eq. 5.9 tells that few paths lead to strong fluctuations of the spectrum, and vice versa.
It is worth noticing that in the case of a large number N_{path} of paths compared to the number N_{eve} of events, as in the valley analysis of experimental spectra, N_{eve}/N_{path} can be very small, so that μ_2/μ_1 tends to the statistical limit $\mu_2/\mu_1 \approx 1$.

This is the limit reached when N_{eve} events are randomly distributed directly in N_{ch} channels, without using the paths distribution.
Eq. 5.9 contains all the information needed to study the fluctuations of counts in the experimental spectra, although it has to be first generalized in order to include the resolution of the detection system, the different probability of population for the paths and the extension to the two-dimensional case.
The whole derivation can be found in [8], while only the final expressions to be used for 2D spectra are here reported:

$$\mu_1 = \frac{N_{eve}}{N_{ch}} \tag{5.10}$$

$$\begin{aligned}\mu_2 = \frac{N_{eve}^2}{N_{ch}} \sum_j \sum_{ii'} \left(\langle W_i W_{i'}\rangle - \langle W_i\rangle\langle W_{i'}\rangle\right) \langle P_j(E_i) P_j(E_{i'})\rangle + \\ + \sum_j \sum_{ii'} \langle W_i\rangle\langle W_{i'}\rangle \left(\langle P_j(E_i) P_j(E_{i'})\rangle - \langle P_j(E_i)\rangle\langle P_j(E_{i'})\rangle\right) + \mu_1\end{aligned} \tag{5.11}$$

where for each path i, with transition energy E_i, W_i is the probability to follow the path i, while, for each channel j, $P_j(E_i)$ is the probability that the energy E_i is detected in channel j. The average is over all possible realizations, following the assumption that the nucleus is a particular realization of a random distribution of nuclei.
From these general expressions two different cases can be distinguished for the random distributions underlying the realizations, corresponding respectively to the regular rotational bands and the strongly interacting bands:

1. *ridge analysis (large fluctuations)*: in the case of regular rotational bands the transition energies E_i will be considered to be randomly distributed. This implies that the first term in Eq. 5.11 is negligible. In addition, one can include a generalization that takes into account the finite resolution of the spectra, namely the $P^{(n)}$ factors representing the probability of detection, given by

   $$P^{(n)} = \frac{\int (P_j(E))^n dE}{\int dE} \tag{5.12}$$

   After this, Eq. 5.11 becomes

   $$\mu_2 = \frac{N_{eve}^2}{N_{ch}} \sum_j [P_j^{(2)} - (P_j^{(1)})^2] \sum_i \langle W_i\rangle^2 + \mu_1 \tag{5.13}$$

Since $(P_j^{(1)})^2$ is negligible as compared to $P_j^{(2)}$ and $\frac{1}{N_{ch}}\sum_j P_j^{(2)} \approx P^{(2)}$ we obtained the relation:

$$\frac{\mu_1}{\mu_2} = \frac{N_{eve}}{N_{path}^{(2)}}\frac{P^{(2)}}{P^{(1)}} + 1 \tag{5.14}$$

where

$$N_{path}^{(2)} = \frac{1}{\sum_i \langle W_i \rangle^2} \tag{5.15}$$

$N_{path}^{(2)}$ is called the *effective number of paths of order 2*.
The effective number of paths $N_{path}^{(2)}$ is equal to the real number of paths N_{path} only in the case that all W_i values are equal (equiprobability), otherwise it gives only a lower limit for the real number of paths.

2. *Valley analysis (small fluctuations)*: for the damped region of strong interacting bands a smooth energy spectrum is considered, while the transition probabilities will have considerable fluctuations of Porter-Thomas nature. In this case the second term of Eq. 5.11 is negligible and one finds

$$\frac{\mu_1}{\mu_2} = \frac{N_{eve}}{N_{path,PT}^{(2)}}\frac{P^{(2)}}{P^{(1)}} + 1 \tag{5.16}$$

where

$$N_{path,PT}^{(2)} = \frac{1}{\dfrac{4}{N_{path}^{(2)}} + \dfrac{4}{n_{path}^{(2)}}\dfrac{(p^{(1)})^2}{p^{(2)}}} \tag{5.17}$$

being $n_{path}^{(2)}$ the analogous of $N_{path}^{(2)}$ in one dimension, that is:

$$n_{path}^{(2)} = \frac{1}{\sum_i \langle w_i \rangle^2} \tag{5.18}$$

and $p^{(n)}$ is the analogous of $P^{(n)}$ in one dimension.
In this case the value $N_{path,PT}^{(2)}$ cannot be easily related to the real number of paths N_{path}, but can anyhow be used to compare experimental and theoretical values.

The fluctuation analysis method is characterised by an intrinsic uncertainty due to the fact that the theoretical results are obtained as an average over realizations, while the experimental results represent just one of the possible realizations. One

can estimate the intrinsic uncertainty from the variance on the second moment μ_2, given by the expression [8]

$$\mu_2(\mu_2) \approx \frac{2}{N_{ch}}[(\mu_2 - \mu_1)^2 + \mu_1^2] \tag{5.19}$$

which holds both for the ridges and valley analysis.

5.1.1 Energy resolution correction factors

The finite energy resolution of the detectors array gives rise to the population of several channel for each γ transition energy, instead of one in case of ideal energy resolution. Ideally the probability distribution of detecting path i in channel j is a step function equal to 1 in channel j. In reality, the probability distribution is, as a first approximation, a Gaussian function whose Full Width Half Maximum (FWHM) depends on the energy detected by the array. The trend of the energy resolution of the AGATA array as a function of E_γ is plotted in Fig. 3.8. Furthermore channels of the matrices have finite amplitude, that is 4 keV for simulated matrices and 4 or 8 keV for experimental ones.
The event distribution in the matrix is modified by this two factors, with respect to the ideal distribution obtained having infinite energy resolution and ideal channels. In order to correct these effects is useful to define moments of detection probability as

$$p^{(n)} = \int (p_j(E))^n dE / \int dE \tag{5.20}$$

where $p^{(1)} = 1/n_{ch}$, in the case of mono-dimensional spectra.
As already shown, in two dimensions Eq. 5.20 becomes

$$P^{(n)} = \int (P_j(E))^n dE / \int dE \tag{5.21}$$

where $P^{(1)} = 1/N_{ch}$.
Obviously, $P^{(n)} = (p^{(n)})^2$ because a bi-dimensional probability is the product of the mono-dimensional ones.
In the present work, the second order momenta of the probability distributions were used, because the number of paths 2 steps long has been extracted. Values $(p^{(2)}/p^{(1)})$ as a function of transition energy are plotted in Fig. 5.1, for different binning factor (i.e. 4 keV/ch and 8 keV/ch).

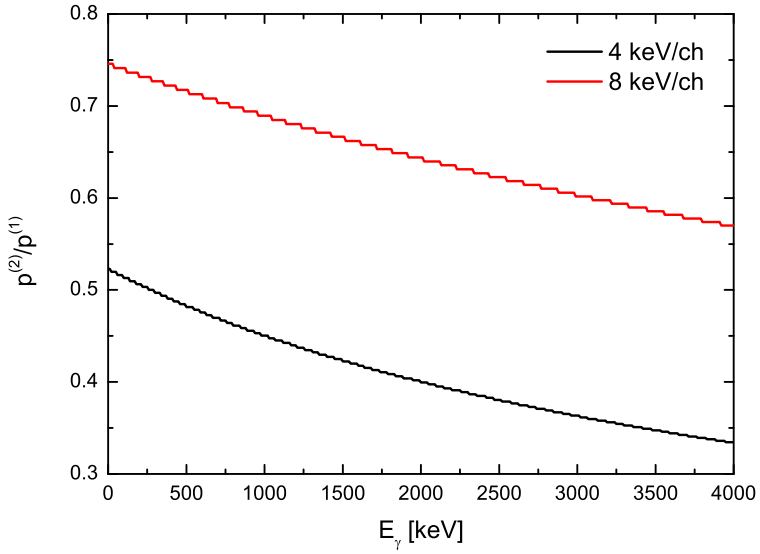

Figure 5.1: Corrective factors ($p^{(2)}/p^{(1)}$) as a function of transition energy, for different binning factor (i.e. 4 keV/ch in black and 8 keV/ch in red).

5.2 Experimental procedure

The statistical fluctuation method, as explained in Sec. 5.1, allows to extract the average number of paths followed by the nucleus in its de-excitation.
In the experimental spectra, the counts distribution over channels is partially contaminated by background. Sec. 5.2.1 describes how background is subtracted.
The experimental resolution has to be taken into account as well, since it distributes the counts relative to the energy E_γ in an area $FWHM(E_\gamma)$, and so the fluctuations are attenuated in the same area, diminishing their value. This is taken care by the $P^{(n)}$ parameters which can be estimated assuming a Gaussian shape for the probability distribution to detect a path in channel j, with a $FWHM$ that depends on the energy of the detected transition. This is given by the experimental energy resolution (see Sec. 5.1.1).

5.2.1 Uncorrelated background subtraction

The Compton background is removed trough subtraction techniques for uncorrelated events: this method is called *COR* [58, 59]. Among different methods of

Compton background subtraction, this one is the most suitable for statistical fluctuation analysis, because it calculates the uncorrelated events distribution from the original spectrum; in this way it can reduce valley contaminations, due to discrete bands features, such as backbending and high-energy γ rays in coincidence with high-spin transitions.

The *COR* procedure is based on the fact that coincidence full-energy-peak events are correlated, while Compton background events are distributed randomly in the spectrum. Therefore, for background events, the probability to have one counts in channel (x, y) is equal to the probability to have one counts in channel x multiplied by the probability to have one counts in channel y.

A double $\gamma - \gamma$ coincidence spectrum composed only by uncorrelated events can be built starting from the original *RAW* spectrum (obtained according to Eq. 4.3) as follows

$$UNCOR(x, y) = P_x P_y \sum_{x,y} RAW(x, y) \tag{5.22}$$

where P_x and P_y are the probability to detect one count in channel x or y, defined as

$$P_i = \frac{\sum_i RAW(i, j)}{\sum_{i,j} RAW(i, j)} \tag{5.23}$$

P_i is the ratio between the total projection over one axis and the number of counts of the 2D spectrum.

The *UNCOR* spectrum is then calculated as

$$UNCOR(x, y) = \frac{\sum_x RAW(x, y) \sum_y RAW(x, y)}{\sum_{x,y} RAW(x, y)} \tag{5.24}$$

Defined in this way, the *UNCOR* and *RAW* spectra have the same number of counts, but distributed in a different way, because the *RAW* spectrum contains only correlated events. Since the total number of counts includes correlated events too, the *UNCOR* spectrum is overestimated. For this reason the *UNCOR* spectrum is scaled down by a factor that depends not only from the experiment and the detector array but also from the gating conditions used to build the spectrum.

The final *COR* spectrum, containing mainly correlated events, is obtained as follows

$$COR(x, y) = RAW(x, y) - f \cdot UNCOR(x, y) \tag{5.25}$$

where f is equal to 0.7. The value of f has been chosen in order to make the ridge-valley structure as clean as possible, avoiding regions with negative counts.

Fig. 5.2 shows an example of the *COR* procedure applied to the high-K matrix: panel a) shows the *RAW* matrix and panel b) the *UNCOR* matrix; in panel c) the matrix obtained using the *COR* procedure with a *COR* factor $f = 0.7$ is shown. As one can see, in the *RAW* matrix it is not possible to distinguish the presence of the ridge-valley structure while in the *UNCOR* matrix the strong background structures running parallel to the axis of the matrix become very visible. After the *COR* procedure the matrix shows rather clearly the ridge-valley structure typical of rotational nuclei.

5.2.2 Level schemes construction

Level schemes of ^{174}W have been investigated using information extracted from bi-dimensional spectra, such as coincidence peak intensities and transition energies. In particular, level schemes have been constructed for all the matrices built with the gating procedure explained in Sec. 4.4, using the program *ESCL8R* of the *RADWARE* package [48].
ESCL8R is an interactive program for graphics-based analysis of $\gamma-\gamma$ data for the deduction of level schemes. It allows fast and easy inspection of the $\gamma-\gamma$ matrix; the matrix is symmetrised, so that the two energy axes are equivalent. In addition to the coincidence matrix, the program requires a two-dimensional background, and knowledge of the peak shapes and widths as a function of γ-ray energy and the efficiency and energy calibrations, parametrized as reported in Sec. 3.1.7 and 3.1.8.

5.2.3 Discrete lines removal

Before proceeding in the fluctuation analysis (see Sec. 5.3), the most intense γ lines have to be removed from the *COR* spectra. In fact, the obtained number of path, N_{path}, converge to the real value if the hypothesis of equal path probability is satisfied. Therefore, the presence of even only one very intense transition increases the fluctuations and decreases the number of paths N_{path} extracted with the experimental analysis. On the contrary, if experimentally-resolved γ lines are correctly subtracted from the spectrum, it is reasonable to suppose that the remaining transitions have approximately the same intensity. The corresponding fluctuations can therefore be extracted without being biased by the strongest ones.

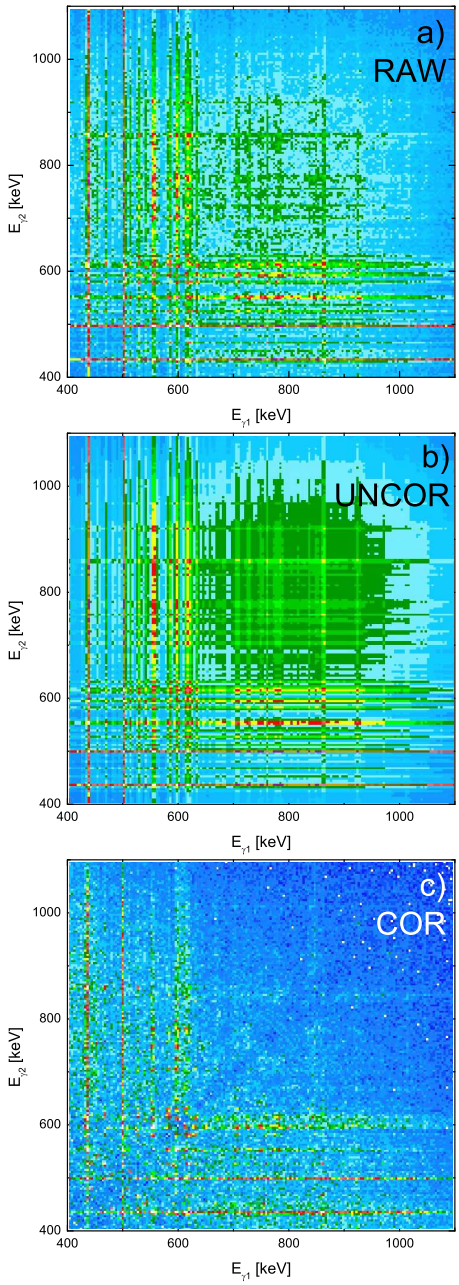

Figure 5.2: Panel a): the RAW high-K matrix of ^{174}W. Panel b): the *UNCOR* matrix. Panel c): matrix obtained using the *COR* procedure with a *COR* factor $f = 0.7$.

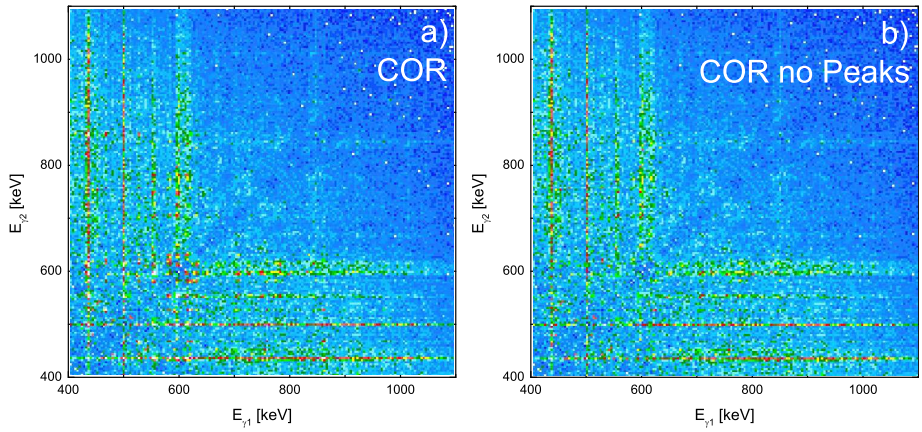

Figure 5.3: Panel a): the *COR* high-K matrix of ^{174}W before discrete lines removal. Panel b): the *COR* matrix after peaks subtraction. Especially near the valley structure at $\sim 600 - 800$ *keV* the effect of the subtraction is more evident.

After the Compton background has been removed, the discrete lines known by the analysis of $\gamma - \gamma$ matrices (see Sec. 5.2.2) have been subtracted through the *SUBPEAK* program of the *RADWARE* package: this program builds a bi-dimensional spectrum composed by discrete lines to be subtracted to the *COR* matrix, starting from the level scheme and transition intensities obtained through the *ESCL8R* program. Fig. 5.3 shows the *COR* spectrum before (on the left) and after (on the right) discrete lines removal. It is important to underline that not the whole level scheme [5, 6] has been subtracted, but only γ lines visible and resolvable in the analysed experimental matrices: this corresponds to only 6-8 strongest bands out of a total 20 known from literature.

5.2.4 Moments calculation

The moments μ_1 and μ_2 of the events distribution, needed to evaluate the N_{path} number of paths (through Eq. 5.14 and 5.16), can be extracted from the experimental 2D-spectra of $\gamma - \gamma$ coincidences making use of the program $STATFIT$ [8, 60]. The code performs a polynomial interpolation of the 2D-spectrum and calculates the first and second moments of the original spectrum with respect to this polynomial surface [8]. The calculation of the first and second momentum

is made starting from the interpolation function, which is itself a 2D spectrum $Fit(x_0, y_0)$, considering an area around each (x, y) combination of $k \times k$ channels and calculating in this window the quantities

$$\mu_1(x_0, y_0) = \sum_{x,y \in K} COR(x, y) f_G(x - x_0, y - y_0) \tag{5.26}$$

$$\mu_2(x_0, y_0) = \sum_{x,y \in K} (COR(x, y) - Fit(x, y))^2 f_G(x - x_0, y - y_0) \tag{5.27}$$

f_G is a weighting function of Gaussian shape centred around the point (x_0, y_0) and normalised so that $\sum_{k,l} f_G(x - x_0, y - y_0) = 1$. The first momentum μ_1 is the weighted average of the spectrum, while the second moment μ_2 is the standard deviation. As shown in Fig. 5.4, in the μ_2 spectrum, as compared to the COR or the μ_1 spectrum, the fluctuations in the ridges are much larger than the ones in the valley. This confirms the assumption that the valley is populated by a much larger number of transitions with a decay fragmented over a high number of states, as in the case of the rotational damping regime (see Sec. 1.4).

5.2.5 Moments spectra integration

The number of decay paths is calculated from the number of events N_{eve} and from the first and second moments, μ_1 and μ_2, using the following expression (derived from Eq. 5.14):

$$N_{path} = \frac{N_{eve}}{\dfrac{\mu_2}{\mu_1} - 1} \frac{P^{(2)}}{P^{(1)}} \tag{5.28}$$

where $P^{(2)}/P^{(1)}$ is a correction factor that takes into account the finite resolution of the detection array (see Sec. 5.1.1).

Integration windows are extracted from bi-dimensional $(E_{\gamma 1}, E_{\gamma 2})$ spectra; their width is set to $\Delta E_\gamma = 4\hbar^2/\Im^{(2)} = 60\ keV$ in each dimension, that is the typical energy separation of two consecutive transition in the rotational cascade of ^{174}W. In this way, each cascade gives one count in each window, and the fluctuation of the number of counts per channel is directly related to the number of paths available to the nucleus de-excitation.

The analysis is applied in the energy region between 700 keV and 1100 keV, where the majority of the decay flow of ^{174}W is concentrated. In particular, we focus on

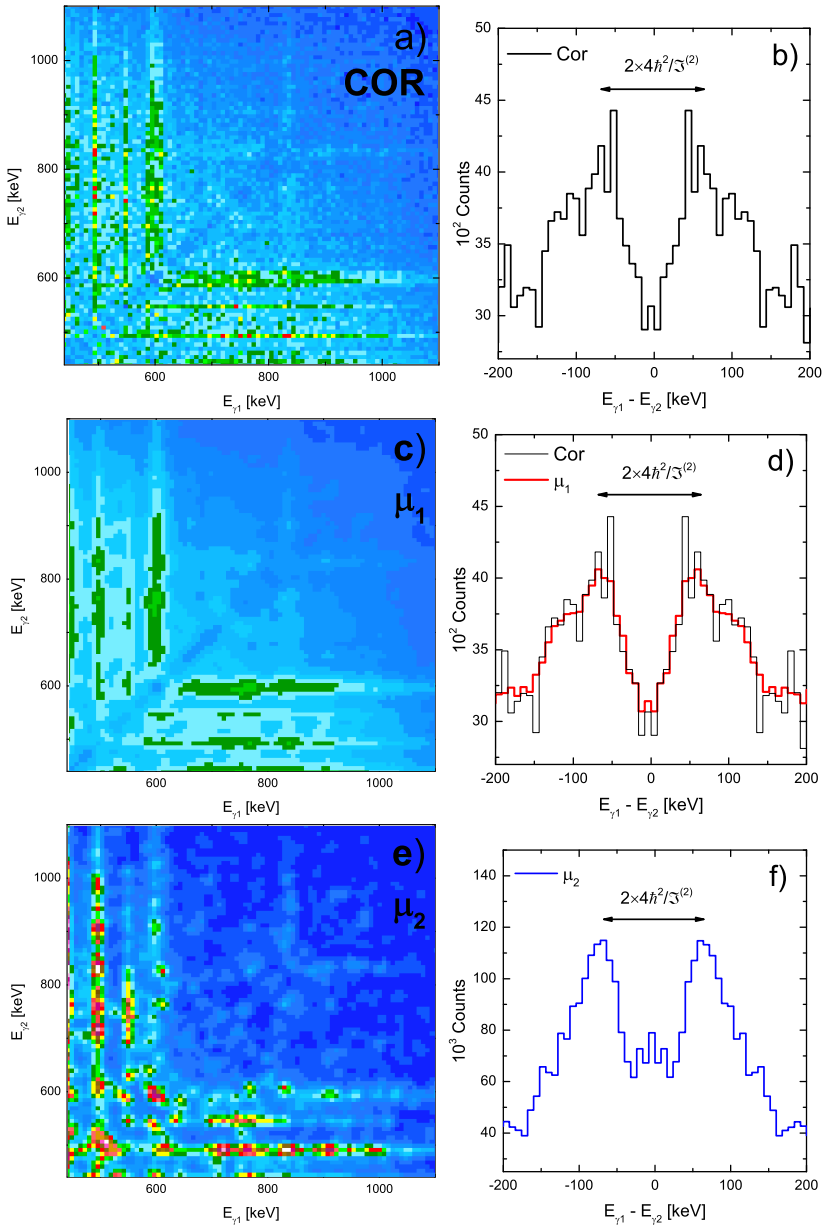

Figure 5.4: Panel a): example of COR spectrum relative to high-K bands. The corresponding μ_1 and μ_2 spectra obtained from the $STATFIT$ code are reported in panel c) and e) respectively. Note that the full scale for the μ_2 matrix is 18 times the other ones. Perpendicular cuts (60 keV wide) at $\langle E_\gamma \rangle = 880$ keV are shown on the right side of the figure (panels b), d) and f)).

the ridges structures, which are are populated by γ transitions belonging to regular rotational motion, not experimentally resolved due to their very low intensity (see Sec. 5.2.3). The number of paths evaluated using this technique will determine the average number of rotational bands, at least two steps long, not experimentally resolved. The γ transitions emitted in the warm regime of rotational damping are instead distributed over the whole spectrum and the most suitable region to extract the number of paths related to them is the central $E_{\gamma 1} = E_{\gamma 2}$ valley; in this region there are no contaminations from the regular rotational motion. The number of paths can be extracted for both regions, in order to obtained information about the two different regimes, still using Eq. 5.28.

Due to the very statistics collected in the present experiment in the experimental matrices selecting specific configuration (low-K or high-K), the valley fluctuation analysis resulted to be very uncertain. For this reason we concentrated on the ridge fluctuation analysis, as described in Sec. 5.3.

After the fluctuation spectra μ_1 and μ_2 have been built from the COR matrix, 60 keV wide cuts, perpendicular to the diagonal, have been produced, at different energies, in the region from $\sim$ 700 keV to $\sim$ 1000 keV. Examples of this kind of projection as shown in Fig. 5.5, for the total $\gamma - \gamma$ matrix of ^{174}W and for low and high-K spectra. The number of events N_{eve} is extracted considering a window of the COR spectrum along the ridge and 60 keV wide. The values of μ_1 and μ_2 are evaluated in the same way from the fluctuation spectra. The integration is done assuming a linear background under the ridge structure, in order to include contribution coming from the cold regular rotational motion only.

5.2.6 Covariance analysis

Another useful information that can be extracted from the fluctuation analysis is the covariance between pairs of spectra, that gives the degree of "similarity" of two distributions of counts. In general, for two given sets of data X_i and Y_i it is possible to establish if they are populated from the same probability distribution on the base of the correlation coefficient r, defined as

$$r = \frac{\sum_i (X_i - \overline{X})(Y_i - \overline{Y})}{\sqrt{\sum_i (X_i - \overline{X})^2 (Y_i - \overline{Y})^2}} \tag{5.29}$$

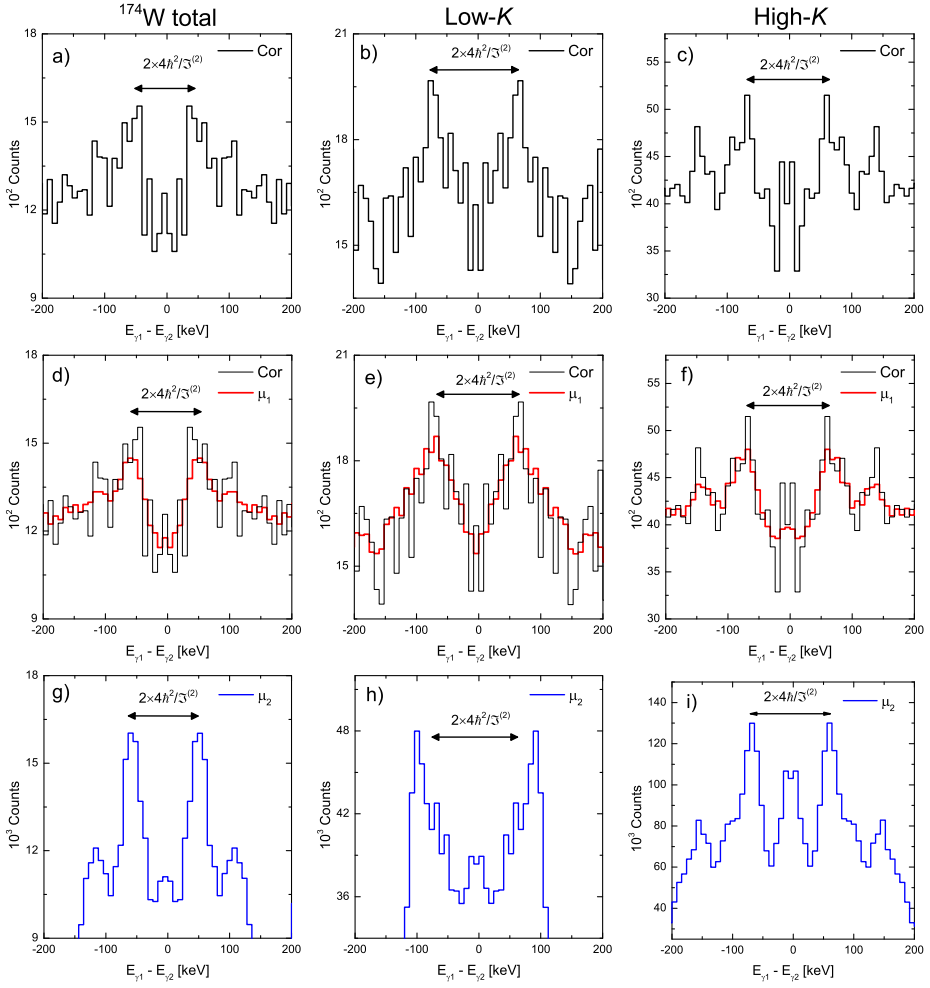

Figure 5.5: Panels a), b) and c): Perpendicular cuts (60 keV wide) of the COR matrix relative to ^{174}W and to low and high-K bands. The corresponding cuts of μ_1 and μ_2 spectra, obtained from the $STATFIT$ code, are reported in panels d) to i). Cuts have been made at $\langle E_\gamma \rangle = 880$ keV for ^{174}W matrix and at $\langle E_\gamma \rangle = 820$ keV in the case of the low-K and high-K spectra.

where the dominator is the product of the variances of the two distributions, while the numerator is the covariance.
The correlation coefficient r is equal to 1 if the sets of data show the same statistical distribution, and is equal to 0 if the two sets of data are completely uncorrelated. Besides these two extreme cases, r gives the degree of correlation between the two data sets. Given two experimental spectra, A and B, the covariance $\mu_{2,cov}(A,B)$ can be calculated as [61]:

$$\mu_{2,cov}(A,B) = \frac{1}{N_{ch}} \sum_j (M_j(A) - \widetilde{M}_j(A))(M_j(B) - \widetilde{M}_j(B)) \tag{5.30}$$

where $M(A)$ and $M(B)$ are the spectra of measured counts, and $\widetilde{M}(A)$, $\widetilde{M}(B)$ are the average distributions obtained from the polynomial interpolation of the spectra, performed by the program $STATFIT$. To normalize the covariance and to have the correlation coefficient r, the following expression is used

$$r(A,B) = \frac{\mu_{2,cov}(A,B)}{(\mu_2(A) - \mu_1(A))(\mu_2(B) - \mu_1(B))} \tag{5.31}$$

The quantities μ_1 and μ_2 are the first and second moment of the fluctuations in the number of counts. From the definition of the covariance the relation between μ_2 and $\mu_{2,cov}$ comes natural, that is $\mu_2(A) = \mu_{2,cov}(A,A)$. The subtraction of the average value of the spectra in the denominator takes into account the spurious fluctuations induced by the background subtraction and gating procedure. In fact, any subtraction performed on a spectrum induces "artificial" fluctuations, of the order of the number of counts in the original spectrum. These fluctuations have no physical meaning and are in general negligible with respect to the real fluctuations related to the presence of a finite number of paths in the nuclear decay. The real fluctuations are proportional to the square of the number of counts.
The covariance $\mu_{2,cov}$ is obtained from the experimental 2D spectra with a similar procedure used for the calculation of μ_1 and μ_2 [16, 61].
After some mathematical derivations, one finds that the error on the correlation coefficient is given by

$$\begin{aligned} \mu_2(r(A,B)) = \frac{r^2(A,B)}{N_{ch}} \left[\frac{\mu_1(A)\mu_1(B)}{(\mu_{2,cov}(A,B))^2} \frac{(\mu_1(A))^2}{2(\mu_2(A))^2} \frac{(\mu_1(b))^2}{2(\mu_2(b))^2} \right] + \\ + \frac{1}{4N_{ch}}(1-r^2)^2 + \frac{3}{2N}(1-r)^2 \end{aligned} \tag{5.32}$$

The covariance technique is employed in connection with the study of the validity of the selection rules on the K quantum number as a function of temperature. In fact, pairs of spectra gated by nuclear configurations characterised by high or low values of the K quantum number will be compared in terms of covariance, in order to establish the degree of similarity between the corresponding nuclear states, as explained in Sec. 5.2.6.

5.3 Results of the ridge fluctuation analysis

The fluctuation analysis method has been applied to different $\gamma - \gamma$ matrices representing the total decay flux for the ^{174}W nucleus and structures in coincidence with low-K and high-K bands, separately. These matrices have been built using the procedure described in Sec. 4.4.

5.3.1 Ridge intensity

The first basic information to be extracted from all matrices is the intensity of the ridge structures as a function of $\langle E_\gamma \rangle$. In order to evaluate the ridge intensity, cuts perpendicular to the main diagonal have been done, in the energy region between 750 keV and 950 keV. The width of each cut is $4\hbar^2/\Im^{(2)} = 60$ keV.
The ridge intensity has been calculated according to the relation:

$$I_{ridge,i}(E_\gamma) = \frac{A_{ridge,i}(E_\gamma)}{A_{bgnor,tot}(E_\gamma)} \tag{5.33}$$

being $A_{ridge,i}$ the area of the ridge belonging to the matrix i (low-K, high-K or total matrix) and $A_{bgnor,tot}$ the area of a region $4\hbar^2/\Im^{(2)} \times 4\hbar^2/\Im^{(2)}$ centred around the ridge of the total ^{174}W matrix; in such a window, the nucleus deposits, on average, one count for each cascade.

In order to have values that can be compared with the simulated data (see Chap. 6), that have a full scale of 100%, the ridge intensities obtained using Eq. 5.33 for the low-K and high-K matrices, has been scaled using the percentage intensity of the 552 keV yrast transition ($12^+ \rightarrow 10^+$). Assuming that the 243 keV yrast transition ($4^+ \rightarrow 2^+$) has intensity 100% (this is the strongest γ transition that collect the entire decay flux), the intensity of the 552 keV transition is tabulated

to be 28.7% [5].
As mentioned in Sec. 4.4 gates were put on 243 keV, 349 keV, 433 keV and 498 keV lines to built the total ^{174}W matrix. The 552 keV γ ray has been selected because it is the strongest line that collect the majority of the decay cascade, not used as a gate; in fact, the intensity of gating γ lines is distorted by the gating procedure and can not be used as a scaling factor in this calculation.
Therefore Eq. 5.33 has been modified, for low-K and high-K matrices, as follows

$$I_{ridge,i}(E_\gamma) = \frac{A_{ridge,i}(E_\gamma)}{A_{bgnor,tot}(E_\gamma)} \cdot \frac{A_{552keV,tot}}{A_{552keV,i}} \cdot 28.7\% \tag{5.34}$$

In order to evaluate $A_{552keV,i}$ (and $A_{552keV,tot}$), a mono-dimensional spectrum gated by the 498 keV transition has been obtained from matrix i (and tot). This is done because the 498 keV and 552 keV are consecutive transitions; in this way, considering this projection, the 552 keV populates the first ridge structures, with an intensity not biased by the gating conditions. Then $A_{552keV,i}$ and $A_{552keV,tot}$ have been calculated with a Gaussian fit centred around the 552 keV line of the gated mono-dimensional spectrum after background subtraction.
The results of the analysis of the ridge intensity are shown in Fig. 5.6. The error bars are the propagation of the errors in the evaluation of the different area, included in Eq. 5.34. For each area the error is defined as the quadratic sum of a statistical error, due to the number of counts (defined as $\sqrt{N}$), and a systematic one. The systematic error is due to the arbitrary with one can fit and subtract background in the region of the ridge. For this reason, two different and independent fits have been done, changing the background and the integrating window; the value of the area, that is used to calculate the ridge intensity, is the average of the two independent evaluations while the systematic error is taken as their dispersion.
It is found that the total ridge intensity in the spin region $25 - 40\hbar$ (after subtraction of the strongest transitions) is of the order of 6% of the entire decay flux, with rather similar population of low-K and high-K structures.
Similar values were found in a previous experimental work reported in Ref. [62].

5.3.2 Number of decay paths

In this section the results obtained using the fluctuation analysis method to study the ridge structure are presented. The number of paths in the ridges is measured for

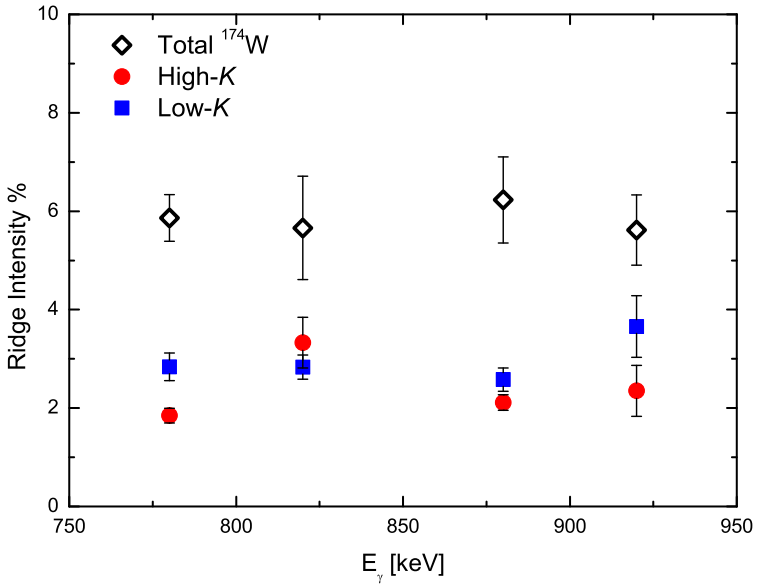

Figure 5.6: Percentage ridge intensity for the total ^{174}W matrix (black) and for the low-K (blue) and high-K matrices (red), obtained using Eq. 5.34.

the different configurations starting from the corresponding gated matrices (total ^{174}W, high-K and low-K).

The matrices used for this analysis are compressed to 4 keV/ch in the case of total ^{174}W and high-K gates, while the low-K one is reduced to 8 keV/ch because of its low statistics. The different binning factors are taken into account using different values of the $\frac{P^{(2)}}{P^{(1)}}$ parameter (see discussion in Sec. 5.1.1).

Results are shown in Fig. 5.7. It is found that the number of unresolved rotational bands for the ^{174}W nucleus is ~ 33, that summed to the four resolved bands, already subtracted (see Sec. 5.2.3) in the energy region $E_\gamma = 750 - -950$ keV, lead to ~ 37 total rotational bands. Furthermore, the analysis indicates that low-K and high-K bands (blue squares and red circles in Fig. 5.7 respectively) are rather equal in number.

The statistical fluctuation analysis of the ridge structures of the ^{174}W nucleus produces results in agreement with a similar work on the normal deformed ^{163}Er nucleus of the rare earth region [4, 16]. In particular, we note that even in the ^{163}Er case a similar number of low-K and high-K structures was observed [4, 16].

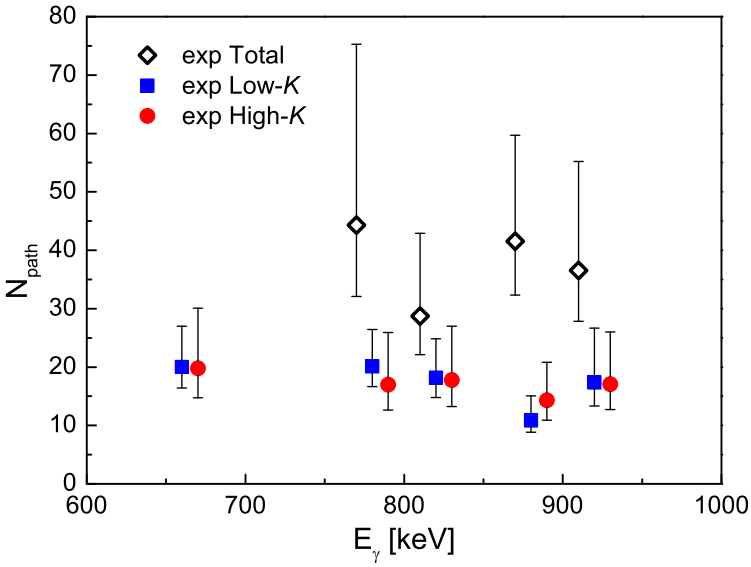

Figure 5.7: The total number of bands for the ^{174}W nucleus (black diamonds) and the number of low-K (blue squares) and high-K bands (red circles), obtained using Eq. 5.28.

Comparison with theoretical values

In addition to these considerations, a comparison with the number of bands predicted by the Cranked Shell Model calculations has been done.
As explained in Chap. 2, with this model it is possible to calculate the energy of each level for a given spin I and the $E2$ decay probability between all the available levels. The decay probability (i.e. the normalised E2 strength function) from level ν_i with spin I to level ν_j with spin $I-2$ is defined as

$$b_{ij} = |\langle \nu_j(I-2)|\nu_i(I)\rangle|^2 \tag{5.35}$$

The number of paths, evaluated experimentally using the statistical fluctuation analysis of the ridge structures, is the average number of rotational bands, defined as a decay path composed by at least two consecutive transitions. The same definition has to be used in order to derive the number of bands from the Cranked Shell Model calculations, to be directly compared to experimental data. The quantity which allows to define the number of discrete bands starting from the calculated microscopic level is the *branching number*

$$n_{b,i} = \frac{1}{\sum_j b_{ij}^2} \tag{5.36}$$

where i is the initial level and j are all the possible final levels. Only transition that are characterised by $n_b < 2$ are considered as "discrete" and can form a discrete rotation bands.
The second important issue is how to discriminate low-K from high-K states, since there is no unambiguous discriminating threshold K_{thr} on the K quantum number. Different values of K_{thr} have been tested against the experimental data, in order to find the most compatible one.

As shown in Fig. 5.8 the total number of bands for the ^{174}W nucleus extracted experimentally agrees with the theoretical calculations. Furthermore, concerning the number of low-K and high-K bands, the best agreement is obtained with $K_{thr} = 6$, for both structures. Using $K_{thr} = 6$ a similar number of low-K and high-K bands is in fact obtained.

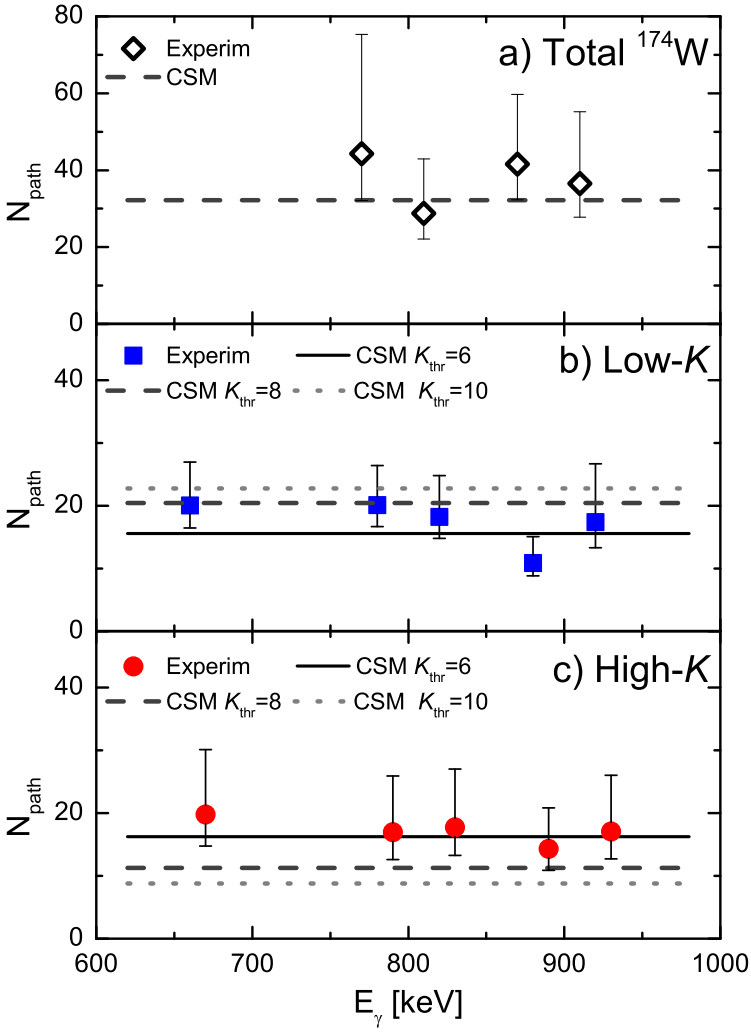

Figure 5.8: Panel a): the total number of bands for the ^{174}W nucleus, obtained from the experiment and CSM calculations. Panel b) and c): the experimental number of low-K (blue squares) and high-K bands (red circles) are compared with CSM calculations, as a function of K_{thr}. The best agreement is obtained with $K_{thr} = 6$, for both structures.

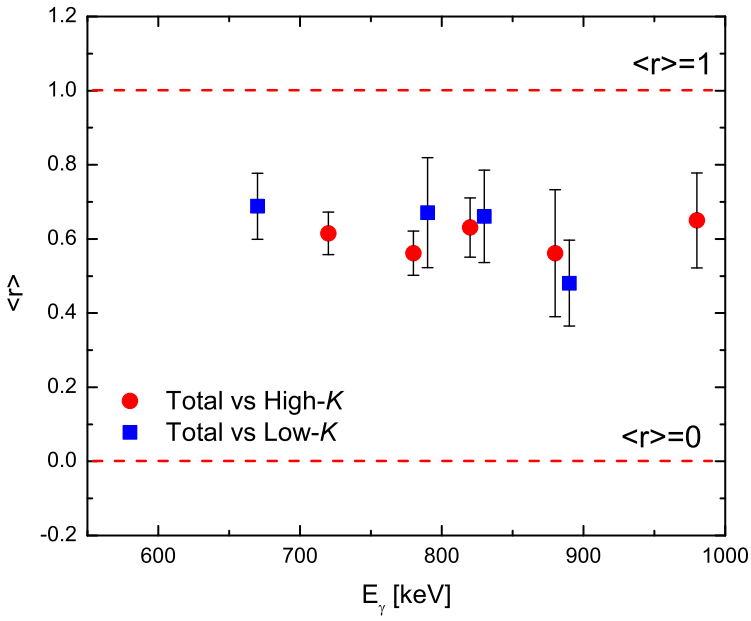

Figure 5.9: Covariance coefficient "Total vs. low-K" (blue squares) and "Total vs. high-K" (red circles), as obtained from the experimental analysis of the ridge structures of ^{174}W.

5.3.3 Covariance between different spectra

In this section a description of the covariance analysis between pairs of $\gamma - \gamma$ matrices gated by different configurations is reported. The analysis is performed only on the ridge structures with the aim of investigating further the properties of the decay flux along discrete bands, in terms of the K quantum number.
Unfortunately, the covariance between low-K and high-K gated matrices could not be estimated because of the limited statistics collected in such matrices, therefore it was impossible to experimentally derive the degree of mixing between the different low-K and high-K configurations.
Instead, in order to study the composition of the decay flux, the covariance coefficients "Total vs. low-K" and "Total vs. high-K" have been evaluated, by applying the procedure described in Sec. 5.2.6 to the total ^{174}W matrix in comparison with low-K and high-K spectra. The result, plotted in Fig. 5.9, shows approximately the same correlation coefficient for both the combinations studied, that is $\sim 60\%$.

This confirms the fact that low-K and high-K structures participate in the same measure to the nuclear de-excitation, as already discussed in connection with the N_{path} evaluation (cfr. Fig. 5.7).

5.4 Study of the rotational planes

Due to the low statistics, only the rotational plane with $N = 1$ (without gating conditions) has been built (see Sec. 1.6.2). It was possible to do only one cuts perpendicular to the main diagonal, 120 keV wide, in order to collect a sufficient number of counts in the ridge structures.

The analysed perpendicular cut of the $N = 1$ rotational plane is shown in Fig. 5.10; the cut has been made at $\langle E_\gamma \rangle = 800$ keV. The valley region of the μ_2 spectrum is not reported because it is affected by large fluctuations not containing physical information but due to low statistics, hence not relevant for this kind of analysis.

The statistical fluctuation analysis has been used to study the ridge structures in order to determine the total number of paths N_{path} at least 3 steps long. Results are shown in Fig. 5.11, and are compared with theoretical values extracted using Cranked Shell Model calculations. It is found that experimental data are in rather good agreement with the theoretical calculations, indicating the existence of approximately 20 discrete rotational bands, at least three steps long.

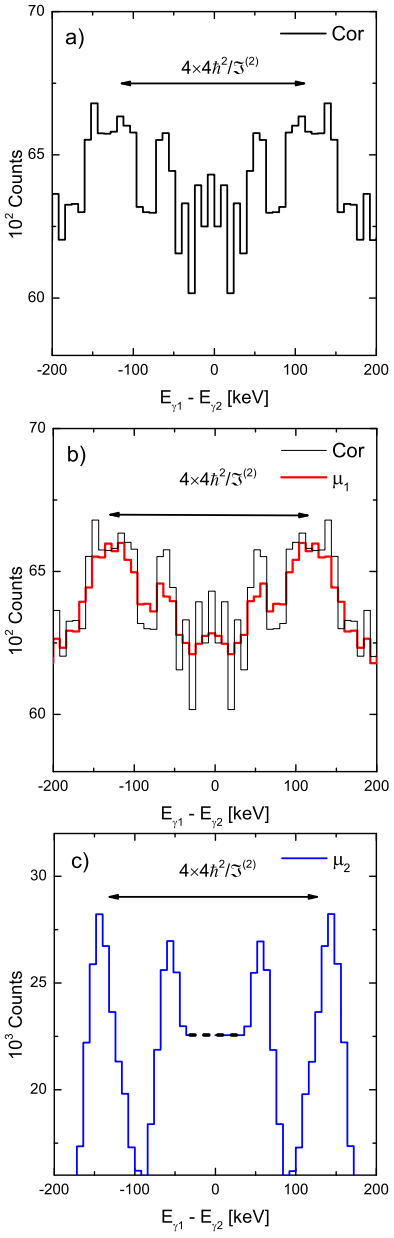

Figure 5.10: Panel a): Perpendicular cuts (120 keV wide) of the COR rotational plane ($N = 1$). The corresponding cuts of μ_1 and μ_2 spectra obtained from the $STATFIT$ code are reported in panels b) and c). Cuts have been made at $\langle E_\gamma \rangle = 800\ keV$.

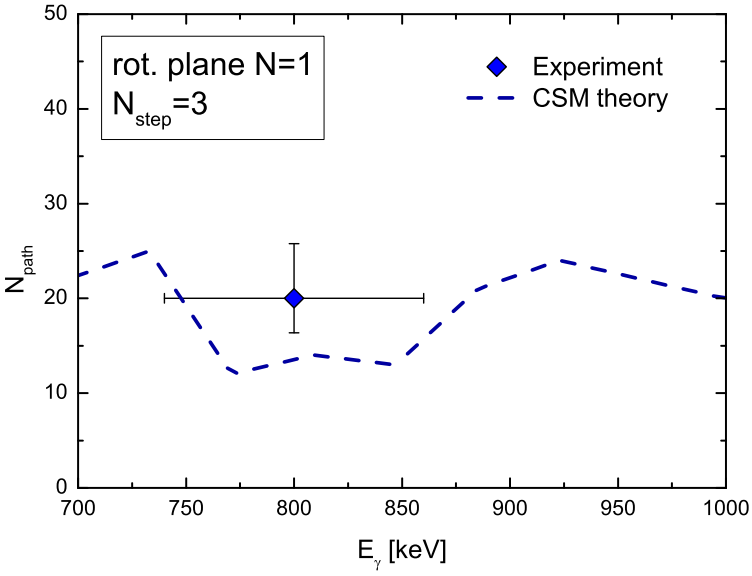

Figure 5.11: Number of paths 3 steps long obtained by applying the fluctuation analysis to the rotational plane (blue diamonds). Results are compared with CSM calculations, here plotted as dashed lines.

Chapter 6

Simulation of the decay flux

Microscopic Cranked Shell Model calculations describe in details the properties of the nuclear rotational motion as a function of temperature, as discussed in Chap. 2. Such calculations are the input of the *MONTESTELLA* code that performs simulations of γ decaying cascades, allowing to have a precise comparison between data and model predictions. In fact, in contrast to schematic simulations, simulations based on microscopic calculations allow to produce γ coincidence spectra which can be analysed by the fluctuation analysis techniques, in the same way as done for experimental data. This makes it possible to perform a more quantitative analysis of the quasi-continuum spectra.
In this Chapter the simulation code *MONTESTELLA* will be described. As already mentioned, it can provide γ decay cascades of nuclei under study, starting from an entry distribution (defined by excitation energy and spin) obtained by the *CASCADE* simulation code [63]. The main output of the simulation consists of γ coincidence spectra which can be directly compared to experimental data.

6.1 Entry distribution

In order to perform the simulation of the compound nucleus decay, it is necessary to know the fusion cross section σ_{fus} of the compound nucleus, as a function of spin I.
This can be calculated by the code *GRAZING* [64], starting from the details of the

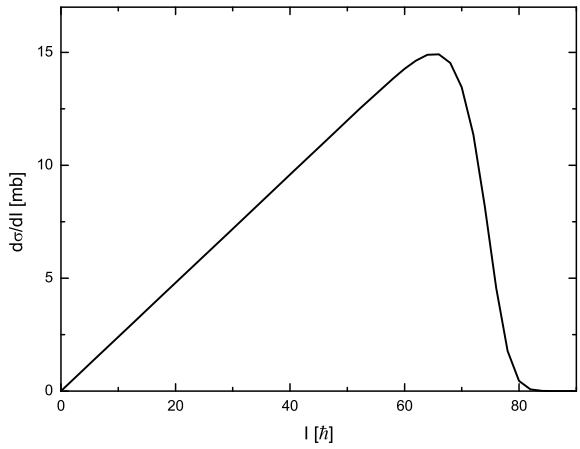

Figure 6.1: Fusion cross section σ_{fus}, obtained with the code *GRAZING*, for the reaction $^{50}Ti +^{128} Te \rightarrow^{178} W^*$ at $E_{beam} = 212\ MeV$

reaction (i.e. target, projectile and beam energy). In this contest it is important to take into account that the reaction happens at lower energy with respect to the beam one, due to energy loss in the target.
In this case, the reaction used is $^{50}Ti +^{128} Te$ at $E_{lab} = 217\ MeV$, corresponding to 5 MeV energy loss in the target. The calculated cross section is represented in Fig. 6.1.

Through the Monte Carlo *CASCADE* code, the compound nucleus decay has been simulated, taking into account the following decay modes:

- electromagnetic radiation;
- protons, neutrons or α-particles evaporation;
- fission.

The crucial point of the simulation is the yrast line, respect to which one calculates the nuclear level density as a function of spin I and excitation energy U. In the simulation used, the yrast line has been calculated using the Lublin - Strasbourg Drop model (see Ref. in [65]) that is equivalent to that calculated by the Cranked

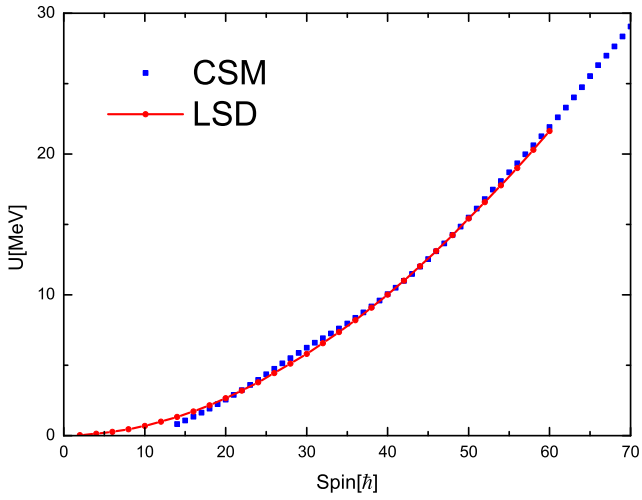

Figure 6.2: Yrast line obtained for the ^{174}W nucleus using the Cranked Shell Model (blue) and the Lublin - Strasbourg Drop model (red) [65]

Shell Model at finite temperature (Fig. 6.2). The LSD yrast line has been calculated from [65] using $T = 3\ MeV$ and *level density* parameter = 0 (that means $A/8.0$). The *CASCADE* code makes a parametrization of the yrast line through the relation:

$$E = \frac{1}{2\theta} \cdot \frac{I(I+1)}{[1 + Def \cdot I^2 + Defs \cdot I^4]} \tag{6.1}$$

where $\theta = 0.01917 \cdot R_0^2 \cdot A^{\frac{5}{3}}$ is the moment of inertia of a spherical rigid body that has radius R_0. Def and $Defs$ are deformation parameters that describe θ variation as a function of spin I, using the liquid drop nuclear description.
Using this code, entry distributions (I, U) have been extracted for the mostly populated residues, namely ^{173}W, ^{174}W and ^{175}W; the bi-dimensional plots and the total projection of these distributions on the spin axis are reported in Fig. 6.3. By integrating these plots it is possible to extract the relative intensity of the three evaporation residues populated during the reaction, as indicated in each plot by labels.

Fig. 6.4 (a)-(e) shows the projections of the ^{174}W nucleus entry distribution for

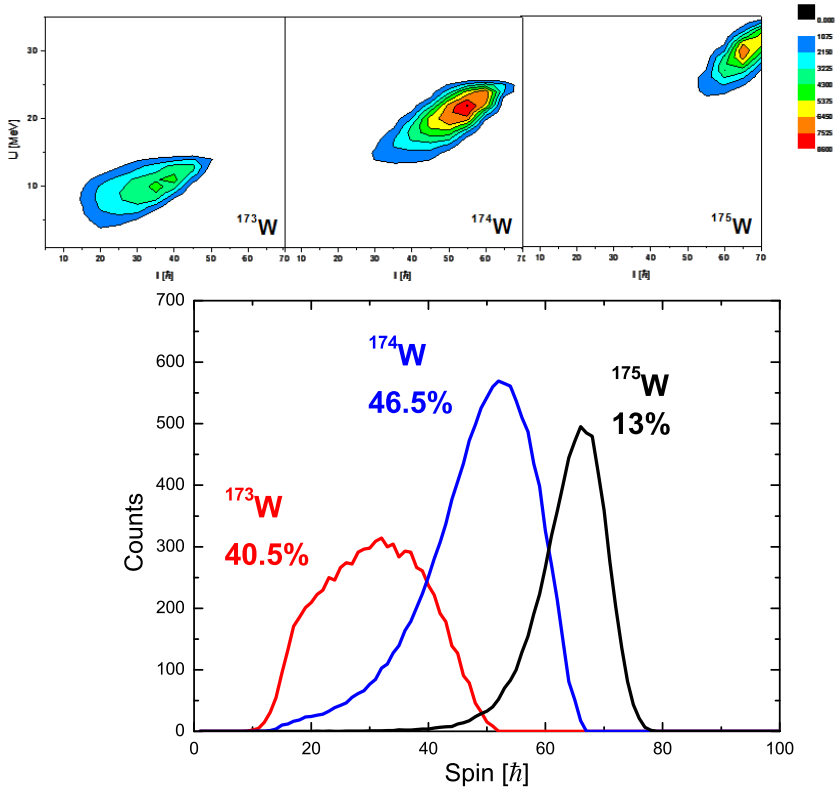

Figure 6.3: Upper panel: entry distributions (I, U) calculated through the *CASCADE* code for the main evaporation residues, populated with the reaction $^{50}Ti +^{128} Te \rightarrow^{178} W^*$ at $E_{beam} = 212\ MeV$. Bottom panel: spin distributions for the three reaction channel ^{173}W, ^{174}W and ^{175}W.

given spin values. In panel (f) the trend of the mean values and FWHM of these projection is summarised, as a function of spin.

In order to compare the relative population of the three evaporation residues with the experimental ones, the same experimental conditions have to be applied to the simulation calculations. As explained in Sec. 4.3. in order to increase the selectivity on ^{174}W, the condition $Fold_{HELENA} \geq 4$ has been set on the scintillators events. Therefore one needs to evaluated the effects given by this requirement on the simulated entry distribution, as explained in the next section.

HELENA response function

First of all the response function of the HELENA multiplicity filter, that is the (F_γ, M_γ) matrix, has been calculated. Here F_γ is the number of gammas detected by the scintillators for an event of multiplicity M_γ. The procedure consists of a combinatorial analysis that allows to extract the probability of detecting F_γ transitions when the nucleus emits M_γ gamma-rays, assuming to have 27 scintillators characterized by $\sim 16\%$ efficiency at 500 keV, 25% of solid angle coverage and 10% of cross talk probability [66].
Once obtained the response function (F_γ, M_γ), projection on the M_γ axis have been done, for fixed values of F_γ. Fig. 6.5 (a) shows the obtained curves and 6.5 (b) the centroids and FWHM of the M_γ distributions as a function of F_γ.

After calculating the response function of the HELENA array it has been possible to correct the entry distribution obtained through the *CASCADE* code for the residues ^{173}W, ^{174}W and ^{175}W. Fig. 6.6 shows the comparison between the entry distributions before (dashed lines) and after (solid lines) applying the HELENA response function and selecting the condition $Fold_{HELENA} \geq 4$. The percentage population of the three residues has been calculated and compared with experimental ones.

In Fig. 6.7, as one can notice, after setting the HELENA fold condition ^{174}W and ^{175}W are favoured with respect to ^{173}W, also observed in the data. In the case of the experiment, the relative population has been extracted from the intensity of the discrete lines observed in the data (cfr. Fig. 4.17, 4.18 and 4.19). Such transitions are representative of the decay flux of each nucleus, therefore their intensity can be

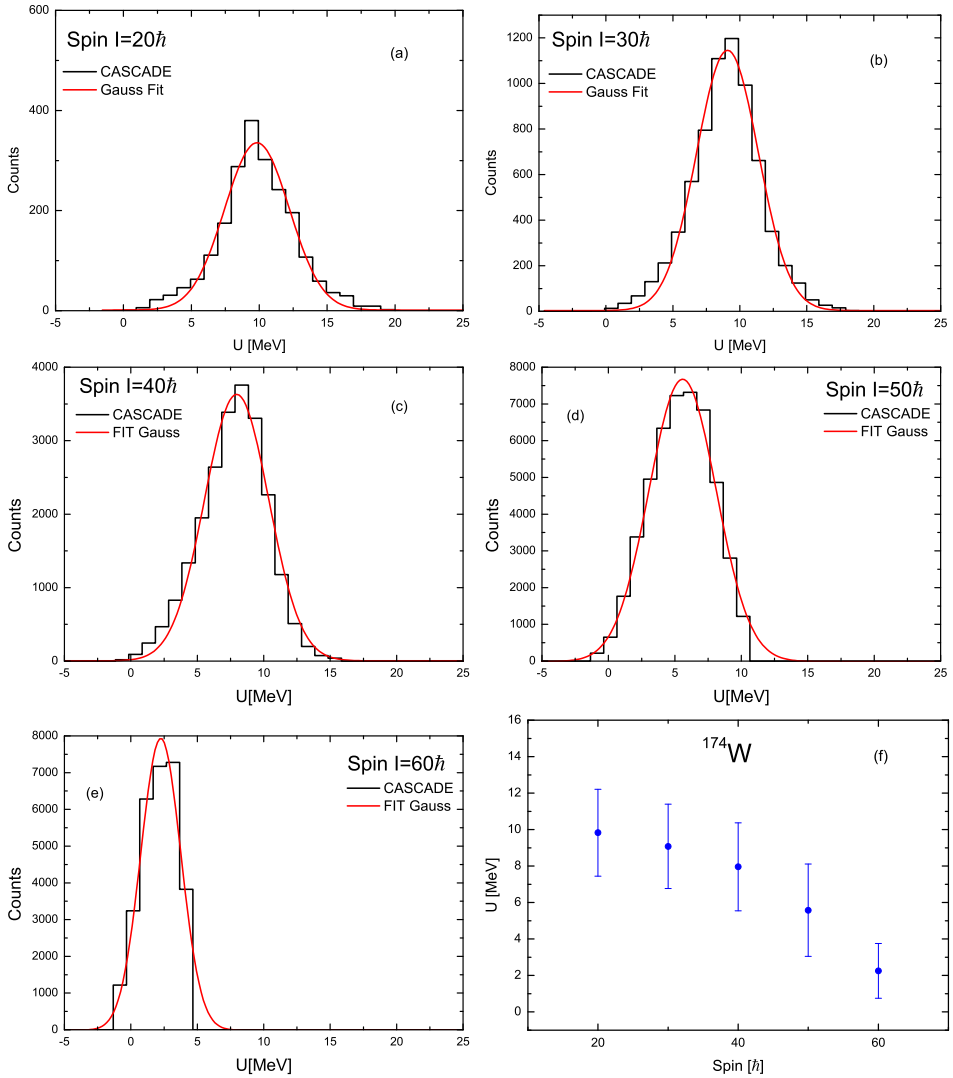

Figure 6.4: Panels (a)-(e) show the ^{174}W nucleus entry distribution for the spin values 20, 30, 40, 50 and 60$\hbar$. Red curves represent Gaussian fits used to extract centroids and FWHM parameters. Centroids position and corresponding error bars (calculated as $\sigma = FWHM/2.35$), are plotted as a function of spin in panel (f).

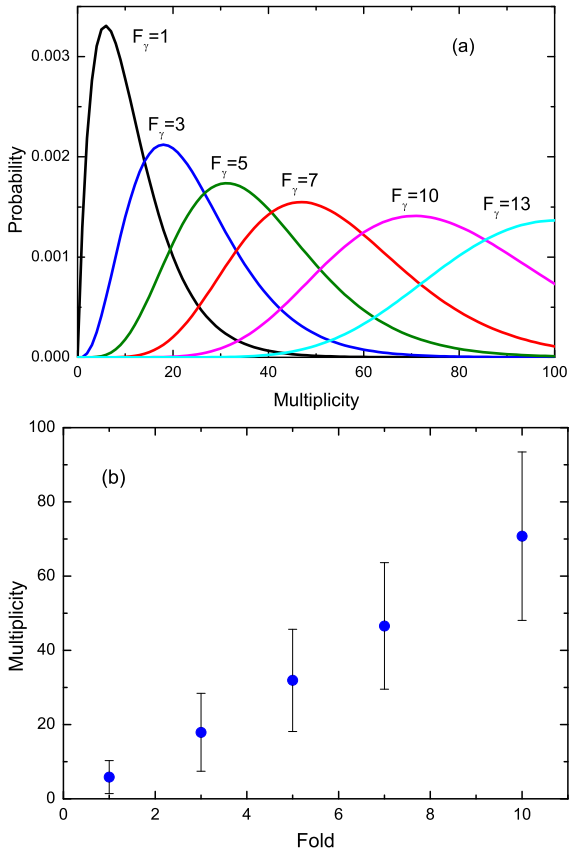

Figure 6.5: (a) M_γ distributions for different values of F_γ. (b) centroids and FWHM of the M_γ distributions as a function of F_γ.

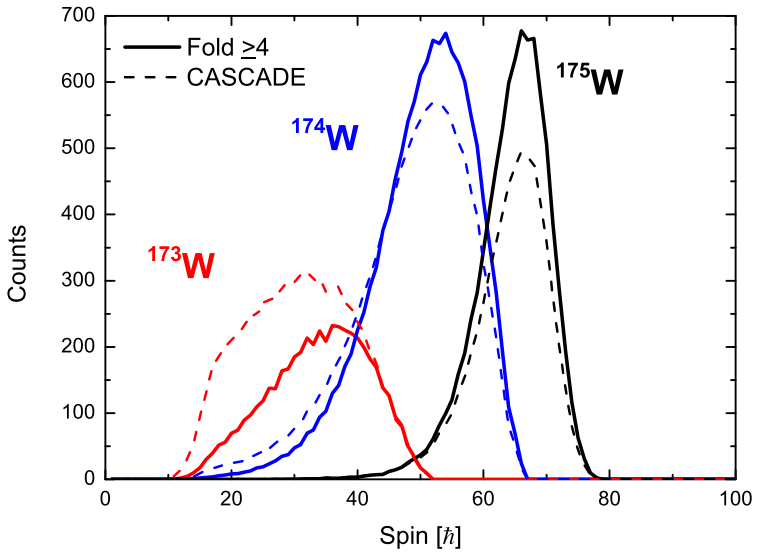

Figure 6.6: Comparison between entry spin distributions of the ^{173}W, ^{174}W and ^{175}W residues before (dashed lines) and after (solid lines) applying the experimental conditions.

used, as a first approximation, to evaluate the relative population of the reaction channels.

6.2 General structure of the *MONTESTELLA* code

The *MONTESTELLA* program performs simulations of the γ decay of rotational nuclei produced trough heavy ions fusion-evaporation reactions. Using this program, it is possible to build mono-dimensional γ-spectra and bi-dimensional $\gamma - \gamma$ matrices, that can be analysed using the same techniques employed with experimental spectra.

Microscopic Cranked Shell Model calculations, described in Chap. 2, are the input of the simulation; they provide information on nuclear energy levels and E2 decay probability.

The nucleus, starting from the excited state in which it is created, has a finite number of decay paths for its de-excitation until the yrast line has been reached.

The fundamental points on which the simulation code is based are:

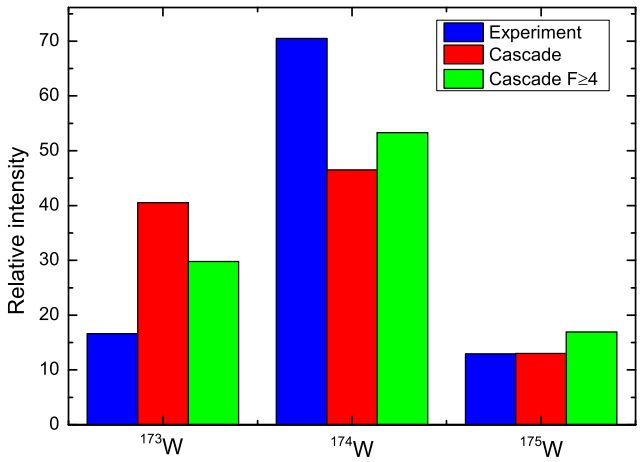

Figure 6.7: Comparison between the relative population of ^{173}W, ^{174}W and ^{175}W residues extracted from experimental data (blue) and using *CASCADE* simulation code, before (red) and after (green) applying the experimental conditions $Fold_{HELENA} \geq 4$. Experimental data are obtained integrating the curves in Fig. 4.21.

1. the starting level of the γ-cascade is randomly selected from an initial distribution of excitation energy as a function of spin, given by the *CASCADE* code (Fig. 6.3);

2. the decay mode is determined through the competition between E1 and E2 γ-transitions;

3. a final level is determined after the E1/E2 decay.

Points 2 and 3 are repeated until the yrast line has been reached.

6.2.1 Entry region

The entry region, defined by the spin $I[\hbar]$ and the excitation energy $U[MeV]$, is provided by the *CASCADE* simulation code. In particular, the spin distribution is given as an external data file that contains all points of the *CASCADE* distribution, while the excitation energy entry region is taken from a Gaussian distribution that has centroid $\langle U \rangle$ and sigma σ, as calculated from the *CASCADE* code in spin interval $40 - 60\hbar$ (see Fig. 6.4 (f)). The values used are $\langle U \rangle = 5.5\ MeV$ and $FWHM = 2.35 \cdot \sigma = 4.7\ MeV$.
Using Monte Carlo techniques, starting from these distributions, (I, U) events are produced and used as the starting point of the γ-cascade.
The number of events initially generated has to be large enough to have a valid statistical distribution, that is, in this case, $2 \cdot 10^5$ events.

6.2.2 Level scheme

In order to simulate the γ-decay of the ^{174}W nucleus, the rotational levels in the spin region from spin $14\hbar$ to $70\hbar$ and in the internal energy region from 0 to $\sim 3\ MeV$ have been microscopically defined according to the model described in Chap. 2. For each level, information on the K-quantum number are given in addition to spin, energy and parity.
The value of K assigned to each level i has been obtained through the expectation value of $\widehat{J}_z^2$:

$$K_i = \sqrt{\langle i | \widehat{J}_z^2 | i \rangle} \tag{6.2}$$

Actually, to each level not a single K value is associated but a gaussian distribution centred around K_i and characterized with a width σ_K that is:

$$\sigma^2(K^2) = \overline{\langle i|\widehat{J}_z^2|i\rangle^2} - \overline{\langle i|\widehat{J}_z^2|i\rangle}^2 \tag{6.3}$$

Each level i is given with an E2 decay probability $b_j = |\langle i(I)|j(I-2)\rangle|^2$ between the state i and all the states j with spin $(I-2)$ extracted from Cranked Shell Model calculation.
For energies higher then the last calculated level at each spin ($U_{band} \sim 2-2.5\ MeV$, as reported in Fig. 2.11) no more microscopic values are available, therefore a continuous distribution of states is used, with properties extrapolated from the lower energy levels. In particular, it is assumed that the decay follows a continuum distribution of states: here the E2 decay probability is characterized by a Gaussian shape, with a full width half maximum Γ_{rot} extrapolated from the discrete-levels region.

6.2.3 Level density

In the discrete band region ($U < 2-2.5\ MeV$) the level density corresponds to the effective density of microscopic levels. For each value of excitation energy over the yrast line U, levels $n(U)$ contained in an interval $\Delta U = 10\ keV$ around U are counted and the level density id obtained as:

$$\rho(U) = n(U)/\Delta U \tag{6.4}$$

In the damping region ($U > 2-2.5\ MeV$) the level density $\rho(U)$ of the calculated nuclear states is fitted as a function of the internal energy U at each spin, using the following function, based on a Fermi gas model

$$\rho(U) = \frac{\sqrt{\pi}}{48}\frac{e^{2\sqrt{aU}}}{a^{1/4}U^{5/4}} \tag{6.5}$$

a is the Fermi parameter that, according to CSM, depends on the spin I and is plotted in Fig. 6.8(a). The level density as a function of excitation energy U, for a given spin ($I = 40\hbar$) is shown in Fig. 6.8(b); here symbols refer to discrete levels of positive and negative parity while the line is obtained using the Fermi gas function in Eq. 6.5.

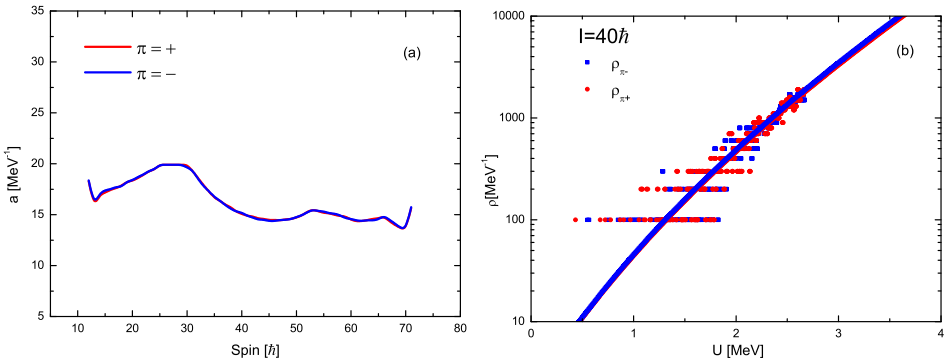

Figure 6.8: (a) Level density Fermi parameter as a function of spin. (b) Level density as a function of excitation energy U, for a given spin ($I = 40\hbar$); symbols refer to discrete levels of positive and negative parity, while the line is obtained using the Fermi gas function of Eq. 6.5.

6.2.4 Transition probability

The *MONTESTELLA* program is based on the competition between transition with multipolarity E1 and E2, that dominate the decay of rotational nuclei. E2 transitions contain information about nuclear rotational features and imply changes in two unit of angular momentum along a specific rotational band, preserving parity. Electric dipole transitions E1, on the other hand, reduce the nuclear excitation energy, inducing a change of parity and spin ($\Delta I = 0, \pm 1\hbar$), allowing to populate different rotational bands.
The possible decay modes are:

- E1 decay in the "band" region;
- E2 decay in the "band" region;
- E1 decay in the "damp" region;
- E2 decay in the "damp" region.

where "band" and "damp" refer to the the region of microscopically calculated levels and above, respectively.

Let's consider the E1 decay probability in the "band" region, called $T_{band}(E1)$. In the "band" region, energy, spin, parity and K-distribution are known for each spin. The E1 transition probability from an initial state of energy U_i, spin I and with a K distribution centred around K_i (σ_i wide) is given by:

$$T_{band}(E1, U_i) = \sum_{Uf} w_{E1}(U_i - U_f) \cdot P_{\Delta K}(K_i, K_f) \tag{6.6}$$

where

$$P_{\Delta K}(K_i, K_f) = \int\int dK_1 dK_2 \; e^{\frac{(K_1-K_i)^2}{2\sigma_i^2}} \; e^{\frac{(K_2-K_f)^2}{2\sigma_f^2}} \; e^{-\frac{|K_1-K_2|}{\sigma}} \tag{6.7}$$

This term reduces the transition probability between states that have different K distributions [4]. The last exponential factor in Eq. 6.7 allows to introduce the same behaviour observed experimentally for discrete isomeric levels [10]. In particular, it hinders the decay of high-K states to yrast states characterized by very different K distributions. The $w_{E1}(U_i - U_f)$ is given by:

$$w_{E1}(U_i - U_f) = C \cdot f_{GDR}(U_i - U_f) \cdot \frac{(U_i - U_f)^3}{\rho(U_i)} \tag{6.8}$$

being f_{GDR} the tail of the Giant Dipole Resonance strength function that has a Lorentzian shape. It is supposed that $f_{GDR}(U)$ is spin independent and depends on the excitation energy above the yrast line, as follows:

$$f_{GDR}(U) = \sum_{i=1}^{3} \frac{\Gamma_R U}{(U^2 - U_{R,i}^2)^2 + (\Gamma_R U)^2} \tag{6.9}$$

being $U_{R,i}$ the energy of the component of the strength function of the GDR along the $i-th$ axis, and Γ_R the width of such component.
The constant C in Eq. 6.8 depends only on quantities typical of the nucleus under analysis and it is introduced in order to satisfy the energy weighted sum rule. It is defined as

$$C = \frac{1}{\hbar} \; \frac{4}{3\pi} \; \frac{e^2}{\hbar c^2} \; \frac{1}{m_p c^2} \; \frac{NZ}{A} \tag{6.10}$$

Previous studies showed that to reproduce the intensity of the experimental discrete bands at low energies the E1 transition probability needs to be reduced by a factor $h_{1n} < 1$, known as hindrance factor.

$$T_{eff}(E1, U_i) = h_{1n} \cdot T(E1, U_i) \tag{6.11}$$

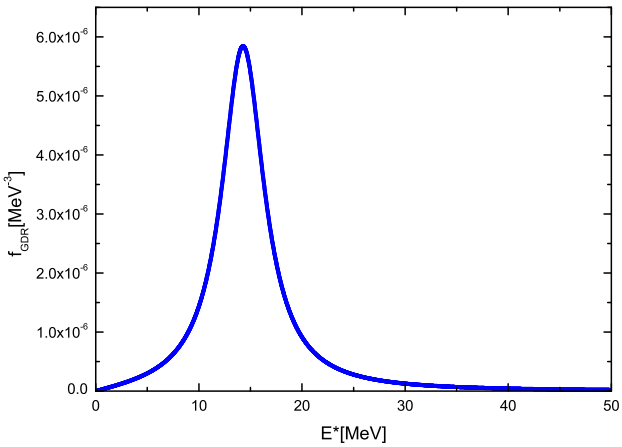

Figure 6.9: Lorentzian curve of the Giant Dipole Resonance strength function, relative to the ^{174}W nucleus. The distribution is centred around 14 MeV with a FWHM of ~ 5 MeV.

In the "damp" region ($U > 2 - 2.5$ MeV), since there are no discrete levels defined, the E1 transition probability is calculated starting from an excitation energy U_i, by the relation

$$T_{damp}(E1, U_i) = \int_0^{U_i} w_{E1}(U_i - U)\rho(U)dU \tag{6.12}$$

with

$$w_{E1}(U_f - U) = C \cdot f_{GDR}(U_i - U) \cdot \frac{(U_i - U)^3}{\rho(U_i)} \tag{6.13}$$

Here f_{GDR} and C have the same expression reported in Eq. 6.9 and Eq. 6.10. Even in this case the calculated transition probability is multiplied by an hindrance factor h_{1n}, as done in Eq. 6.11.

The E2 transition probability as a function of energy U_i is given by the relation

$$T(E2, U_i) = \int w_{E2}(U_i - U)dU \tag{6.14}$$

where

$$w_{E2}(U_i - U) = \frac{12\pi}{225} \frac{e^2}{(\hbar e)^5} \frac{E_\gamma^5}{\hbar} B(E2, E_\gamma) \tag{6.15}$$

with

$$B(E2, E_\gamma) = B_0 \frac{2}{\sqrt{2\pi\sigma^2}} \cdot e^{\frac{(E_\gamma - \langle E_\gamma \rangle)^2}{2\sigma^2}} \tag{6.16}$$

In the previous expression the value of B_0 is related to the static nuclear deformation, and it is expressed in Weisskopf units. In our case B_0 is 140 *W.u.* [67]. The mean value $\langle E_\gamma \rangle$ and the corresponding standard deviation are calculated through all possible transitions between spin I and $I-2$ for states of the band region, while in the damping region such values are independent on spin, and are obtained as an average over the corresponding quantities from discrete levels. Eq. 6.16 assumes different formulations depending whether the corresponding E_γ transition lies in the band or damping region, namely:

$$B(E2, E_\gamma) = \begin{cases} b_j, & \text{in the band region} \\ B_0 \frac{2}{\sqrt{2\pi\sigma_{rot}^2}} e^{\frac{(E_\gamma - \langle E_\gamma \rangle)^2}{2\sigma_{rot}^2}}, & \text{in the damping region} \end{cases} \tag{6.17}$$

where b_j is the decay probability from state at spin I to all states at spin $I-2$ with $j = 1, \ .., \ 1000$. These decay probabilities are calculated using the Cranked Shell Model formalism (see Sec. 6.2.2). In the damping region the E2 decay probability has a Gaussian shape with a full width half maximum given by Γ_{rot}, that is related to σ_{rot} by the relation $\Gamma_{rot} = 2.35 \cdot \sigma_{rot}$.

Given the transition probability $T(E1, U)$ and $T(E2, U)$, the total decay probability from the state (I, U_i) through a dipole or a quadrupole transition is

$$T_{tot}(U_i) = T(E1, U_i) + T(E2, U_i) \tag{6.18}$$

The decay mode is selected via a MonteCarlo using as E1 and E2 probabilities the ratios:

$$P(E1, U_i) = \frac{T(E1, U_i)}{T_{tot}(U_i)} \quad \text{and} \quad P(E2, U_i) = \frac{T(E2, U_i)}{T_{tot}(U_i)} \tag{6.19}$$

The energy of the γ transition and the final state to which the nucleus decays through the decay mode are determined using the parametrizations $w_{E1}(E_\gamma)$ and $w_{E2}(E_\gamma)$. If one has an E1 decay, using a Monte Carlo procedure the spin change ΔI ($\Delta I = 0, \pm 1 \ \hbar$) given by the transition is determined, while afterwards the

final state is chosen among all possible states with the correct spin and opposite parity respect to the initial level. If an E2 decay is chosen, the γ transition keeps the nucleus in the same nuclear configuration (same signature and parity) with a $\Delta I = 2\hbar$ change of spin unit.

6.2.5 Study of the $P_{\Delta K}(K_i, K_f)$ integral

The effects on K-hindrance given by the $P_{\Delta K}(K_i, K_f)$ integral, reported in Eq. 6.7, have been investigated. To do this, the value of $P_{\Delta K}$ has been plotted as a function of $\Delta K = K_i - K_f$ using different values of the σ parameter, which regulates the E1 decay hindrance.
As a multiplicative factor, $P_{\Delta K}$ has two extreme values: 0 (full-hindrance) and 1 (no-hindrance). Different cases between these two limits have been studied using $\sigma = 0.3,\ 2.5,\ 10,\ 100$ and 500. Fig. 6.10 shows the trend of the $P_{\Delta K}(K_i, K_f)$ integral as a function of the difference ΔK, for different σ_i, σ_f parameter combination.
As one can notice, in case of well-separated K distribution, that corresponds to small value of σ_i, σ_f (e.g. $\sigma_i = \sigma_f = 2$), the $P_{\Delta K}(K_i, K_f)$ function rapidly decreases with increasing ΔK. On the contrary, if the K distributions have a large overlap (e.g. $\sigma_i = \sigma_f = 6$), the slop of the curve diminishes. This behaviour is more evident in the case of strong hindrance ($\sigma = 0.3$ or 2.5) and becomes weaker when the hindrance condition is more relaxed. Furthermore, it can be observed that as σ increases, the $P_{\Delta K}(K_i, K_f)$ integral gradually goes to 1.
The value of σ used to perform the simulation is 0.3, that is the value found in literature [1].

6.3 Parameters of the simulation

In order to reproduce the experimental decay flow of ^{174}W a number of input parameters need to be adjusted before running the simulation *MONTESTELLA*: the most important one is the hindrance factor h_{1n} for the E1 decay. The adjustment of the hindrance factor is based on the reproduction of the intensity of the yrast band and of the first ridge, as observed in a $\gamma - \gamma$ coincidence matrix [29].

First of all, the yrast intensity extracted from experimental data has been compared to the simulated values, using different values of h_{1n}. As one can see in

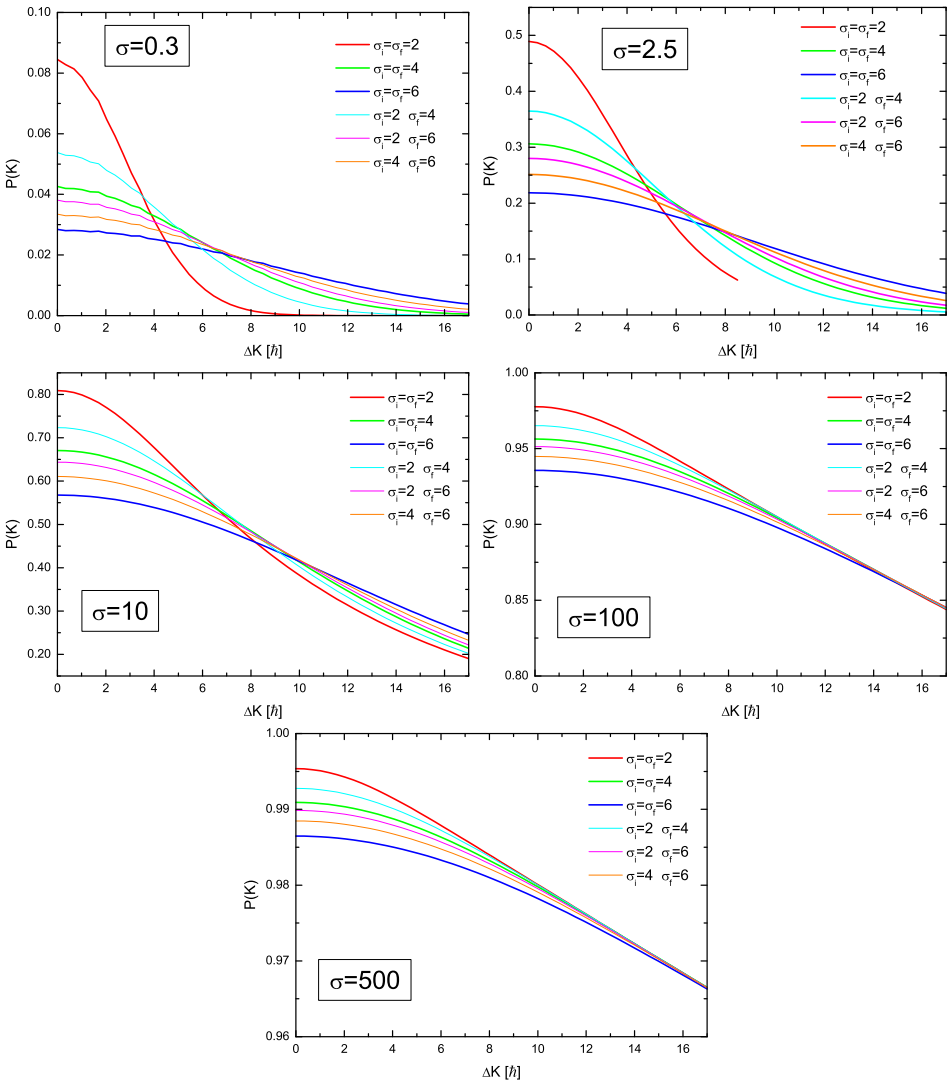

Figure 6.10: Values of the $P_{\Delta K}(K_i, K_f)$ integral for different values of the σ parameter; in each panel, each curve is associated to different width σ_i and σ_f of the initial and final K distribution.

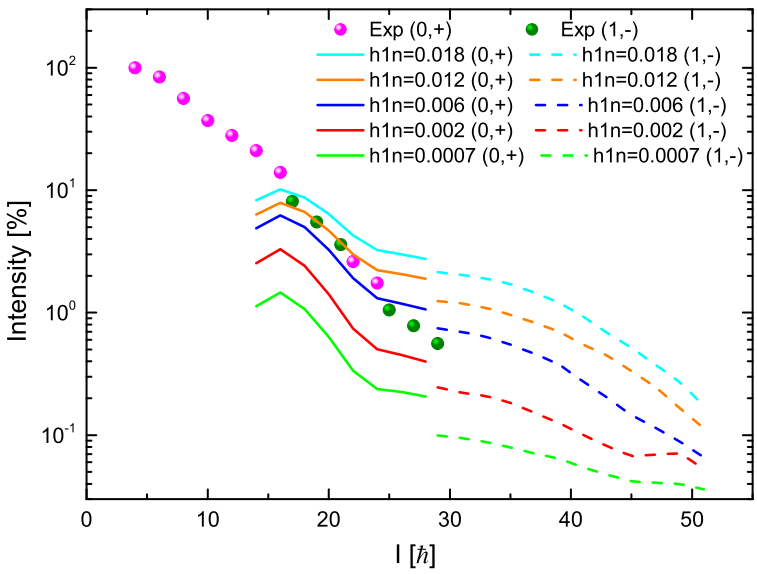

Figure 6.11: Comparison between yrast population intensities extracted from experimental data and simulations using different values of h_{1n}. As one can see, the best agreement is reached using $h_{1n} = 0.012$.

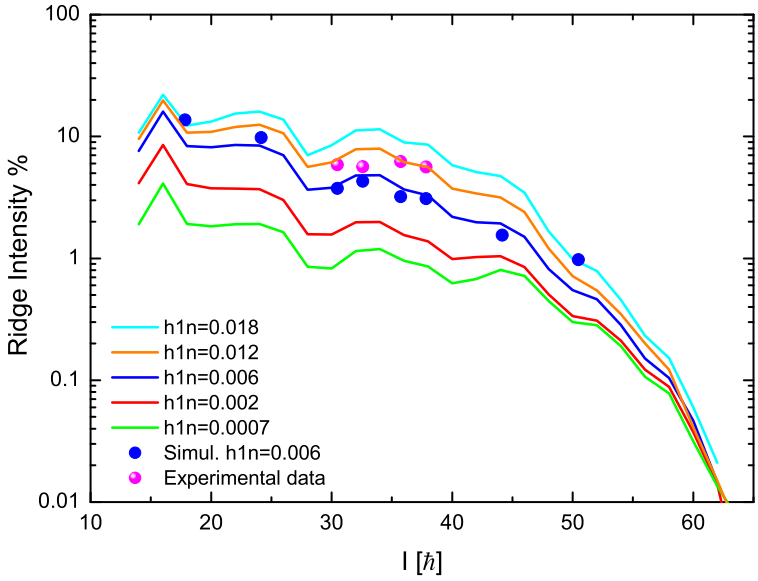

Figure 6.12: Comparison between the intensity of the first ridge extracted from experimental data and the one obtained with the *MONTESTELLA* simulation using different values of h_{1n}. Lines correspond to the intensity obtained by summing over the population of the discrete excited bands, blue symbols refer to values extracted from the analysis of simulated $\gamma - \gamma$ matrices. Best agreement is obtained using the E1 hindrance factor $h_{1n} = 0.012$.

Fig. 6.11, the best agreement is reached using $h_{1n} = 0.012$, even considering the extrapolation of the experimental data points towards high spin.
The second quantity used to set the h_{1n} hindrance factor is the intensity of the first ridge of the total $\gamma - \gamma$ matrix. The ridge intensity obtained from the *MONTESTELLA* simulation has been calculated using two independent methods: i) by analysing the ridge structures observed in the simulated $\gamma - \gamma$ matrices (blue points in Fig. 6.12), using a procedure similar to the one adopted for experimental data (see Sec. 5.3.1) and ii) by integrating the intensity population of the discrete excited bands (defined by the branching condition $n_b < 2$) followed by the γ cascade (line plots in Fig. 6.12). As shown in Fig. 6.12, $h_{1n} = 0.012$ is, even in this case, in best agreement with the experimental data, here plot with pink circles.

The parameters used to run the *MONTESTELLA* simulation code are reported

$\langle U \rangle$	$FWHM_U$	h_{1n}	$B(E2)_{nor}$
5.5 MeV	4.7 MeV	0.012	140 W.u.

Table 6.1: Optimal parameters used to run the *MONTESTELLA* simulation code.

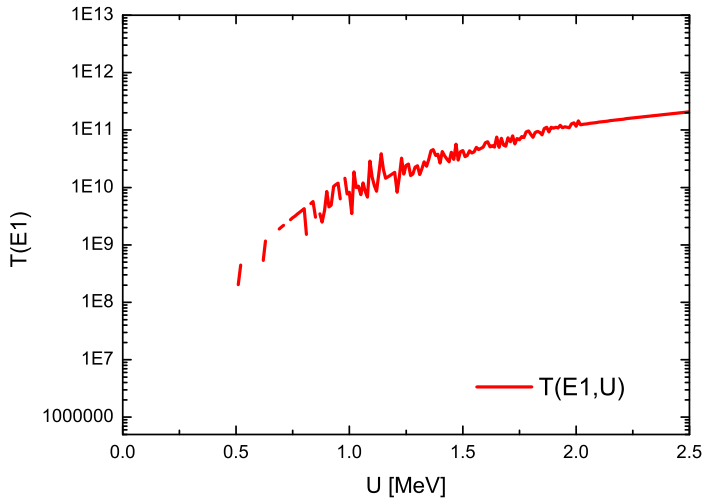

Figure 6.13: $T(E1, U_i)$ trend without the K quantum number dependence.

in Tab. 6.1. $B(E2)_{nor}$ is the strength of the E2 decay and it is taken from Ref. [68].

6.4 *K* dependence of statistical decay probability

Once the best parameters for the γ decay flow have been determined, the K quantum number dependence of the statistical decay probability has been investigated. The E1 decay probability, regardless of the K dependence, can be calculated following Eq. 6.11. Such a $T(E1, U_i)$ trend is shown in Fig. 6.13.

As discussed in Sec. 6.2.4, by taking into account the K quantum number dependence, the E1 decay probability, in the band region, becomes

$$T_{band}(E1, U_i) = \sum_{Uf} w_{E1}(U_i - U_f) \cdot P_{\Delta K}(K_i, K_f) \tag{6.20}$$

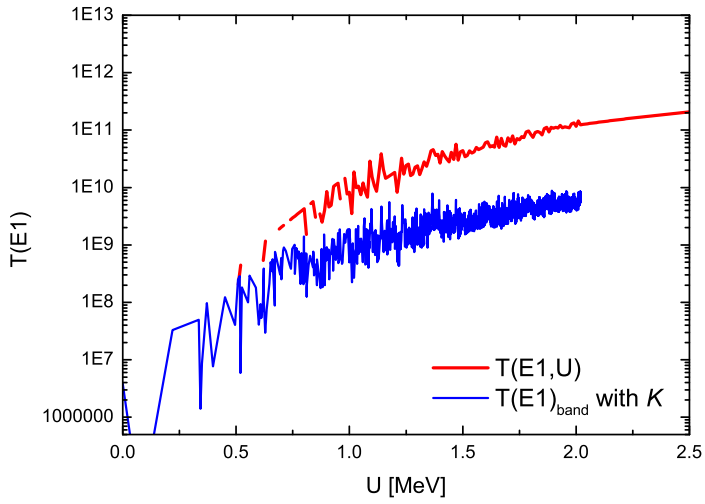

Figure 6.14: Comparison between the E1 decay probability $T(E1, U_i)$ (red) and $T_{band}(E1, U_i)$ (blue) with the same hindrance factor $h_{1n} = 0.012$.

where the hindrance factor $P_{\Delta K}(K_i, K_f)$, given by Eq. 6.7, is a number smaller than 1. As a consequence, the $T_{band}(E1, U_i)$ probability becomes smaller compared to the $T(E1, U_i)$ corresponding expression, regardless of K, reported in Fig. 6.14. This implies that the number of statistical decays is reduced, therefore the hindrance factor h_{1n}, used in the discrete band region, has to be modified in order to reproduce the experimental conditions. It is found that by multiplying h_{1n} by a factor of 18, the $T_{band}(E1, U_i)$ probability becomes very close to the original $T(E1, U_i)$, as reported in Fig. 6.15.

The final h_{1n} value, used for the T(E1) probability is $h_{1n} = 0.012 \cdot 16 = 0.192$.

6.5 Average properties of the simulated decay flux

The average properties of the simulated decay flux of ^{174}W have been investigated. Fig. 6.16 shows the average γ decay flux in the U vs $Spin$ plane. The dashed blue line (Fig. 6.16) indicates the excitation energy region where microscopic levels are available. It is seen that the majority of the γ decay flux at $I \geq 40\hbar$ runs in

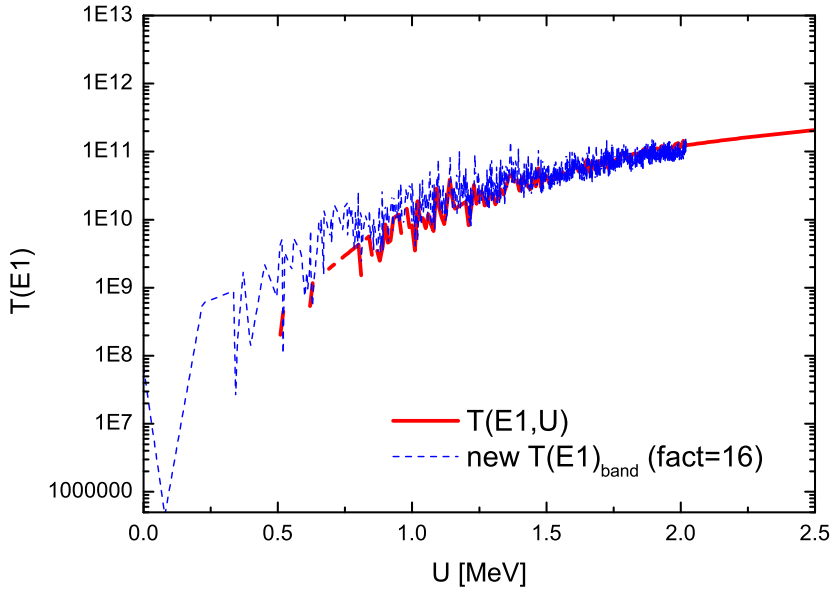

Figure 6.15: Comparison between the E1 decay probability $T(E1, U_i)$ (red) and $T_{band}(E1, U_i)$ (blue) after changing the h_{1n} hindrance by a factor of 16, in order to take into account the dependence on the K quantum number (see text for details).

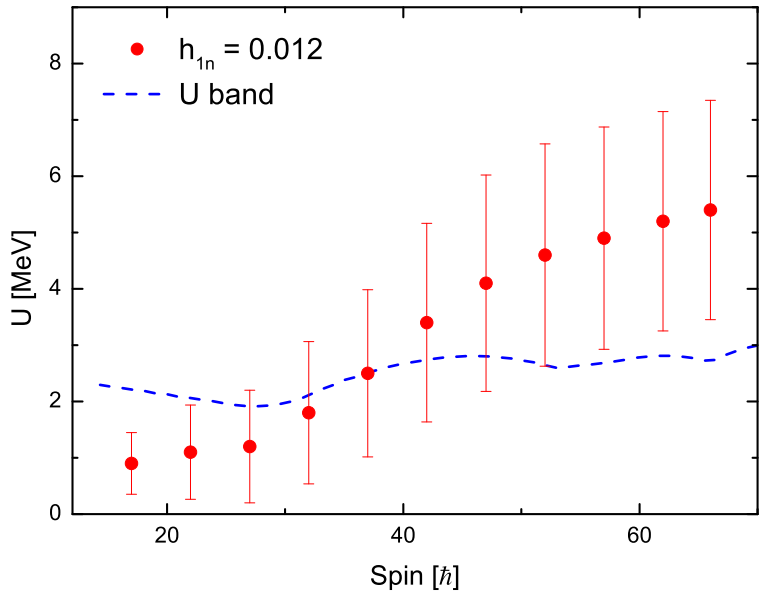

Figure 6.16: γ decay flux expressed as internal energy $U[MeV]$, as a function of spin. The discrete bands region is delimited by the dashed blue line.

the damping region, characterised by highly mixing rotational bands, not treated microscopically in the present simulation. In the spin region $I = 10-40\hbar$ the decay flux covers instead the microscopically calculated region, allowing for a detailed investigation of nuclear structure properties with fluctuation analysis techniques.

In addition to the intensity of the yrast band, used to determined the hindrance factor for the E1 decay, the population of the first excited bands for low-K and high-K configuration has been compared with experimental data. On the left panel of Fig. 6.17, the simulated intensity of the two strongest low-K excited bands is compared with the experimental ones; the agreement is rather good although in the high spin region no experimental data are available. On the right panel of Fig. 6.17 the same comparison is presented for high-K bands. The intensities of bands with the same K value are summed. Even in this case the simulated data are in agreement with the one extracted by the experimental analysis. Intensity values that refer to experiment are taken from Ref. [5].

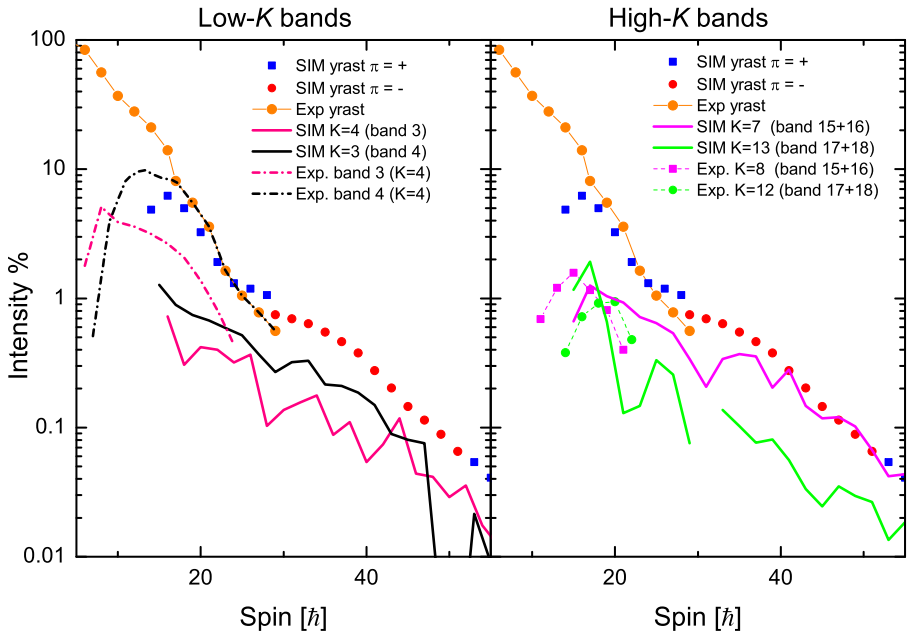

Figure 6.17: Comparison between experimental and simulated intensity population for the strongest low-K (left) and high-K (right) excited bands. The intensity plotted for high-K structures are the sum of two bands with the same K value.

6.6 Analysis of the simulated spectra

The *MONTESTELLA* simulation code is able to produce $\gamma - \gamma$ matrices similar to the experimental ones, to be analysed with analogous tecniques as described in Chap. 5. In particular, a direct comparison between experimental and simulated data is performed, in terms of number of paths. This is in fact one of the most significant quantities for the understanding of the rotational motion at finite temperature.

6.6.1 Number of paths

First of all, a total $\gamma - \gamma$ matrix has been produced by the code *MONTESTELLA*. The same analysis to extract the number of decay paths has been performed as for the experimental matrices. For this reason the most intense discrete lines have been subtracted, in order to ensure a proper evaluation of the count fluctuations [8]. In particular, while all known transitions from the level scheme have been removed from the experimental matrices (see Sec. 5.2.3), as a first approximation only the yrast band has been subtracted from the simulated spectra for each spin-parity configuration, since these are the most intensely populated transitions. The obtained matrix is shown in Fig. 6.18. The statistical fluctuation analysis was then applied. Cuts at $\langle E_\gamma \rangle = 880\ keV$ of the COR, μ_1 and μ_2 simulated matrices relative to ^{174}W are shown in Fig. 6.19, in comparison with the experimental ones. Fig. 6.20 shows the comparison between the total number of paths obtained by applying the statistical fluctuation analysis to experimental (open black diamonds) and simulated (red line) matrices; the number of discrete bands predicted by the Cranked Shell Model is also reported (blue line).

One can observe that the values obtained with the simulation of the decay flux and the ones extracted with the microscopic nuclear structure calculations are very similar and in agreement with the experimental data.

Concerning the evaluation of the number of low and high K bands separately, it is important to established a criterion to define low-K and high-K states. As discussed in Sec. 4.4, experimentally it is possible to select specific configurations either by gating on transitions belonging to low-K bands or by using a time-gate to select high-K bands through isomeric transitions.

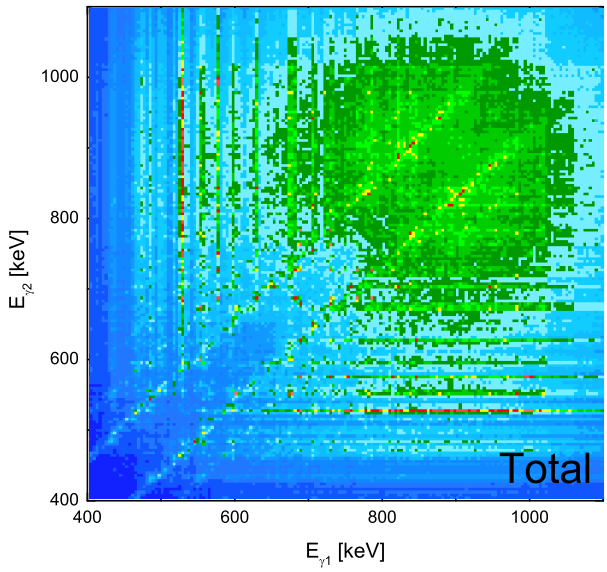

Figure 6.18: Simulated total $\gamma - \gamma$ matrix of ^{174}W, after the subtraction of the yrast band.

In the simulation a criterion to distinguish between low and high K states has been introduced. In practice, a threshold value, called K_{thr}, is set, so that the states characterised by values of K greater then this threshold are defined as "high K" states, while the others are treated as "low K" states.
In order to update 2D $\gamma - \gamma$ matrices in coincidence with low (high) K states, it is required that the last two transitions of a cascade end on states characterised by a K value lower (greater) then K_{thr}. The requirement to have at least two different transitions is used to ensure that these transitions belong to a band in order to update a 2D matrix gated by such configuration.
Two different values of K_{thr} have been tested: the first is $K_{thr} = 6$ that was the one that has given the best agreement between experimental data and Cranked Shell Model calculations (see Sec. 5.3.2) and the second one is $K_{thr} = 8$. This latter value was used in an analogous analysis on ^{163}Er [4, 16].

Fig. 6.21 shows $\gamma - \gamma$ matrices gated by low-K (top) and high-K (bottom) configurations, obtained with the requirement $K_{thr} = 6$. Similar matrices with $K_{thr} = 8$ have also been built. The contribution of the total yrast matrices has

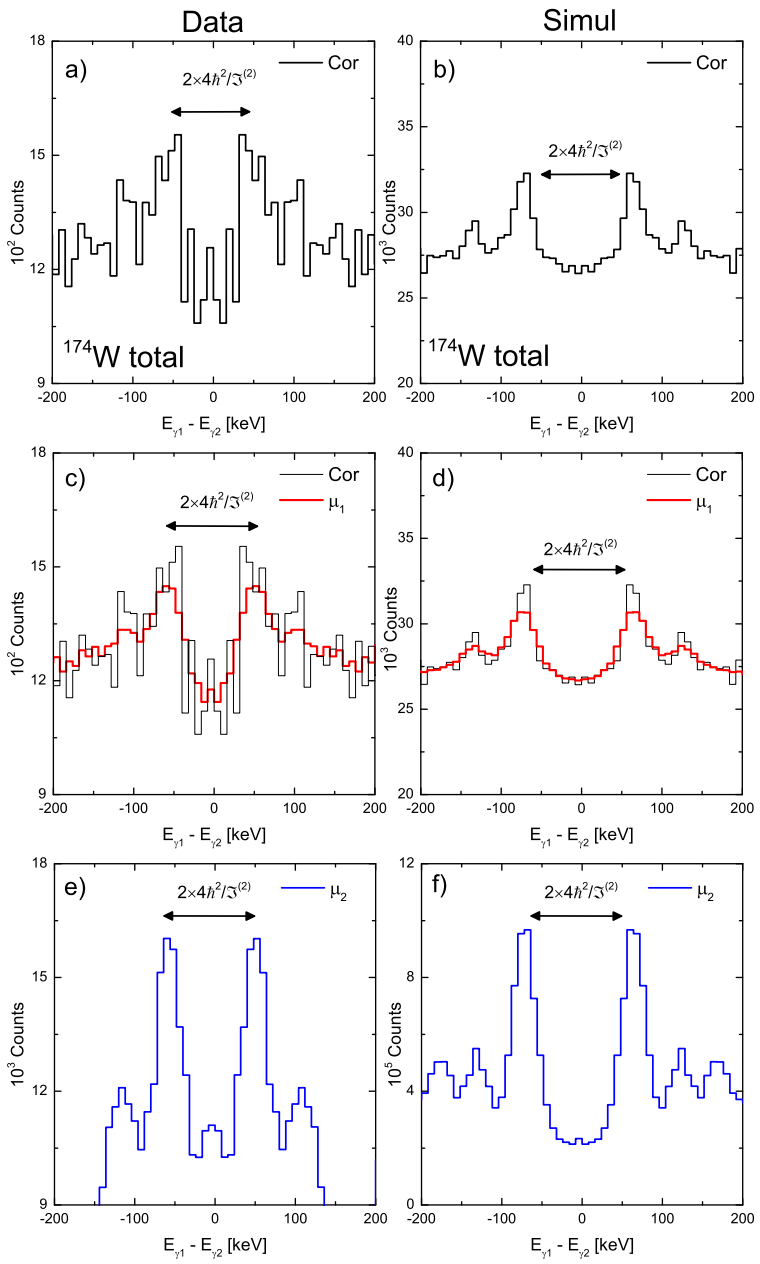

Figure 6.19: Panels b), d) and f): Perpendicular cuts (60 keV wide) of the COR, μ_1 and μ_2 simulated matrices relative to ^{174}W, in comparison with the experimental ones (Panels a), c) and e)). Cuts have been made at $\langle E_\gamma \rangle = 880\ keV$.

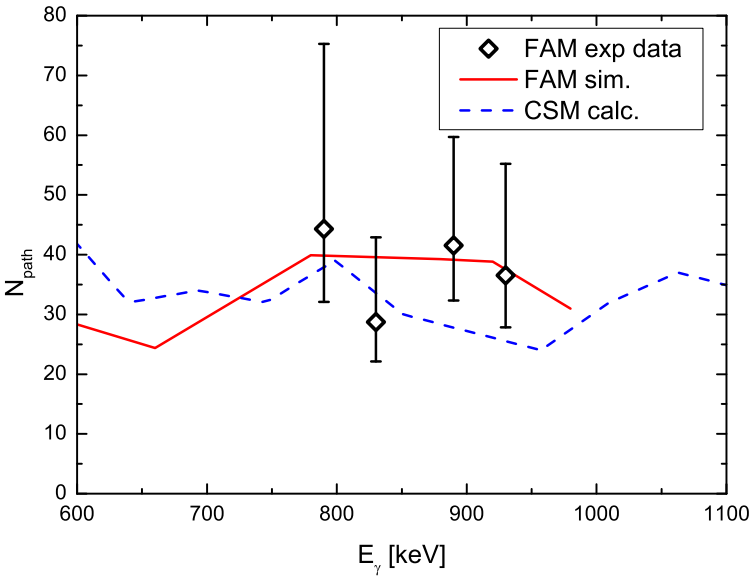

Figure 6.20: Comparison between the total number of paths obtained by applying the statistical fluctuation analysis to experimental (open black diamonds) and simulated (red line) matrices; the number of discrete bands predicted by the Cranked Shell Model is indicated with a blue line.

been subtracted to the low-K matrix, as done for the total $\gamma - \gamma$ matrices.

Cuts at $\langle E_\gamma \rangle = 880\ keV$ of the COR, μ_1 and μ_2 simulated matrices relative to low-K and high-K are shown in Fig. 6.22 and 6.23 respectively, in comparison with the experimental ones.

The statistical fluctuation analysis has been performed on both low-K and high-K matrices and the results have been compared to the experimental number of paths, as shown in Fig. 6.24. As one can see, the condition $K_{thr} = 6$ (indicated with red lines) gives a better reproduction of the data, both for the low-K and high-K number of paths. This value of K_{thr} was the same deduced from the comparison between experimental data and microscopic calculations, as discussed in Sec. 5.3.2. Fig. 6.25 summarizes the results obtained for the of number of low-K and high-K paths extracted with the three different methods, namely i) statistical fluctuation analysis on experimental data, ii) statistical fluctuation analysis on simulated matrices ($K_{thr} = 6$) and iii) microscopic Cranked Shell Model calculations ($K_{thr} = 6$). As one can see reasonable agreement is obtained between experimental data, simulations and calculations, confirming the validity of the technique and of the data interpretation.

6.6.2 Rotational planes analysis

The *MONTESTELLA* simulation code can produced rotational planes distributions, allowing to study three dimensional correlations between γ rays in the cascade. In this case, only the $N = 1$ rotational plane was studied, being the only one available in the data. The obtained matrix is shown in Fig. 6.26, where the second ridge is clearly visible.

The statistical fluctuation analysis has been performed on the ridge structure: an example of perpendicular cut is shown in Fig. 6.27; the COR spectrum is plotted in panel a), while μ_1 and μ_2 are shown in panel b) and c), respectively.

Results are plotted in Fig. 6.28 and are compared with experimental data and Cranked Shell Model calculations. As one can see, the total number of discrete paths formed by three consecutive transitions ($N_{steps} = 3$), extracted from the simulated matrix, agrees well with the experimental data and the microscopic Cranked Shell Model calculations.

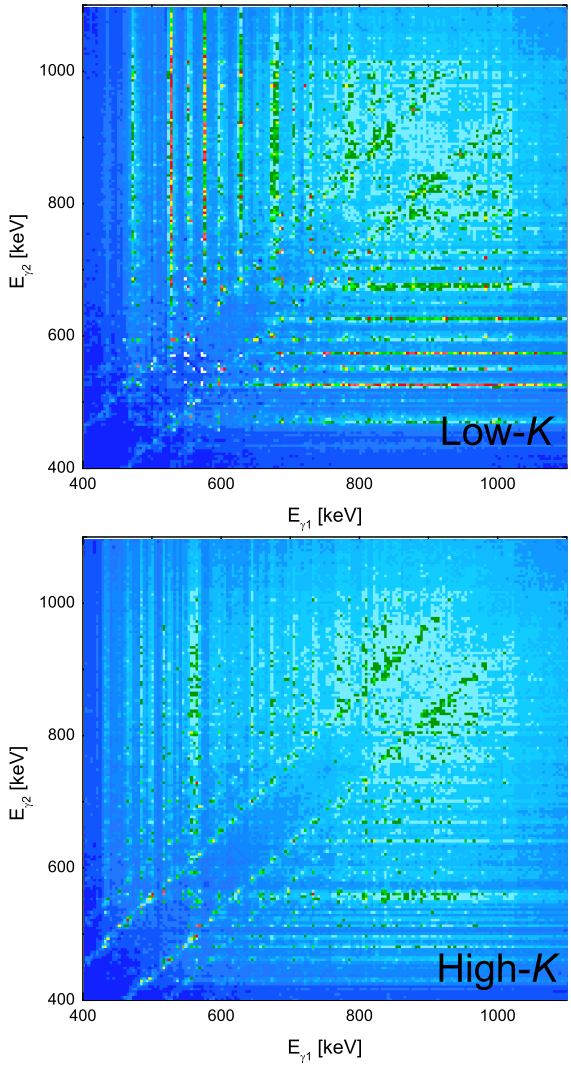

Figure 6.21: Simulated $\gamma - \gamma$ matrices gated by low-K (top) and high-K (bottom) configurations, obtained using the simulation code with the requirement $K_{thr} = 6$. The ridge structure, running parallel to the diagonal $E_{\gamma 1} = E_{\gamma 2}$, is evident in both matrices.

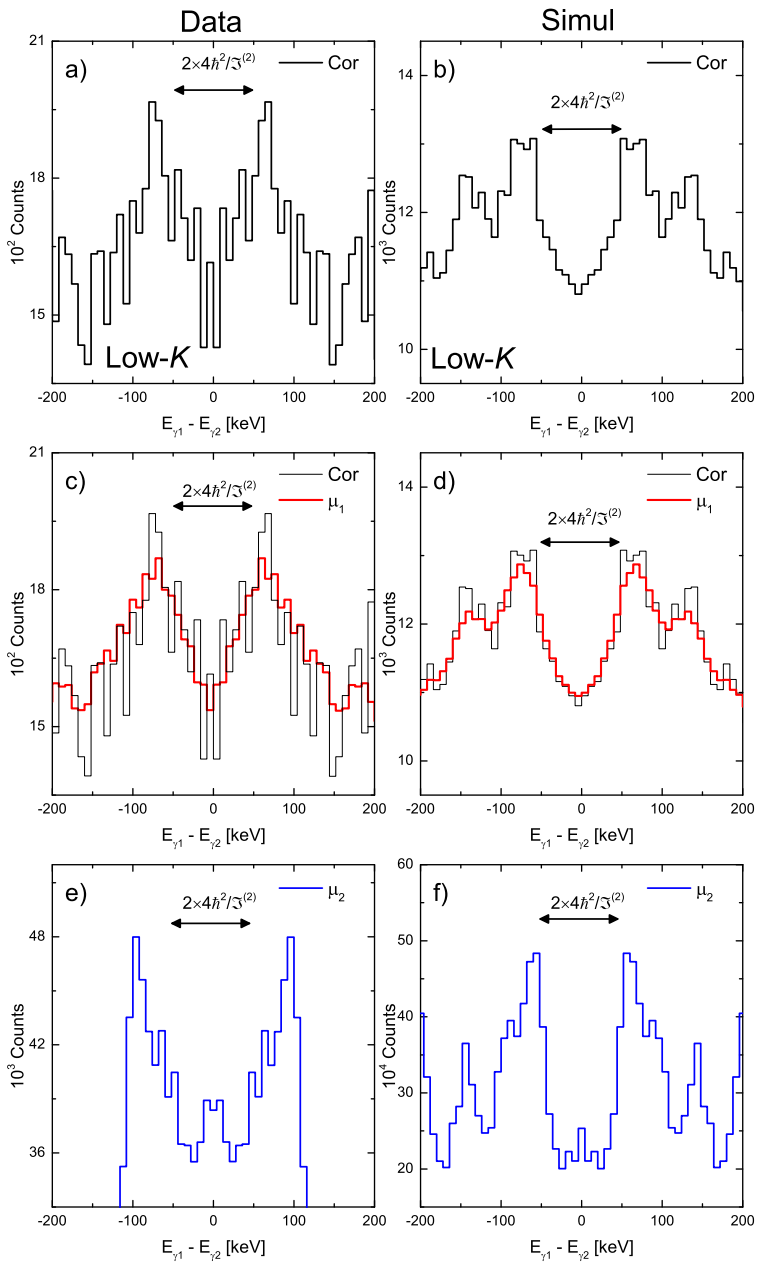

Figure 6.22: Panels b), d) and f): Perpendicular cuts (60 keV wide) of the COR, μ_1 and μ_2 simulated matrices relative to low-K bands, in comparison with the experimental ones (Panels a), c) and e)). Cuts have been made at $\langle E_\gamma \rangle = 820\ keV$.

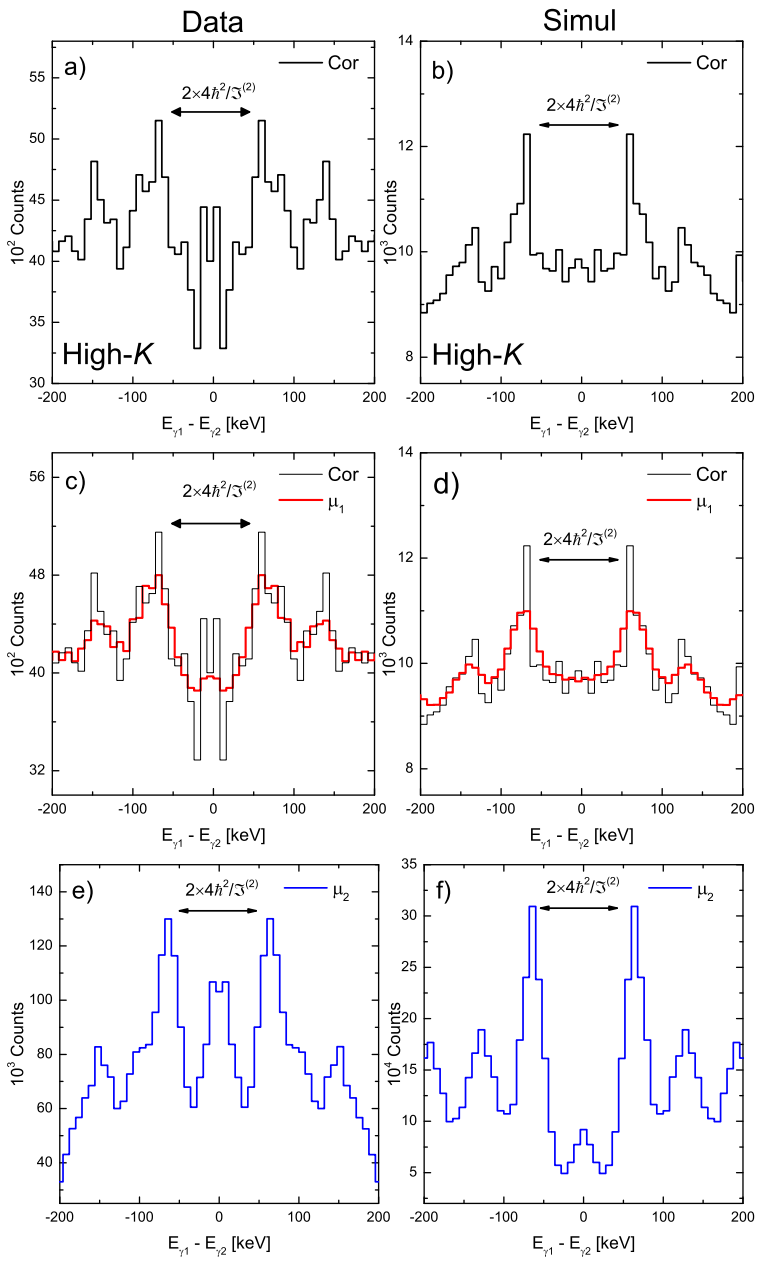

Figure 6.23: Panels b), d) and f): Perpendicular cuts (60 keV wide) of the COR, μ_1 and μ_2 simulated matrices relative to high-K states, in comparison with the experimental ones (Panels a), c) and e)). Cuts have been made at $\langle E_\gamma \rangle = 820\ keV$.

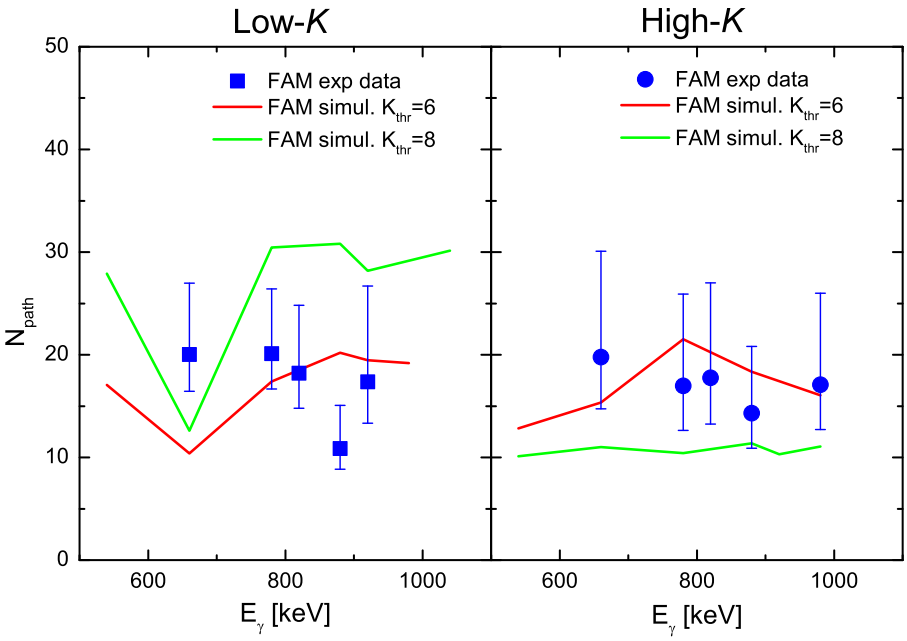

Figure 6.24: Number of paths obtained from the ridge analysis of low-K (left) and high-K (right) configurations. Experimental data are indicated by symbols. In the simulation two different value of K_{thr} have been used: red lines corresponds to $K_{thr} = 6$ while green line to $K_{thr} = 8$ (see text for details).

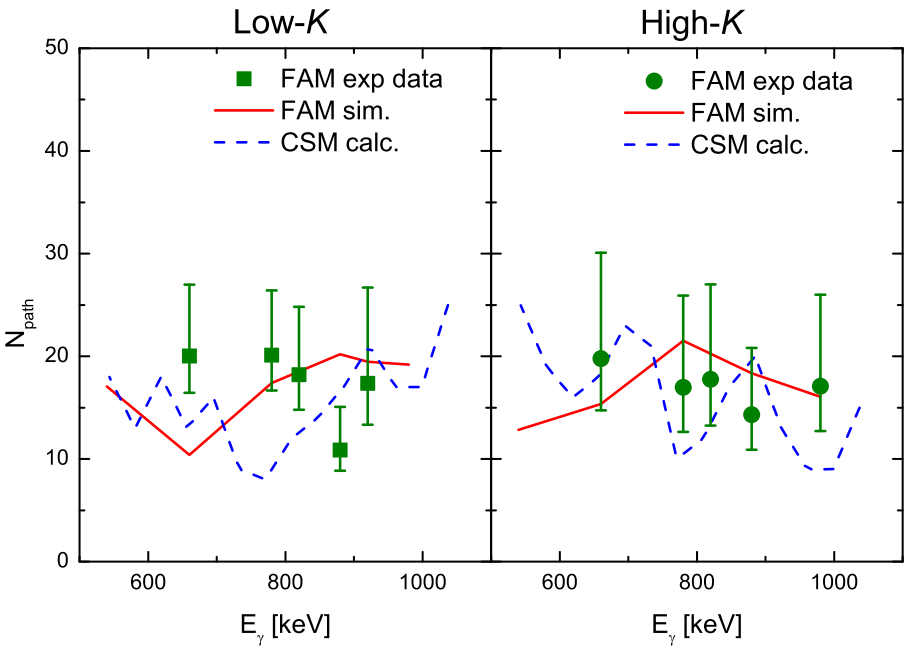

Figure 6.25: Comparison between the number of low-K (on the left) and high-K (on the right) paths extracted with three different methods. Experimental data are indicated by symbols; red lines correspond to the fluctuation analysis of simulated data, while blue dashed line to the microscopic Cranked Shell Model calculations. In the last two methods $K_{thr} = 6$ was used.

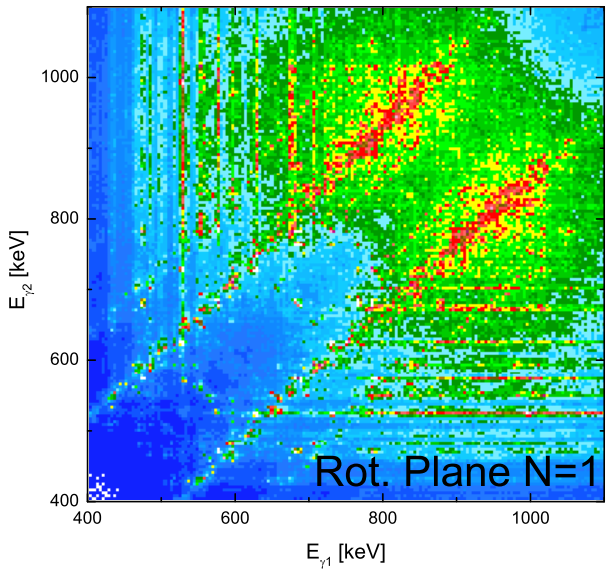

Figure 6.26: Simulated rotational plane with $N = 1$, collecting the whole decay flux.

6.6.3 Covariance analysis

After evaluating the number of discrete bands of the ^{174}W nucleus, the covariance analysis has been performed [61]. The three simulated matrices, used for the statistical fluctuation analysis of the ridge structures, were considered in pairs, in order to extract the correlation coefficients, using the procedure described in Sec. 5.2.6. In the simulation, it is possible to perform a covariance analysis between the following combinations of configurations: i) the total data set vs. low-K (or high-K) states and ii) low-K vs. high-K configurations. In case i) experimental data will also be compared to the simulation. Even for this analysis, two different values of K_{thr} (i.e. 6 and 8) have been tested.

First of all, the correlation coefficients between the total simulated matrix and a matrix updated in coincidence with low-K and high-K cascades are described. The results are reported in Fig. 6.29, using $K_{thr} = 6$ on the left, and $K_{thr} = 8$ on the right. Using $K_{thr} = 6$ the correlation coefficients assume more similar values than for $K_{thr} = 8$, supporting the hypothesis of equal-population of low-K and high-K bands, as it was found in the experimental data analysis. Moreover, the

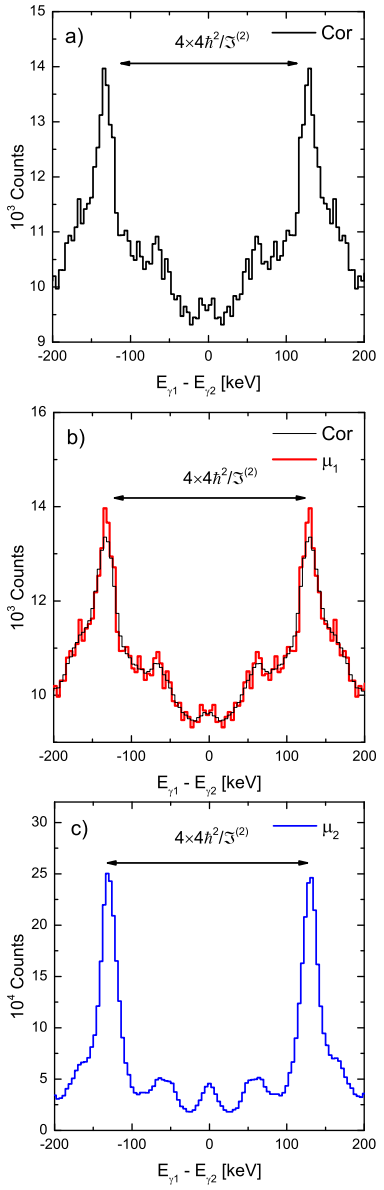

Figure 6.27: Panel a): Perpendicular cuts (60 keV wide) of the COR matrix relative to the $N = 1$ rotational plane of ^{174}W. The corresponding cuts of μ_1 and μ_2 spectra obtained from the $STATFIT$ code are reported in panels b) and c). Cuts have been made at $\langle E_\gamma \rangle = 840\ keV$.

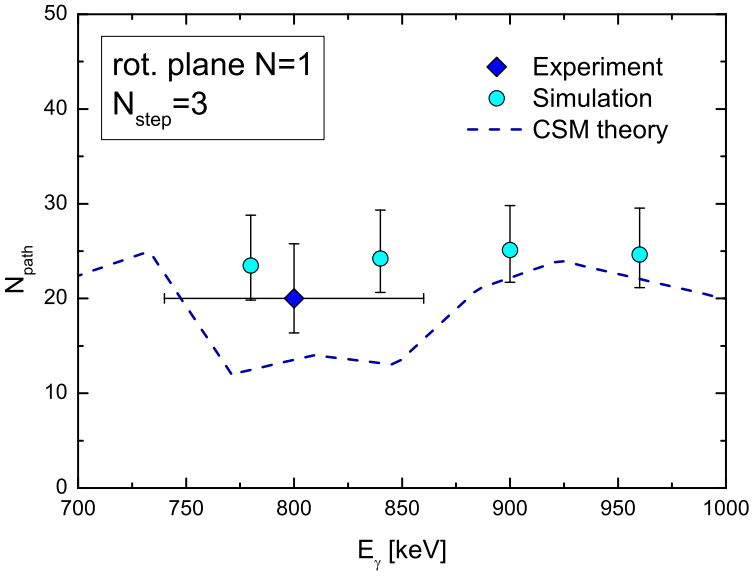

Figure 6.28: Comparison between the total number of paths with $N_{steps} = 3$ extracted using experimental (blue diamonds) and simulated (cyan circles) rotational planes ($N = 1$). Corresponding results from the Cranked Shell Model calculations are shown by the blue line.

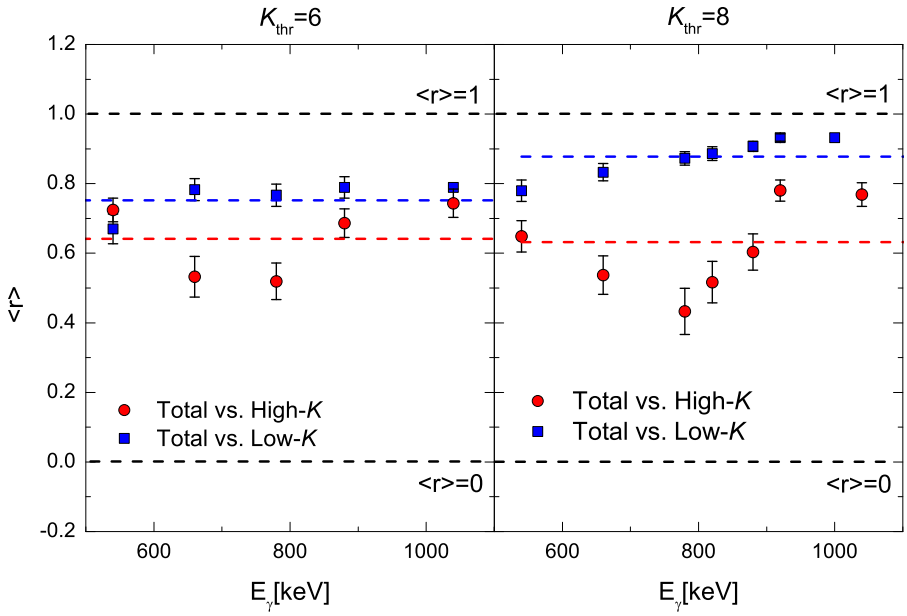

Figure 6.29: Correlation coefficients between the total matrix and low-K (and high-K) spectra are indicated by blue squares (red circles), as obtained from the covariance analysis of the simulated spectra. Coloured dashed lines indicate the mean values of the distributions. The threshold used to discriminate between low-K and high-K is $K_{thr} = 6$ on the left, and $K_{thr} = 8$ on the right.

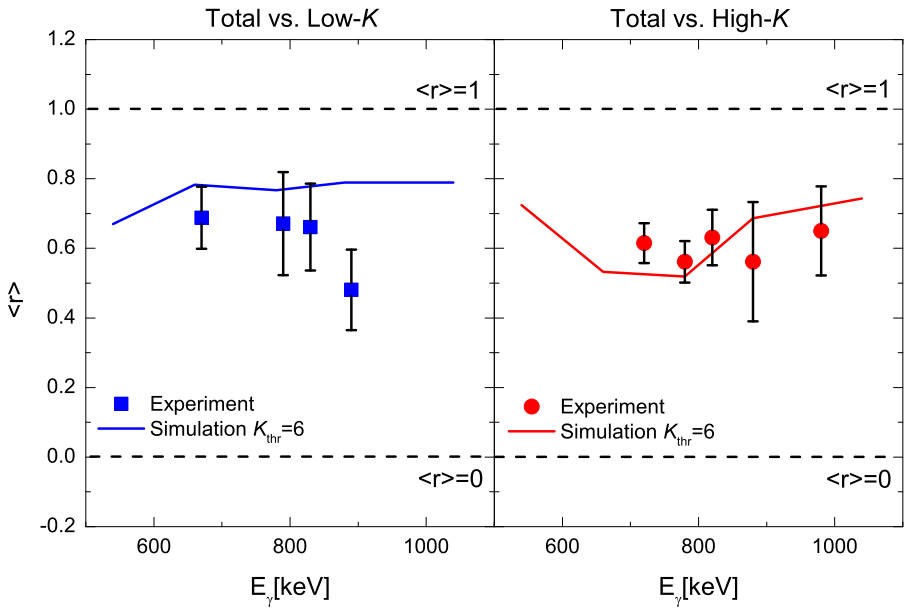

Figure 6.30: Comparison between correlation coefficients obtained with the analysis of experimental (symbols) and simulated (lines) matrices. The Total vs. low-K case is reported on the left, while the Total vs. high-K analysis is given on the right.

comparison between experimental data and simulated ones with $K_{thr} = 6$ gives a good agreement in both cases (see Fig. 6.30).

The most important case for this kind of study, namely the ridge covariance between simulated data gated by low-K and high-K configurations is now considered. In this case a direct comparison with the experimental data is not possible, as discussed in Sec. 5.3.3, due to the limited statistics of the data set. In this case, only $K_{thr} = 6$ have been considered.
As shown in Fig. 6.31, the ridges covariance on the simulated low-K and high-K spectra give very small values, consistent with $r = 0$, especially in the low-energy region below 850 keV ($I < 30\hbar$), where the majority of the discrete flux goes. This results confirm the robustness of the K quantum number selection rules up to the region where rotational damping sets in (namely $U < 1$ MeV above yrast), as already observed in the case of ^{163}Er [4, 16].

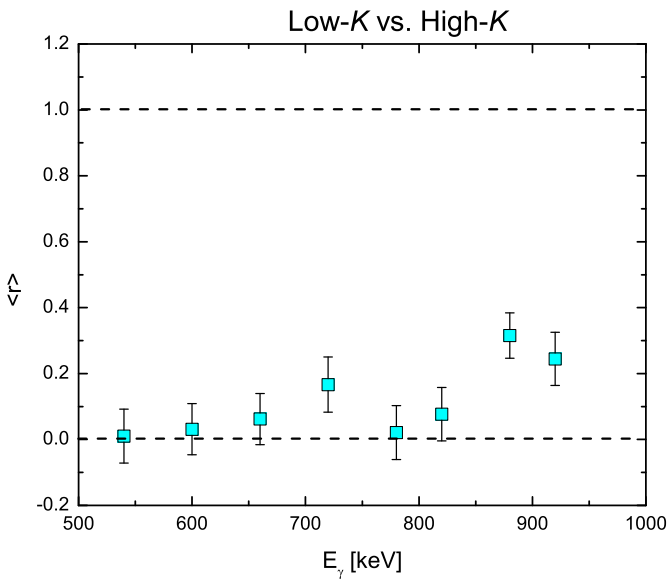

Figure 6.31: High-K vs. low-K correlation coefficient obtained from the covariance analysis of the ridge structures, for the simulated data.

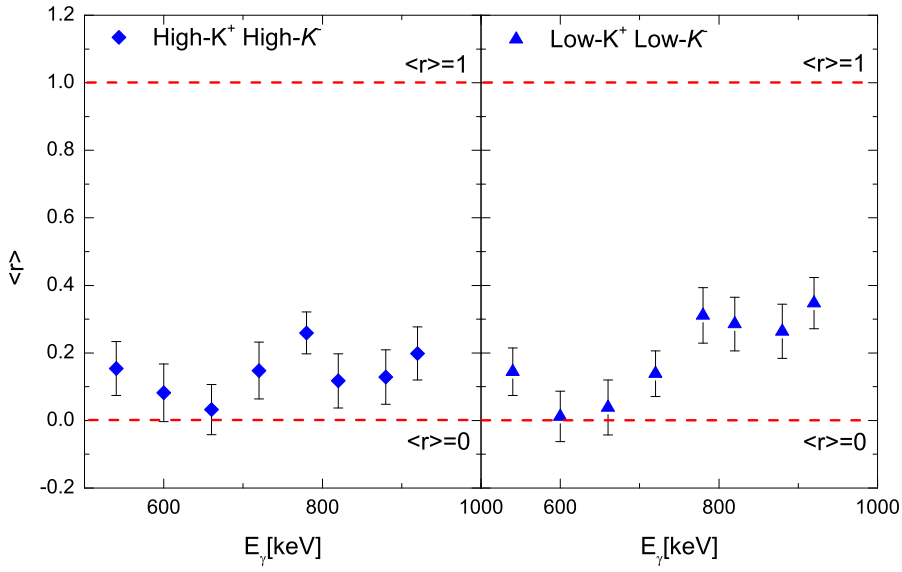

Figure 6.32: Correlation coefficients obtained from the covariance analysis of the ridges, for simulated high-K vs. high-K (on the left) and low-K vs. low-K (on the right), with different parity.

In addition to the three combinations just described, we also performed the covariance analysis on matrices with the same value of K quantum number, but having different parities. This study allows to test the correlations among low-K or high-K discrete bands, induced by E1 transitions, between states with similar K quantum numbers.

Results are summarized in Fig. 6.32: on the left (on the right) is reported the correlation coefficient between high-K (low-K) states with different parities. The obtained correlation coefficient displays a different trend, depending on the combination of K values of the pair of spectra analysed. In particular, a little degree of mixing is found among discrete bands characterised by similar values (high or low) of the K quantum number. Such a mixing is rather weak, both for low and for high K states, resulting in $\approx 25\%$ and $< 20\%$ correlations due to E1 cross talking decays. This result is expected from the E1/E2 competition within the γ cascades, as also observed in the previous studied case of ^{163}Er [4, 16].

One can then conclude that the covariance analysis of the ridges points in the direction of a persistence of the K quantum number selection rules in the cold region of rotational motion, namely up to $\sim 1\ MeV$ excitation energy, before a mixing among rotational states sets in as a consequence of rotational damping.

Chapter 7

K hindrance to γ decay

The study of the warm rotation in ^{174}W along discrete rotational bands, presented and discussed in Chap. 6, has clearly evidenced the importance of introducing a quenching in the E1 decay between low-K and high-K bands. In the present Chapter we discuss this problem in a more general context, namely we will try to relate our results to the reduced hindrance values f_ν, extracted from standard discrete spectroscopy studies of high-K isomers [10]. As it will be shown, our analysis is consistent with the general trend obtained from the analysis of K-isomers [10, 69].

7.1 Sensitivity of the simulation to K hindrance

In order to verify the sensitivity of the simulation to the introduction of the $P_{\Delta K}(K_i, K_f)$ term in the E1 decay probability, the number of paths for different configurations has been extracted using different K hindrance values. The total number of paths for the ^{174}W nucleus and the number of low-K and high-K bands have been evaluated as a function of the σ parameter used to define the $P_{\Delta K}(K_i, K_f)$ expression (see Sec. 6.2.5).
Obviously, the $T_{band}(E1, U)$ will change according to Eq. 6.20, because $P_{\Delta K}(K_i, K_f)$ is σ-dependent. In order to correctly reproduce the number of statistical E1 decays, the same procedure described in Sec. 6.4 has been performed for every value of the σ parameter used. The corrective factors f found are reported in Tab. 7.1.

σ	0.3	2.5	10	> 500 ($P_{\Delta K} = 1$)
f	16	2.4	0.82	0.42

Table 7.1: Corrective factors f used to reproduce the correct number of statistical E1 decays. $f = 16$ used for $\sigma = 0.3$ is the same as in Sec. 6.4.

Fig. 7.1 shows the trend obtained for the number of paths (N_{path}), in three different cases (total, low-K and high-K), using $\sigma = 0.3,\ 2.5$ and $P_{\Delta K}(K_i, K_f) = 1$ (meaning $\sigma > 500$). The case $\sigma = 10$ has also been considered, for high-K bands only.

As one can observe, the total number of bands and the number of low-K bands extracted from the simulation are independent from the σ parameter, pointing to a very reduced sensitivity to the K-hindrance introduced in the E1 decay probability. This is true even in the case of average values, between 750 keV and 950 keV, with smaller error bars on N_{path} (see the insets of Fig. 7.1): all values obtained with the simulation are within the error bars of the experimental data. On the other hand, it is found that the number of high-K bands depends more strongly on the σ parameter and experimental data are mostly consistent with $\sigma = 0.3$ and $\sigma = 2.5$. Note that $\sigma = 0.3$ is the value found in literature [1], which has been used to perform the entire analysis on simulated data.

This observation confirms that an hindrance, which corresponds to strong selection rules on the γ decay, is needed to well reproduced the number of high-K paths. Without the hindrance factor ($P_{\Delta K}(K_i, K_f) = 1$) or with relaxed conditions ($\sigma = 10$), a number of high-K bands larger than even the microscopically calculated ones is found (see Fig. 6.24). Cranked Shell Model calculations gives an upper limits to this, therefore we conclude that if the K hindrance factor is not correctly included, meaningless results are obtained.

7.2 Evaluation of the $P_{\Delta K}(K_i, K_f)$ integral

In this section we investigate in detail the $P_{\Delta K}(K_i, K_f)$ term, since we have found it plays an important role in the description of the γ-decay of high-K isomers.

In order to obtain quantitative information, the analysis of $P_{\Delta K}$ is performed by averaging over groups of states, for different values of spin and excitation energy.

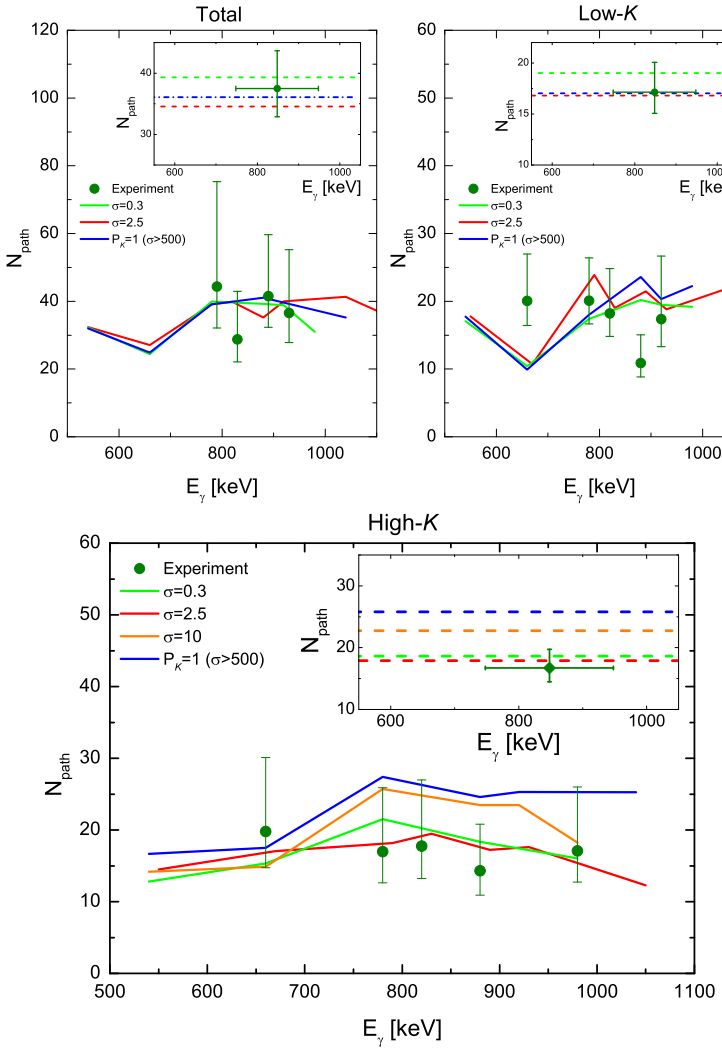

Figure 7.1: Comparison between experimental and simulated data, as a function of the σ parameter. $\sigma = 0.3,\ 2.5$ and $P_{\Delta K}(K_i, K_f) = 1$ (corresponding to $\sigma > 500$) have been used to calculate the total number of paths and the number of low-K bands (upper panel). Since the stronger sensitivity to σ was observed in the number of high-K bands, $\sigma = 10$ was added as intermediate value (bottom panel) in this last case. Insets show values averaged between 750 keV and 950 keV. Error bars on E_γ in the experimental points refer to the width of the cut used for statistical fluctuation analysis.

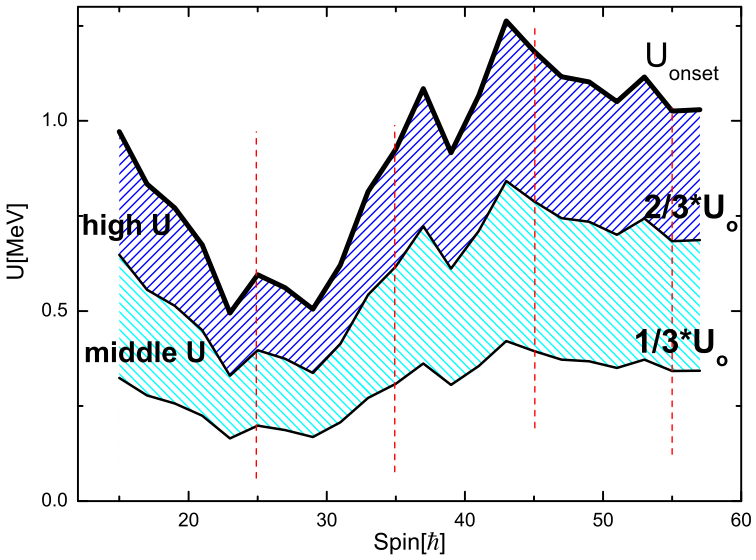

Figure 7.2: The spin-energy regions considered for the $P_{\Delta K}(K_i, K_f)$ analysis. The middle energy region is shaded in cyan while the high energy one is coloured in blue.

Starting from the microscopic calculations, the value of $P_{\Delta K}$ for different sets of energy levels has been extracted. According to Eq. 6.7 the following parameters are needed: K_i, K_f, σ_i and σ_f. In order to find these quantities, microscopic energy levels, calculated using the Cranked Shell Model (CSM), have been used.
First of all, a subset of states has been selected, asking for two consecutive transitions characterized by $n_b < 2$ (see Eq. 5.36), in the energy region where $U < U_{onset}$ (see Fig. 7.2). This requirement is needed in order to test the relevance of $P_{\Delta K}(K_i, K_f)$ for the decay among discrete bands.
The energy interval below U_{onset} has been divided in three regions, equally wide, as a function of spin. The middle (high) excitation energy region is shaded in cyan (blue) in Fig. 7.2. Spin regions centred around 30, 40 and 50$\hbar$ (10$\hbar$ wide) were considered (delimited by red dashed lines in Fig. 7.2).
Fig. 7.3 plots the energy distributions of the subsets of levels here selected, divided as low ($K \leq 6$, in blue) and high ($K > 6$, in red) K states. The lowest energy region is almost empty for all spins, since it corresponds roughly to the energy gap between the yrast band and the first excited levels. Therefore, this region has not

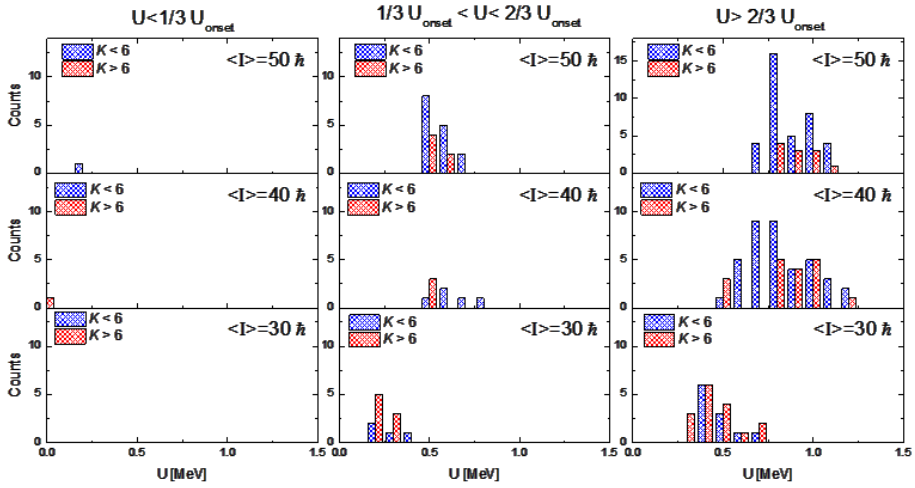

Figure 7.3: Distributions of microscopically calculated energy levels as a function of U, for different spin regions. The lowest energy region is almost empty for all spins, therefore it has not been considered in the analysis. The contribution of low ($K \leq 6$, in blue) and high ($K > 6$, in red) K states is shown separately.

been considered in the analysis. Moreover, the low (high) K levels will be considered as final (initial) states in the calculation of $P_{\Delta K}(K_i, K_f)$.

For each group of states the centroid of the average K value and the corresponding σ_K given by the Cranked Shell Model (see Eq. 6.2 and 6.3) have been calculated, in order to extract a representative K-distribution for each group of levels. In this way, K_i, K_f, σ_i and σ_f needed to calculate $P_{\Delta K}(K_i, K_f)$ are obtained. Tab. 7.2 reports these quantities.

Since the high-K ($K > 6$) distributions have very low statistics in the middle energy region at $I = 40\hbar$ and $I = 50\hbar$, it has been decided to sum together the middle and the high energy regions for these spin values and to calculate a unique set of parameters. After that, the centroid $< U >$ and standard deviation σ_U of the U distributions have been calculated without separating between low and high-K states. Tab. 7.3 contains the final parameters, used for this analysis.

Fig. 7.4 shows the distributions of the K-quantum number calculated as a Gaussian function centred in K_i (K_f) with $FWHM = 2.35 \cdot \sigma_i(\sigma_f)$, where K_i (K_f) and

	$I = 30\hbar$		$I = 40\hbar$		$I = 50\hbar$	
	middle U	high U	middle U	high U	middle U	high U
K_i	8.12	8.69	6.00	9.47	6.50	9.55
K_f	2.50	3.55	3.60	3.33	4.00	3.89
σ_i	1.81	1.91	2.17	2.27	2.75	2.64
σ_f	1.75	1.91	1.80	1.86	2.23	2.09

Table 7.2: Parameters extracted from the average K value and σ_K given by the CSM calculations for different excitation energy regions at spin $I = 30,\ 40,\ 50\hbar$.

	$I = 30\hbar$		$I = 40\hbar$	$I = 50\hbar$
	middle U	high U	middle U + high U	middle U + high U
$< U > [MeV]$	0.26	0.47	0.82	0.79
$\sigma_U [MeV]$	0.07	0.11	0.14	0.09
K_i	8.12	8.69	8.97	8.74
K_f	2.50	3.55	3.36	3.92
σ_i	1.81	1.91	2.26	2.29
σ_f	1.75	1.91	1.80	2.13

Table 7.3: Parameters used to calculate $P_{\Delta K}(K_i, K_f)$ averaging over the middle and high energy regions at $I = 30,\ 40$ and $50\hbar$.

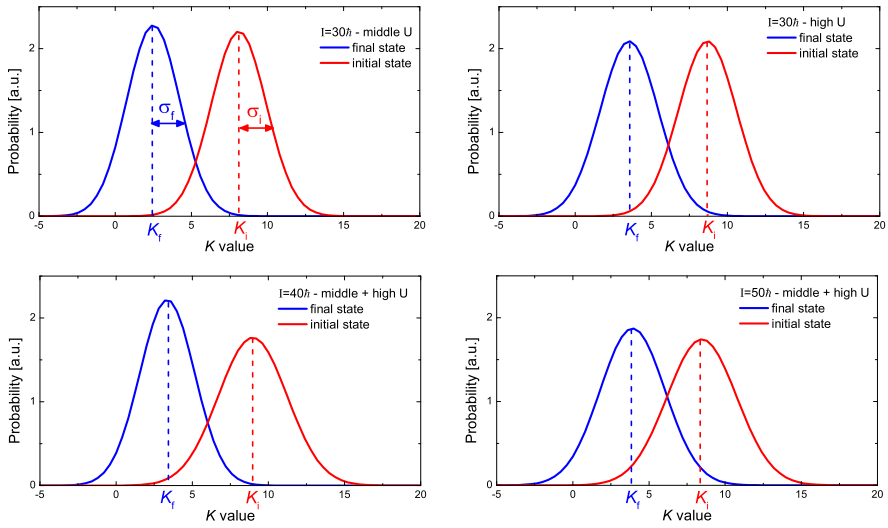

Figure 7.4: Representative distributions of the K-quantum number for the (I, U) phase-space regions here considered. K_i and K_f are indicated for all curves, while σ_i and σ_f are given in the first panel only, as an example.

$\sigma_i(\sigma_f)$ are the parameters taken from Tab. 7.3.

The overlap region between the two curves corresponds to the expression

$$\int\int dK_1 dK_2 \; e^{\frac{(K_1-K_i)^2}{2\sigma_i^2}} \; e^{\frac{(K_2-K_f)^2}{2\sigma_f^2}}$$

entering into the Eq. 6.7: the smaller is the overlap, the smaller is the integral value. Therefore in case of well-separated distribution the K-hindrance between low-K and high-K states is stronger. In Eq. 6.7, the additional term

$$e^{-\frac{|K_1-K_2|}{\sigma}}$$

introduce a further quenching to the decay between states that have different K distribution.

The $P_{\Delta K}(K_i, K_f)$ values defined in Eq. 6.7 are finally calculated by a program that discretizes the integrals in steps of 0.34 for K_i and K_f and in steps of 0.5 for σ_i and σ_f. For this reason it is not possible to have a precise evaluation of $P_{\Delta K}(K_i, K_f)$ for the parameters that characterize the representative distributions (given in Tab. 7.3 and Fig. 7.4). The method used to overcome this approximation

		$\sigma = 0.3$		$\sigma = 10$	
Region	ΔK	$P_{\Delta K}(K_i, K_f)$	σ_{PK}	$P_{\Delta K}(K_i, K_f)$	σ_{PK}
$I = 30\hbar$, middle U	5.62	0.0081	0.0050	0.5859	0.0115
$I = 30\hbar$, high U	5.14	0.0172	0.0029	0.6169	0.0153
$I = 40\hbar$	5.61	0.0123	0.0048	0.6075	0.0133
$I = 50\hbar$	4.55	0.0250	0.0034	0.6450	0.0133

Table 7.4: The $P_{\Delta K}(K_i, K_f)$ values calculated for the four representative regions using $\sigma = 0.3$ and $\sigma = 10$ (see text for details).

is to consider the two closest values of each parameter and to calculate $P_{\Delta K}(K_i, K_f)$ using all possible combinations of them. In order to have a correct evaluation of $P_{\Delta K}(K_i, K_f)$, the values obtained in this way are averaged and their standard deviation is calculated.
This work has been done using $\sigma = 0.3$ in Eq. 6.7, that corresponds to the standard value from literature [1], and $\sigma = 10$ that is only a little out of the error bars in the high-K plot of Fig. 7.1. The results of this procedure are shown in Tab. 7.4.

7.3 From $P_{\Delta K}(K_i, K_f)$ to standard decay hindrance f_ν

The final step of our $P_{\Delta K}(K_i, K_f)$ analysis consists in the comparison between the obtained $P_{\Delta K}(K_i, K_f)$ values and the standard values for the decay hindrance f_ν, defined according to Eq. 1.36. As already explained in Chap. 1, ν is the degree of forbiddenness, defined as $\nu = \Delta K - \lambda$, being λ the multipolarity of the γ transition. The decay hindrance f_ν depends on the ν degree of forbiddenness as follows [10]

$$f_\nu = F_\nu \cdot \exp\left[-\frac{3}{\nu}\sqrt{\frac{\pi^2}{6} g_0 \Delta E} \right] \tag{7.1}$$

where $\frac{\pi^2}{6} g_0 = \frac{A}{7.5} MeV^{-1}$ and ΔE is the excitation energy of the considered level relative to the one of a rigid rotor. F_ν is a constant for a given value of ν, extracted by fitting the experimental data. The expression 7.1 is obtained assuming that the

density of states increases exponentially with $\sqrt{\Delta E}$, as explained in Ref. [10].
It should be noted that the reduced hindrance declines exponentially with the square root of the energy difference.
Since our *MONTESTELLA* simulation calculations considers only the hindrance on E1 transitions ($\lambda = 1$), it has been assumed that $\nu = \Delta K - 1$. Hence the four points that we have considered in our analysis, have ν between 3.5 and 5 (see Tab. 7.4).

Finally we have related f_ν to $P_{\Delta K}(K_i, K_f)$ by the following expression

$$f_\nu = \frac{1}{P_{\Delta K}(K_i, K_f)} \tag{7.2}$$

leading to the values plotted in Fig. 7.5, together with experimental data of previous analysed nuclei in the mass region $A \sim 180$ [10], already shown in Chap. 1. The solid blue curve has been calculated through Eq. 7.1, using $\nu = 4$ and calculating F_ν by normalization with the lowest energy data points (^{178}Hf), as done in Ref. [10]; the dashed blue line has been calculated with the same F_ν value but with $\nu = 3$.
It is found that f_ν values obtained with $\sigma = 0.3$ (green circles) are in good agreement with the hindrance values obtained experimentally from the discrete K-isomers E2 decay analysis in the same mass region, while $\sigma = 10$ (orange diamonds) gives values completely out from the curves.
The reduced hindrance factor relative to the discrete 1879 keV E2 transition depopulating the high-K ($K = 12$) isomer of ^{174}W, has been added to the plot of Fig. 7.5 in order to compare it to the systematic of E2-E3 isomers in the mass region $A \sim 180$. The excitation energy of the initial state of this transition has been calculated with respect to a rigid rotor coinciding with the yrast band of CSM, at the same spin ($I = 12\hbar$), while the hindrance factor has been taken from Ref. [5]. The obtained data point is compatible with the general trend of the other discrete isomers just discussed.
The other discrete isomeric transition observed in ^{174}W, an M1 decay having $E_\gamma = 247$ keV [5], has been treated separately because the trend of F_W as a function of ΔK depends on the type (magnetic or electric) and the multipolarity of the decay transition [25]. In the case of this 247 keV line, one has $\Delta K = 2$, meaning $\nu = 1$, and a reduced hindrance factor $f_\nu = F_W = 1.4 \cdot 10^5$ (see Eq. 1.36) . As shown in Fig. 7.6, this experimental value agrees with previous experimental

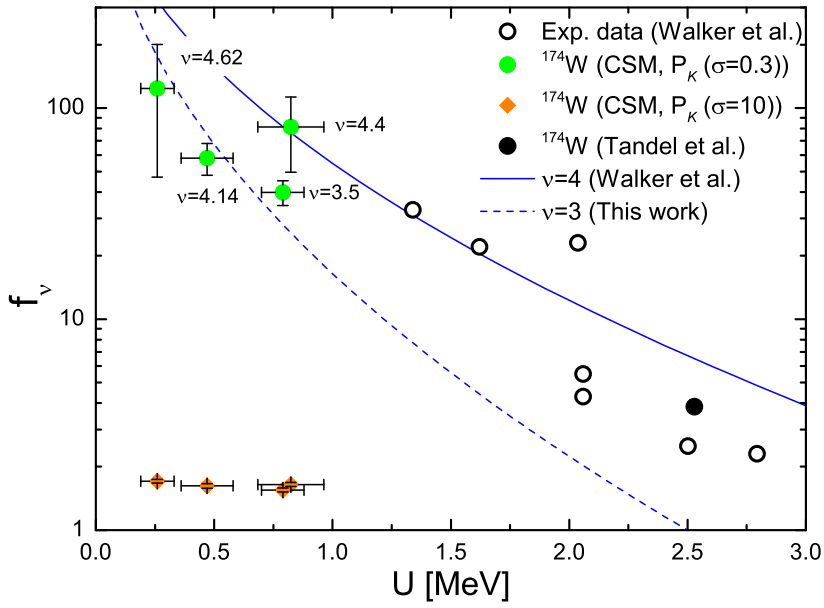

Figure 7.5: Reduced hindrance f_ν, as a function of internal energy U for nuclei in the mass region $A \sim 180$. Open circles refer to experimental data from Ref. [10]. Green circles (orange diamonds) have been obtained, in this work, from the analysis of the hindrance on the E1 decay of ^{174}W, using $\sigma = 0.3$ ($\sigma = 10$) in the expression of $P_{\Delta K}(K_i, K_f)$ of Eq. 6.7. The black circle refers to the hindrance factor measured for the high-K ($K = 12$) isomer of ^{174}W [5]. The solid blue line through the data represents the f_ν curve for $\nu = 4$, normalised at ^{178}Hf. The dotted blue line corresponds to $\nu = 3$ (see text for details).

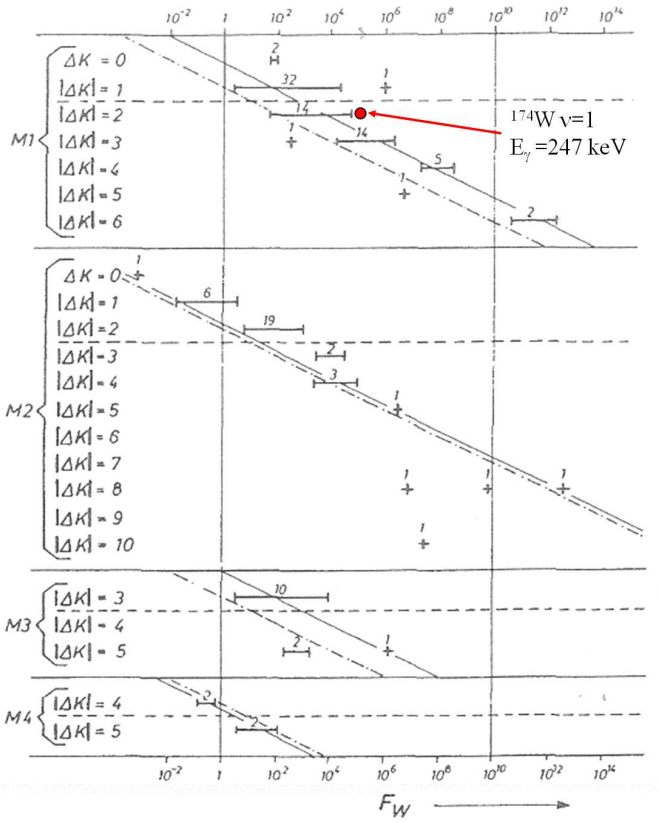

Figure 7.6: Range of hindrance factors relative to the Weisskopf estimate F_W of magnetic γ-ray transitions for different $|\Delta K|$ values [25]. Bars correspond to experimental values and the numbers above them indicate the number of γ-ray transitions considered. The dot-and-dash sloping lines show the dependence of F_W on ΔK according to the empirical rule proposed by Rusinov [25]. The solid sloping lines are arbitrarily drawn through the experimental ranges of F_W parallel to the dot-and-dash lines. The red circle corresponds to experimental hindrance of the M1 247 keV γ transition of ^{174}W [5].

works of Ref. [25].

As one can see from Fig. 7.5 the theoretical curve of decay hindrance shows a decrease with excitation energy. This is due to the K-mixing process, that becomes more important in the high excitation energy and high density region (see Chap. 1). Without including the K-mixing process, the trend of experimental data would not be reproduced. This observation means that K-mixing is essential to explain the decay hindrance of excited high-K bands.

One can then conclude that the results here discussed give evidence that discrete excited bands, in average, follow selection rules on the K-quantum number which are well reproduced by a K-mixing model. This explains the gradual weakening of the K hindrance as a consequence of the increasing in the density of states with excitation energy. This results in a lower hindrance value f_ν for higher excited states above yrast, while low-lying discrete states, before the full mixing regime sets in ($U > 1\ MeV$), are expected to show a much stronger quenching in the decay between states with different K-quantum number distributions, as also observed in our data.

Conclusion

The warm nuclear rotational motion of ^{174}W has been studied in detail in this thesis, in order to probe the validity of the selection rules on the K quantum number, as a function of temperature.
This nucleus has been populated by a fusion-evaporation reaction of ^{50}Ti (at 217 MeV) on a ^{128}Te backed target. The experiment was performed in July 2010 at Legnaro National Laboratories of INFN, using the AGATA Demonstrator, coupled to an array of 27 BaF_2 scintillators, named the HELENA array.
Different $\gamma - \gamma$ matrices, gated on specific nuclear configurations, have been built and analysed through statistical fluctuation techniques.
The analysis shows that there are $\sim$ 37 discrete bands, equally divided between low-K and high-K configurations. This result is found to be in good agreement with microscopic Cranked Shell Model calculations and simulated data, choosing as a discrimination threshold between low- and high-K states, the value $K_{thr} = 6$.
A statistical analysis based on covariance studies has confirmed that the low-K and high-K structures participate almost equally to the nuclear de-excitation of ^{174}W, in accordance to simulation calculations. In addition to this, it has been found, by analysing simulated $\gamma - \gamma$ matrices, that the covariance between low-K and high-K spectra is close to 0, confirming the robustness of the selection rules in the discrete bands region up to the region where rotational damping sets in ($U \approx 1\ MeV$).
Finally, the study on the K hindrance to the γ decay, discussed in the last Chapter, has revealed the importance of the K mixing process in explaining the decay along rotational bands. In particular, a K-mixing model is necessary to explain the gradual weakening of the K hindrance with temperature as a consequence of the increasing in the density of states with excitation energy. Our results probe the overall hindrance on K for the entire body of discrete bands, which is found to

follow the general trend observed for the discrete K-isomers E2 decay in the same mass region. This gives evidence, for the first time, that the hindrance to the γ decay between low-K and high-K structures is a general property for all discrete levels, including both rotational structures as well as K-isomeric states.
This result is relevant for a general understanding of the γ decay properties of high-K isomeric states.

Acknowledgements

Bibliography

[1] Bohr, A. & Mottelson, B. R. *"Nuclear Structure, Volume II: Nuclear Deformations"* (World Scientific, Singapore, 1998).

[2] Garrett, J. D. *et al. Phys. Lett. B* **392**, 24 (1997).

[3] Bracco, A. & Leoni, S. *Rep. Prog. Phys.* **65**, 299 (2002).

[4] Leoni, S. *et al. Phys. Rev. C* **72**, 034307 (2005).

[5] Tandel, S. K. *et al. Phys. Rev. C* **73**, 044306 (2006).

[6] Tandel, S. K. *et al. Phys. Rev. C* **77**, 024313 (2008).

[7] Akkoyun, S. *et al. Nucl. Instrum. and Meth. in Phys. Res. A* **668**, 26 (2012).

[8] Døssing, T. *et al. Physics Reports* **268**, 1 (1996).

[9] Matsuo, M. *et al. Nucl. Phys. A* **736**, 223 (2004).

[10] Walker, P. *et al. Phys. Lett. B* **408**, 42 (1997).

[11] Hodgson, P. E., Gadioli, E. & Erba, E. *"Introductory Nuclear Physics"* (Oxford University Press, 1997).

[12] Shalit, D. & Feshbach. *"Theoretical nuclear physics"*, vol. 1 (1990).

[13] Wilczynski, J. *Nucl. Phys. A* **216**, 386 (1973).

[14] Cohen, S., Plasil, F. & Swiatecki, W. J. *Annals of Physics* **82**, 557 (1974).

[15] Herskind, B. *et al.* In *Proc. Int. Conf. on Nucl. Phys.*, 117 (1983).

[16] Bosetti, P. *et al. Phys. Rev. Lett.* **76**, 1204 (1996).

[17] Krane, K. S. *"Introductory Nuclear Physics"* (John Wiley and sons, Singapore, 1988).

[18] Bohr, A. & Mottelson, B. R. *Physica Scripta* **24**, 71 (1981).

[19] Casten, R. *"Nuclear Structure from a simple perspective"* (Oxford University Press, New York, 1990).

[20] Ejiri, H. & de Voigt, M. J. A. *"γ-ray and Electron Spectroscopy in Nuclear Physics"* (Oxford University Press, New York, 1989).

[21] Lauritzen, B., Døssing, T. & Broglia, R. A. *Nucl. Phys. A* **457**, 61 (1986).

[22] Leoni, S. *et al. Phys. Rev. C* **79**, 064307 (2009).

[23] Mottelson, B. R. *Nucl. Phys. A* **557**, 717c (1993).

[24] Walker, P. & Dracoulis, G. *Nature* **399**, 35 (1999).

[25] Loebner, K. E. G. *Phys. Lett. B* **26**, 369 (1968).

[26] Benzoni, G. *et al. Phys. Lett. B* **615**, 160 (2005).

[27] Stephens, F. S. *et al. Phys. Rev. Lett.* **94**, 042501 (2005).

[28] Leoni, S. *et al. Europ. Phys. Journ. A* **4**, 229 (1999).

[29] Bracco, A. *et al. Phys. Rev. Lett.* **76**, 4484 (1996).

[30] Bengtsson, T. *et al. Phys. Rev. Lett.* **62**, 2448 (1989).

[31] Narimatsu, K. *et al. Nucl. Phys. A* **601**, 69 (1996).

[32] Matsuo, M. *et al. Nucl. Phys. A* **617**, 1 (1997).

[33] Farnea, E. *et al. Nucl. Instrum. and Meth. in Phys. Res. A* **621**, 331 (2010).

[34] Georgiev, A., Gast, W. & Lieder, R. M. In *IEEE Transactions on Nuclear Science*, vol. 41, 1116 (1994).

[35] Recchia, F. *et al. Nucl. Instrum. and Meth. in Phys. Res. A* **604**, 555 (2009).

[36] Olariu, A. *et al.* In *IEEE Transactions on Nuclear Science*, vol. 53, 1028–1031 (2006).

[37] Kröll, T. & Bazzacco, D. *Nucl. Instrum. and Meth. in Phys. Res. A* **565**, 691 (2006).

[38] Crespi, F. C. L. *et al. Nucl. Instrum. and Meth. in Phys. Res. A* **570**, 459 (2007).

[39] Boston, A. J. *et al. Nucl. Instrum. and Meth. in Phys. Res. B* **261**, 1098 (2007).

[40] Kojouharov, I. *et al.* In *IEEE Nuclear Science Symposium Conference Record*, vol. 3, 2213 (2007).

[41] Kröll, T. & Bazzacco, D. *Nucl. Instrum. and Meth. in Phys. Res. A* **463**, 227 (2001).

[42] http://mgs2005.in2p3.fr/Mgs.php. "MGS software".

[43] Crespi, F. C. L. *et al. Nucl. Instrum. and Meth. in Phys. Res. A* **620**, 299 (2011).

[44] van der Marel, J. & Cederwall, B. *Nucl. Instrum. and Meth. in Phys. Res. A* **437**, 538 (1999).

[45] Schmid, G. J. *et al. Nucl. Instrum. and Meth. in Phys. Res. A* **430**, 69 (1999).

[46] Lopez-Martens, A. *et al. Nucl. Instrum. and Meth. in Phys. Res. A* **533**, 454 (2004).

[47] Bazzacco, D. *Nucl. Phys. A* **746**, 248 (2004).

[48] Radford, D. C. *Nucl. Instrum. and Meth. in Phys. Res. A* **361**, 297 (1995).

[49] Maj, A. *et al. Nucl. Phys. A* **571**, 185 (1994).

[50] Giaz, A. *"Enhancing the capability for nuclear strucure experiments with BaF_2 detectors coupled to large arrays"*. Master's thesis, University of Milan (2008/09).

[51] Boiano, C. *et al.* In *IEEE Nuclear Science Symposium Conference Record*, 2068 (2008).

[52] Grave, X. *et al.* In *Real Time Conference, 2005. 14th IEEE-NPSS* (2005).

[53] http://www.sparrowcorp.com/products/software.
"Kmax - Advanced tools for industry, education and research".

[54] http://agata.pd.infn.it/documents/simulations/agataCode.html.
"AGATA simulation code".

[55] Tarasov, O. B. & Bazin, D. *Nucl. Instrum. and Meth. in Phys. Res. B* **204**, 174 (2003).

[56] Walker, P. M. *et al. J. Phys. G: Nucl. Phys* **4**, 1655 (1978).

[57] Wang, H. X. *et al. Phys. Rev. C* **86**, 044305 (2012).

[58] Deleplanque, M. A. *et al. Phys. Rev. Lett.* **45**, 172 (1980).

[59] Ellegaard, C. *et al. Phys. Rev. Lett.* **48**, 670 (1982).

[60] Leoni, S. *"Study of the quasi-continuum nuclear rotational motion at high angular momenta"*. Ph.D. thesis, University of Milan (1992).

[61] Leoni, S. *et al. Nucl. Phys. A* **671**, 71 (2000).

[62] Cromaz, M. *et al. Phys. Rev. C* **54**, 2055 (1996).

[63] Pühlhofer, F. *Nucl. Phys. A* **280**, 267 (1977).

[64] Winter, A. *et al. Nucl. Phys. A* **594**, 203 (1995).

[65] http://jacobi.ifj.edu.pl/∼mazurek/2/index_yrast.php.
"Lublin - Strasbourg Drop Model for rotating nuclei - yrast line".

[66] http://jacobi.ifj.edu.pl/∼mazurek/foldmul/index_fold.php.
"Multiplicity filter response function".

[67] http://www.nndc.bnl.gov/nudat2/.
"NuDat - National Nuclear Data Center".

[68] Gascon, J. *et al. Nucl. Phys. A* **472**, 558 (1987).

[69] Swan, T. P. D. *et al. Phys. Rev. C* **86**, 044307 (2012).